FACULTY OF MECHANICAL ENGINEERING

Department of Production Machines and Equipment

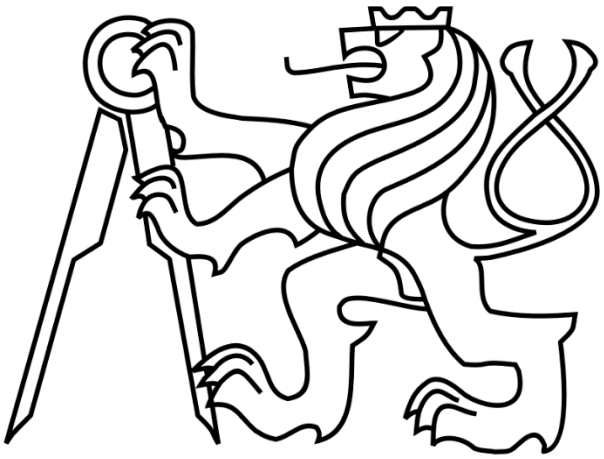

Master thesis

An Experimental Investigation of Thermal Contact Resistance between Bearing Ring and Housing in Spindle Applications

Experimentální stanovení tepelných odporů v kontaktu mezi ložiskovým kroužkem a tubusem vřetene

2016 **Bc. Martin Okénka**

Thesis assignment

DECLARATION

I declare that I have developed and written the enclosed master thesis completely by myself and have stated all information sources or means in enclose list in accordance with the Guidelines of adhering to ethical principles in the preparation of undergraduate theses, issued by the Czech Technical University in Prague on 1/7 2009.

I do not have a relevant reason against the use of this academic work in accordance with § 60 of the Act no.121 / 2000 Coll., on copyright, rights related to copyright and amending some laws (Copyright Act).

In Prague, 15/7 2016 ……..

Signature

ACKNOWLEDGEMENT

I would like to express my gratitude to the supervisor of my thesis Ing. Otakar Horejš, Ph.D., for his kind advise, guidance and comprehensive support. Many thanks also to Ing. Peter Kohút, Ph.D, for his endless help with practical issues. I am equally grateful for help and neat explanation concerning the FE modelling to Jaroslav Šindler. Thanks belong to Ing. Josef Kekula for his immediate help with measurement. For never-ending support, patience and help with graphical work on the thesis I would like to express my deepest thankfulness to Bc. Kateřina Glaserová.

Annotation

Author:	Bc. Martin Okénka
Title of master thesis:	An Experimental Investigation of Thermal Contact Resistance between Bearing Ring and Housing in Spindle Applications
Extent:	96 pages, 69 figures, 17 tables
Academic year:	2015/2016
Department:	Ú12135 – Department of Production Machines
Supervisor:	Ing. Otakar Horejš, Ph.D.
Consultant	Ing. Peter Kohút, Ph.D., Jaroslav Šindler
Submitter of the topic:	CTU – Faculty of Mechanical Engineering, Ú12135
Application:	Thermo-mechanical FE models of spindle assemblies and machine tools Arbitrary problems concerning heat flux across cylindrical interface
Key words:	Spindle bearings, heat flux, cylindrical interface, thermal contact resistance, thermal resistance, thermal contact conductance, thermal conductivity
Annotation:	The thesis investigates thermal contact resistance of a cylindrical interface between a bearing ring and its housing. A brief overview of thermal issues in machine tool design accompanied with theoretical basics of heat transfer is given in the beginning. The research of thermal contact conductance models and of their experimental applications follows. In the experimental section a simplified setup is used to determine the material properties of used steel and to estimate thermal contact resistance of planar contact. The results of steady state analysis and FE model are compared. Subsequently, using the cylindrical setup, the resistance of cylindrical interface is determined. The influence of initial clearance and power rate across the contact is investigated and the values are compared to contact conductance model. A brief insight to the influence of lubricant and of relative position of the specimens is given afterwards together with a comparison of ideal and real contact. Potential impact of gained data is evaluated eventually.

Anotace

Jméno autora:	Bc. Martin Okénka
Název DP:	Experimentální stanovení tepelných odporů v kontaktu mezi ložiskovým kroužkem a tubusem vřetene
Rozsah práce:	96 stránek, 59 obrázků, 17 tabulek
Akad. rok vyhotovení:	2015/2016
Ústav:	Ústav výrobních strojů a zařízení
Vedoucí DP:	Ing. Otakar Horejš, Ph.D.
Konzultant:	Ing. Peter Kohút, Ph.D., Jaroslav Šindler
Zadavatel tématu:	ČVUT FS, Ú12135
Využití:	Termo-mechanické MKP modely vřetenových jednotek a výrobních strojů Obecné aplikace z oblasti tepelného toku válcovým kontaktem těles
Klíčová slova:	Vřetenová ložiska, tepelný tok, válcový kontakt těles, tepelný odpor kontaktu, tepelný odpor, tepelná vodivost kontaktu, tepelná vodivost
Anotace:	Předložená práce se zabývá tepelným odporem válcového kontaktu mezi ložiskovým kroužkem a tubusem vřeteníku. Nejdříve je stručně popsána tepelná problematika v oblasti výrobních strojů společně s teoretickými základy přenosu tepla. Následuje přehled modelů tepelné vodivosti kontaktu doplněný přehledem odpovídajících experimentů. V praktické části práce je nejdříve popsán experiment ve zjednodušeném uspořádání pro stanovení materiálových vlastností použité oceli a pro odhadnutí tepelného odporu rovinného kontaktu. Výsledky z ustáleného stavu jsou porovnány s FE modelem systému. Následovně, experimentem ve válcovém uspořádání, je určen tepelný odpor válcového kontaktu. Je vyšetřen vliv počáteční vůle mezi povrchy, vliv velikosti tepelného toku přes kontakt a získané hodnoty jsou porovnány s modelem vodivosti kontaktu. Následuje stručný přehled vlivu maziva v kontaktu a vlivu vzájemného natočení členů společně s porovnáním ideálního kontaktu s reálným. Možný dopad získaných výsledků je zhodnocen nakonec.

Contents

Nomenclature

A	Cross-sectional area	$[m^2]$
b	Thickness of solid in direction of heat flux	$[m]$
c_p	Isobaric specific heat capacity	$[J/kgK]$
c_V	Isochoric specific heat capacity	$[J/kgK]$
d	Diameter	$[m]$
E	Modulus of elasticity	$[Pa]$
H	Surface microhardness	$[Pa]$
h	Thermal contact conductance	$[W/m^2K]$
h_{full}	Height of specimen	$[m]$
h_g	Gap contact conductance	$[W/m^2K]$
h_r	Radiation heat transfer coefficient	$[W/m^2K]$
h_{red}	Reduced height of specimen	$[m]$
h_s	Solid spot thermal contact conductance	$[W/m^2K]$
I	Electrical current	$[A]$
k	Thermal conductivity	$[W/mK]$
L	Length	$[m]$
p	Pressure	$[Pa]$
P	Power rate	$[W]$
$P_{p/e}$	Dimensionless pressure (plastic/elastic cond.)	$[-]$
Pr	Prandtl number	$[-]$
q	Heat flow	$[W]$
$\dot{q}$	Heat flux	$[W/m^2]$
$\dot{q}_l$	Heat flux per axial unit length	$[W/m]$
r	Radial coordinate	$[m]$
R	Avogadro constant	$[J/molK]$
Ra	Average roughness	$[um]$
Rc	Thermal contact resistance	$[Km^2/W]$
R_h	Electrical resistance of heater	$[Ohm]$
R_w	Thermal resistance of solid	$[Km^2/W]$
T	Temperature	$[°C], [K]$
t	Time	$[s]$
U	Voltage	$[V]$
V	Volume	$[m^3]$
x	Coordinate in direction of heat flux	$[m]$

α	Thermal accommodation coefficient	$[-]$
$\alpha_{ring/hous.}$	Thermal expansion linear coefficient	$[K^{-1}]$
δ	Distance of mean planes of surfaces	$[m]$
ε_{hoop}	Tangential (hoop) deformation	$[-]$
γ	Specific heat ratio	$[-]$
ν	Poisson's ration	$[-]$
σ	Root mean square average of the profile	$[\mu m]$
σ_u	Tensile strength	$[Pa]$
σ_y	Yield strength	$[Pa]$
$tan\theta$	Mean of absolute slope of a profile	$[-]$

1 Preface

The thesis investigates thermal contact resistance of cylindrical contact between a bearing ring and its housing. Specifically, the focus is on a bearing assembly of machine tool spindle group. In order to determinate the range of the thermal contact resistance, following steps are undertaken.

Review of literature is presented first, examining heat sources in machine tools and basics of heat transfer in solids and their contacts. Models of thermal contact conductance are researched and their comparison to various experimental results is presented. Experiments concerning heat transfer across typical joints in machine tool design follow. An insight into material problematics is given as well.

In experimental section, a two-stage experiment is designed. First, a simplified experiment is performed to verify design assumptions and to measure thermal conductivity of material further used for following measurement. A simple measurement is carried out to determine thermal contact resistance of planar interface under insignificant pressure. The results are compared to the models presented previously.

A main objective of the thesis, the cylindrical interface between bearing ring and housing is then investigated. A full scale experiment is conducted eventually. Values of resistance of interface between bearing housing and individual bearing rings are compared to situation with ideal contact. A thermal conductance model is compared to obtained experimental values. A contribution of other influential parameters is investigated as well.

The results of the full scale experiment are discussed and graphically presented. The study of their possible impact on thermo-mechanical modelling of spindle assemblies is carried out at last.

2 Review of literature – research of thermal contact conductance

To fully understand the problem of heat transfer from bearing rings to housings across their contact or narrow gap, related available literature is reviewed in the following chapter.

A general insight to thermal problematic in machine tool design is given at the very beginning. Sources of heat are determined and their negative effects are described. The Wide approach is then reduced to problems connected to heat transfer from bearing ring to housing.

Research concerning heat transfer, thermal conduction and conductance is provided. Problems of a composite plane wall and a composite cylindrical wall are discussed for their close relation to the bearing to housing heat transfer. The phenomena of thermal resistance and imperfect contact of materials are introduced.

Thermal contact conductance theories follow. The phenomenon is split into solid spot conductance, gap conductance and radiation. The theories are divided by their assumptions and the most influential factors for thermal contact conductance are presented.

Subsequently, experiments related to bearing to housing heat transfer are selected from a number of thermal contact conductance experiments and are discussed. Experimental results are compared to corresponding thermal contact conductance models.

At the end, experiments involving heat transfer across other parts of production machines are listed.

At the very end, a brief research of materials used in spindle application is given and range of thermal properties of individual construction components is estimated.

2.1 Disruptive thermal effects

Machine tools are exposed to a number of heat sources which affect the temperature of individual machine parts not only during machining. These sources vary with time and load and negatively influence accuracy. Caused distortion is then inversely proportional to the thermal toughness of a machine tool. The sources of heat are identified in Figure 1 by [1].

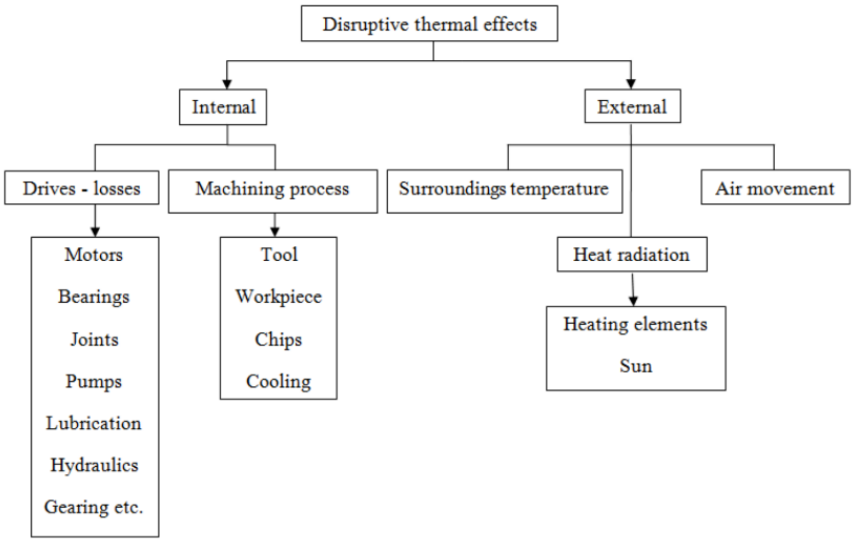

Figure 1: Classification of disruptive thermal effects influential in machine tool design, [1], processed by [20]

While external heat is transferred to the machine construction mainly by convection and radiation, internal heat transfer is carried out by conduction mainly. The heat transfer in solid material is well described and thus the focus of further investigation lays on discontinuities in machine tool design. Generally, all kinds of joints act as hardly predictable elements, for instance, welded, bolted and pressed joints between fixed parts. Joints enabling relative motion behave even more complex, for instance linear guideways, ball bearings, hydrostatic or hydrodynamic guideways, cylindrical and planar fits with clearance.

Comprehensive insight into qualities of those connections would enable more precise prediction of machine tool distortion and so its correction as well.

Thus thermal contact conductance of bearing ring and housing contact needs to be examined as one of the areas that need to be explored more thoroughly.

2.2 Point of interest

Once comprehensively described, thermal properties of contact between bearing ring and housing or spindle shaft can be used to refine thermo-mechanical models of spindles and spindle housings. To locate the exact point of interest, see Figure 2.

The schema shows a bearing and its surroundings. The main source of disruptive heat are friction forces in bearing. Generated heat is then transferred in radial direction from bearing races to housing and shaft and in axial direction to spacers. The ratio of thermal resistances in individual directions determines the most heated neighbouring parts.

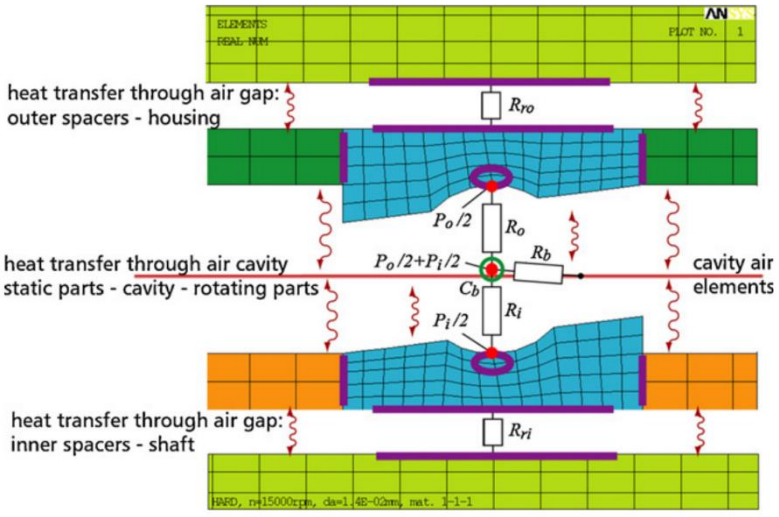

Figure 2: Thermo-mechanical model of spindle bearing, spindle shaft and housing, note R_{ro} marking exact point of interest of the thesis, [24]

Therefore, if heat is directed unevenly, surrounding parts are heated unequally and thus thermally caused distortion is bigger than necessary. By investigation of thermal contact conductance phenomenon in spindle applications, obtained accuracy of machining can be improved.

2.3 Thermal contact conductance introduction, basic relations

For a better orientation in the area of heat transfer, the problem of heat flow through plane wall is described, followed by an analysis of composite plane wall, tube and composite tube. Both [2] and [3] give a basic overview, while [4] gives more complex insight.

2.3.1 Heat transfer through simple plane wall

As purely conductive heat transfer, heat flux $\dot{\boldsymbol{q}}$ $[W/m^2]$ through solids is given by Fourier's law that states

$$\dot{\boldsymbol{q}} = -k\boldsymbol{grad}T \qquad (2\text{-}1)$$

saying that the heat flux goes in the direction of descending temperature and is proportional to temperature gradient and to k $[W/mK]$, thermal conductivity of material.

Applied on boundless plane wall oriented perpendicularly to x axis, the relation is reduced to

$$\dot{q} = -k\frac{dT}{dx} \qquad (2\text{-}2)$$

applying boundary conditions of constant temperatures on surfaces of the wall (see Figure 3), temperature distribution along thickness of wall is given as

$$T(x) = T_{w1} - \frac{\dot{q}}{k}x \qquad (2\text{-}3)$$

which is an usable relation for thermal contact conductance investigation giving the possibility of measuring heat flux by two thermometers placed in a compact material at known distance.

By investigating heat flux through full thickness b of the wall, thermal resistance concept can be introduced using thermal resistance of the wall R_W $[K.m^2/W]$

$$\dot{q} = \frac{k}{b}(T_{w1} - T_{w2}) = \frac{(T_{w1} - T_{w2})}{\frac{b}{k}} = \frac{(T_{w1} - T_{w2})}{R_W} \qquad (2\text{-}4)$$

Giving an analogy to the Ohm's law $I = U/R$, where $(T_{w1} - T_{w2})$ corresponds to voltage U, $\dot{q}$ to current I and R_W to electric resistance R.

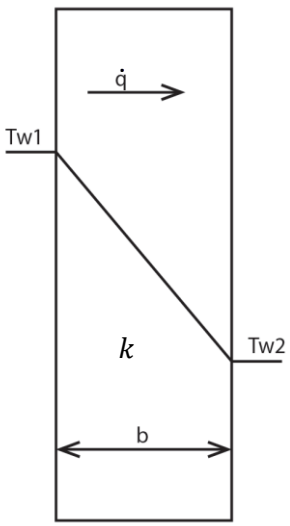

Figure 3: Simple plane wall temperature distribution

2.3.2 Heat transfer through composite plane wall

Presented relations can be easily modified for composite plane wall assuming perfect contact between layers. More detailed derivation is given in [2] or [3] as well as [4].

Let's denote parameters of individual layers as k_i, b_i, $R_{w\,i}$. Heat fluxes through each layer $\dot{q}_i = \dot{q}$ are the same and constant because of energy conservation principle. The assumption of perfect contact leads to identical temperatures of adjoining surfaces. Thus temperature T_i is to be understood as the temperature at the beginning of the i^{th} layer in the direction of heat flux. See Figure 4 showing denotation and temperature distribution in composite wall. Chaining equations of heat flux for each of n layers gives relation of heat flux through composite wall

$$\dot{q} = \frac{(T_{w\,1} - T_{w\,n+1})}{\sum_{i=1}^{n} \frac{b_i}{k_i}} = \frac{(T_{w\,1} - T_{w\,n+1})}{\sum_{i=1}^{n} R_{w\,i}} = \frac{(T_{w\,1} - T_{w\,n+1})}{R_w} \qquad (2\text{-}5)$$

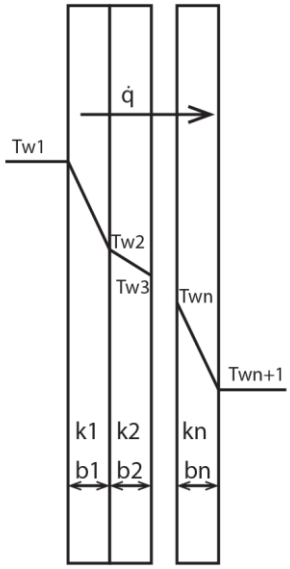

Figure 4: Temperature distribution in plane composite wall

Now the imperfect contact of rough surfaces can be introduced. Basics are given in [3] and [4].

Technical usage of hard materials with rough surface forces us to leave the assumption of perfect contact between layers and so different temperatures of neighbouring surfaces need to be expected (as shows Figure 5). The phenomenon of imperfect contact known as thermal contact resistance is a more complex problem and the theories dealing with it are described in the following chapters.

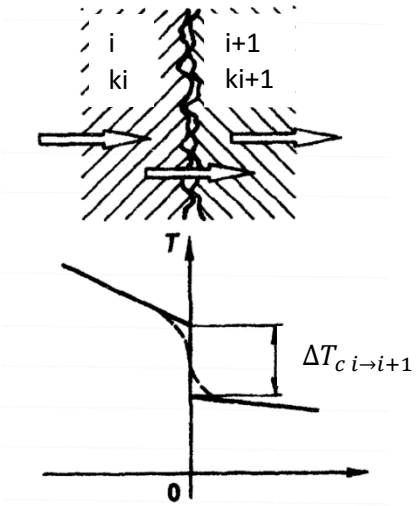

Figure 5: Temperature discontinuity on rough surfaces, [3]

Simplified approach assumes contact temperature drop depending on many parameters. Heat flux $\dot{q}$, pressure P, roughness and thermal properties of the materials and interstitial fluid are the main of them. This temperature discontinuity between i^{th} and $(i+1)^{th}$ layer can be expressed by thermal contact resistance $R_{c\,i\to i+1}$ $[m^2K/W]$ as follows

$$R_{c\,i\to i+1} = \frac{T_i - T_{i+1}}{\dot{q}} \qquad (2\text{-}6)$$

Knowing thermal resistance of individual layers and thermal contact resistance between each two of them, heat flux relation for composite plane wall with imperfect contacts can be derived.

$$\dot{q} = \frac{(T_{w\,1} - T_{w\,n+1})}{\sum_{i=1}^{n} R_{w\,i} + \sum_{i=1}^{n-1} R_{c\,i\to i+1}} \qquad (2\text{-}7)$$

2.3.3 Heat transfer through a simple cylindrical wall

Let us consider boundless cylindrical wall with constant surface temperatures $T_{w1} > T_{w2}$. Due to axial symmetricity of geometry and boundary conditions, the heat flux can be investigated as one dimensional along radial axis r.

Using Fourier's law (eq. (2-1)) and cylindrical coordinates and boundary conditions of constant temperatures on the surfaces, one can obtain the formula for the temperature distribution. See Figure 6 illustrating logarithmic temperature distribution and the boundary conditions. Full derivation is given by [4].

$$T = T_{w1} - \frac{\dot{q}_l}{2\pi k} ln \frac{r}{r_1} \qquad (2\text{-}8)$$

where $\dot{q}_l$ (W/m) stands for heat flux per axial unit length.

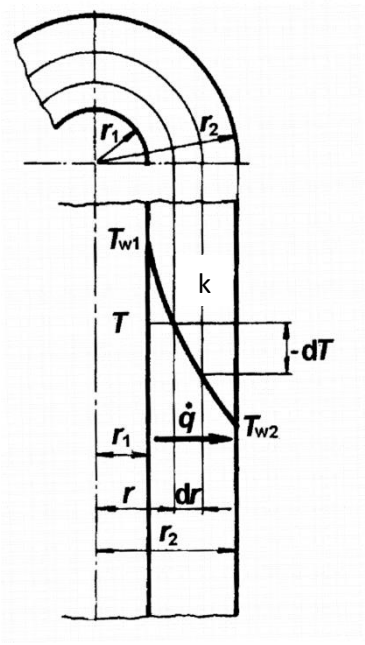

Figure 6: Temperature distribution along radial coordinate in boundless cylindrical wall, [2]

Thermal resistance concept can be introduced in the same manner for the plane wall by expressing heat flux through the full thickness of the cylindrical wall.

$$\dot{q}_l = \frac{T_{w1} - T_{w2}}{\frac{1}{2\pi k} ln\frac{r_2}{r_1}} = \frac{T_{w1} - T_{w2}}{R_w} \qquad (2\text{-}9)$$

2.3.4 Heat transfer through composite cylindrical wall

Let's assume boundless cylindrical composite wall with perfectly contacting layers. Each of them with known parameters k_i, r_i, r_{i+1}, $R_{w\,i}$, where r_i, r_{i+1} are the inner and outer radius of i^{th} layer respectively. And heat flux per axial unit length $q_{l\,i}^{\cdot} = \dot{q}_l$ is constant.

Chaining equations across all n layers yields the expression of heat flux through composite wall as follows. See [4] for a more thorough derivation and Figure 7 depicting logarithmic temperature distribution.

$$\dot{q}_l = \frac{T_{w1} - T_{w2}}{\frac{1}{2\pi}\sum_{i=1}^{n}\frac{1}{k_i} ln\frac{r_{i+1}}{r_i}} = \frac{T_{w1} - T_{w2}}{\sum_{i=1}^{n} R_{w\,i}} = \frac{T_{w1} - T_{w2}}{R_w} \qquad (2\text{-}10)$$

Now thermal contact resistance needs to be implemented in the same manner as for the composite plane wall

$$\dot{q}_l = \frac{T_{w1} - T_{w2}}{\sum_{i=1}^{n} R_{w\,i} + \sum_{i=1}^{n-1} R_{c\,i\to i+1}} \qquad (2\text{-}11)$$

which, assuming other parameters as known, easily yields the expression for thermal contact conductance in cylindrical composite wall.

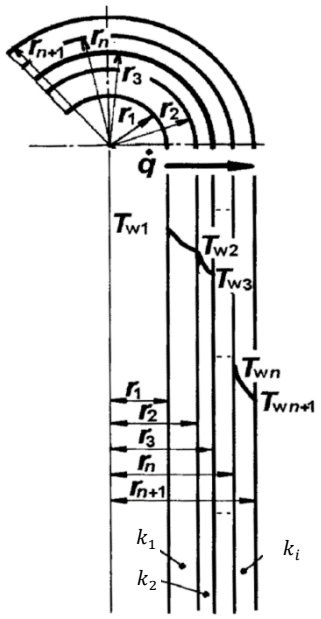

Figure 7: Temperature distribution along radial coordinate in boundless cylindrical composite wall, [2]

2.4 Thermal contact conductance prediction theories

The overlook of theoretical prediction of contact thermal conductance of nominally flat surfaces is given in the following chapter.

2.4.1 Factors influencing thermal contact conductance

Out of many factors involving thermal and mechanical properties of joint materials as well as external conditions, the most influential parameters to thermal joint conductance are named below, [5].

Pressure (p)

Generally, one of the most influential factor. With higher pressure comes higher deformation of asperities and actual contact area increases resulting in conductance growth.

Surface geometrical properties

Parameters as mean of absolute slope of a profile ($tan\theta$), roughness (Ra, σ) and flatness deviation determine the actual contact area and thus thermal conductance.

Gap thickness (δ)

Distance of mean planes of rough surfaces in contact. The parameter dominantly influences gap contact conductance and is determined by surface geometrical properties and applied pressure and by actual measurable gap.

Thermal properties of solids

The conductivity of all involved materials (k) of solids in contact. And linear expansion coefficient of contacting solids (α).

Mechanical properties of solids

Surface microhardness (H) and yield strength (σ_y) of mating materials determine plastic deformation of asperities. While modulus of elasticity of solids (E) influence elastic deformation of asperities.

Average temperature of contact

The interface temperature influences most of the other parameters as they are usually not constant with temperature.

Interface material

The presence of interstitial fluid, coating, foil or intermediate plates and their thermomechanical properties or vacuum condition largely determines thermal joint properties.

2.4.2 Basic relations

Here the fundamental parameters and relations are stated. So far no interstitial fluid is taken in consideration, vacuum is expected instead. Neat explanation is given by [6], [7] provides even more detailed insight.

Unlike in previous chapters, thermal contact conductance $h\ [W/m^2K]$ is used. Nevertheless h equals to the inverse of thermal contact resistance

$$R_c[m^2K/W] = \frac{1}{h} \qquad (2\text{-}12)$$

Thermal contact conductance consists of contributions of solid spot conductance h_s and radiation heat transfer coefficient h_r. In case of present interstitial fluid, its contribution would occur as h_g, gap conductance. So one can write

$$h = h_s + h_r\ (+h_g) \qquad (2\text{-}13)$$

In [6] the thermal contact conductance is reasonably used in dimensionless form as

$$\bar{h} = \frac{h\,\sigma}{k\ tan\theta} \qquad (2\text{-}14)$$

where σ stands for standard deviation of profile height $RMS\ [m]$, $k\ [W/mK]$ for thermal conductivity of solids in contact and $tan\theta$ stands for the mean of absolute slope of a profile.

Once dimensionless $\bar{h}$ is introduced, it is convenient to use dimensionless pressure for plastic deformation P_p as well. By [7] it is introduced as ratio of applied pressure $P[Pa]$ on contact and microhardness $H\ [Pa]$

$$P_p = \frac{p}{H} \qquad (2\text{-}15)$$

or dimensionless pressure for elastic deformation mode of asperities in terms of the mean of absolute slope of a profile $tan\theta$ and combined modulus of elasticity E' (see eq. (2-25) for E' relation)

$$P_e = \frac{p\sqrt{2}}{E'tan\theta} \qquad (2\text{-}16)$$

In case of different materials in contact, their effective thermal conductivity k is calculated to be used in place of normal conductivity, [8]

$$k = \frac{2k_1k_2}{k_1+k_2} \quad (2\text{-}17)$$

Where $k_{1,2}$ $[\mathrm{W/mK}]$ are conductivities of individual solids.

Surface roughness parameters are usually described by the arithmetic average of absolute values of surface roughness R_a $[m]$ or RMS – root mean square roughness σ $[m]$. Defined as, [9]

$$R_a = \frac{1}{L}\int_0^L |y(x)|dx \qquad \sigma = \sqrt{\frac{1}{L}\int_0^L y^2(x)dx} \quad (2\text{-}18)$$

and assuming Gaussian distribution of asperities, roughnesses are related as stated below. This relation was found as adequately accurate by [5].

$$\sigma = \sqrt{\frac{\pi}{2}}\, R_a \quad (2\text{-}19)$$

For differently finished materials, effective RMS roughness is used, [8]

$$\sigma = \sqrt{\sigma_1^2 + \sigma_2^2} \quad (2\text{-}20)$$

Most of the models are in different ways very weak functions of the mean of absolute slope of a profile $tan\theta$. Defined as follows, [9]

$$tan\theta = \frac{1}{L}\int_0^L \left|\frac{dz(x)}{dx}\right| dx$$

and which can be determined from RMS (σ) by relations submitted by [10]. Although the relation was commented as having high uncertainties by [9], no better correlation was found. For RMS roughness $\sigma \leq 2\ \mu m$ it stands

$$tan\theta = 0.124\sigma^{0.743} \quad (2\text{-}21)$$

For plastic models is major parameter microhardness H. The thesis [5] compiles three relation of estimating the microhardness. Relation by Lambert and Fletcher based on tensile strength σ_u, relation by Tien based on yield strength σ_y and relation based on progressive measurement of Vickers' hardness submitted by Song and Yovanovich.

$$H = 3\,.\,\sigma_u$$
$$H = 3\,.\,\sigma_y \quad (2\text{-}22)$$

$$\frac{P}{H} = \left[\frac{P}{1.62c_1\left(\frac{\sigma_s}{\sigma_0}tg\theta\right)^{c2}}\right]^{1/(1+0.71c_2)} \quad (2\text{-}23)$$

Especially for gap conductance, mean surface plane separation $\delta\ [m]$ is influential. As the surfaces are mostly in physical contact, it has to be determined from surface parameters. In case of actual measurable gap, mean surface plane separation δ would be added to its value.

$$\delta = \sqrt{2}\sigma\ erfc^{-1}\left(\frac{2p}{H}\right) \quad (2\text{-}24)$$

2.4.3 Mode of deformation

Thermal contact conductance varies with the mode of deformation of asperities on contact surfaces. Deformation mode depends on material microhardness H, shape of asperities $tan\theta$ and combined modulus of elasticity E':

$$E' = \frac{E_1 E_2}{E_1(1-\nu_2^2) + E_2(1-\nu_1^2)} \quad (2\text{-}25)$$

where $E_{1,2}$ are modules of elasticity of individual materials and $\nu_{1,2}$ are corresponding Poisson's ratios.

Note that deformation mode is not function of pressure level.

According to [6] one can expect predominant elastic deformation for following contact parameter

$$\frac{H}{E'tan\theta} \gg 3 \quad (2\text{-}26)$$

And predominant plastic deformation conversely

$$\frac{H}{E'tan\theta} \ll 3 \quad (2\text{-}27)$$

2.4.4 Plastic deformation of surface asperities

Models matching conditions of predominant plastic deformation mode are overviewed in subsequent lines. As most of construction materials are inclinable to plastic deformation of asperities in contact, plastic deformation assumption is prevailing.

Cooper, Mikic, Yovanovich, 1968, [7]

Taken chronologically, a relation for $\bar{h}$ was presented in [7] with assumption of plastic deformation of surface asperities. This is based on an estimation that less than 1 % of the area in actual contact is in elastic state. Let's denote thermal contact conductance and its dimensionless form under assumption of purely plastic deformation h_p, $\overline{h_p}$ respectively. Approximated relation states

$$\frac{h_p\ \sigma}{k\ tan\theta} = 1.45\left(\frac{p}{H}\right)^{0.985} \quad (2\text{-}28)$$

Or in dimensionless form

$$\overline{h_p} = 1.45\left(P_p\right)^{0.985} \quad (2\text{-}29)$$

The publication [7] supports this equation by comparison with experimental data shown in Figure 8. Observe the drop of experimental data against approximated line. Authors note that as long as no further information is available, one can expect real conductance to lie in area between depicted line and line lower by factor of 2.

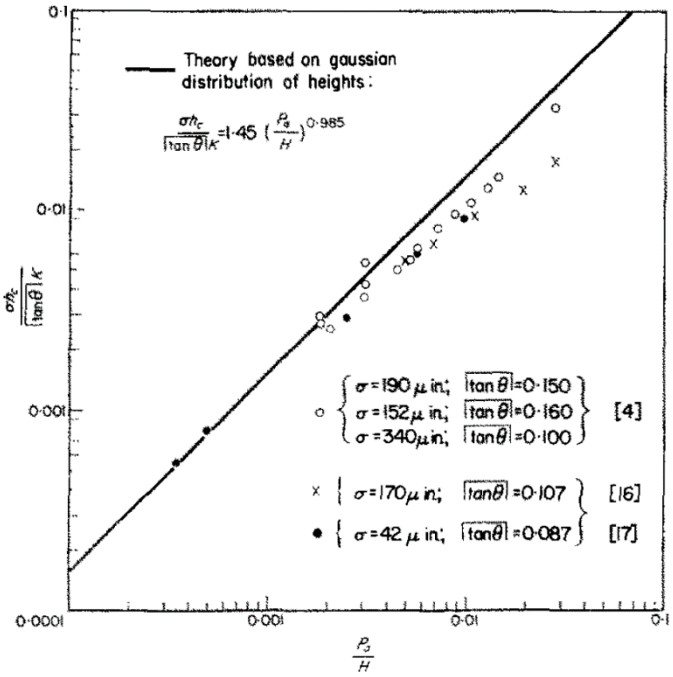

Figure 8: Dimensionless contact conductance vs. dimensionless pressure for nominally flat surface in vacuum, plotted line based on estimation of purely plastic deformation, [7], experimental data parameters: σ – surface roughness RMS, $|tan\theta|$ – the mean of absolute slope of a profile

Mikic, 1973, [6]

Later publication [6] reflects lower dispersion of experimental data and states equation for thermal contact conductance of rough nominally flat surfaces in vacuum under conditions of negligible radiation as follows. Note slightly lower coefficients.

$$\frac{h_p\,\sigma}{k\,tan\theta} = 1.13\left(\frac{p}{H}\right)^{0.94} \quad \text{or} \quad \overline{h_p} = 1.13\left(P_p\right)^{0.94} \qquad (2\text{-}30)$$

Yovanovich, 1981, [11]

The author of an even later paper and complex summary of thermal contact and gap conductance Yovanovich, [11], finds balance and states intermediate coefficients. The equation is followed by note that for each set of parameters coefficients should be investigated by experiment rather than claiming wide validity of specific values. As guideline following is submitted

$$\frac{h_p\,\sigma}{k\,tan\theta} = 1.25\left(\frac{p}{H}\right)^{0.95} \quad \text{or} \quad \overline{h_p} = 1.25\left(P_p\right)^{0.95} \qquad (2\text{-}31)$$

Cooper, Mikic, Yovanovich, 1969, [7]

And relation for dimensionless thermal contact conductance expressed in terms of the *relative mean plane separation* δ_r

$$\overline{h_p} = \frac{h_p\,\sigma}{k\,tan\theta} = \frac{1}{2\sqrt{2\pi}} \frac{\exp\left(-\frac{\delta_r^2}{2}\right)}{\left[1-\sqrt{\frac{1}{2}erfc\left(\frac{\delta_r}{\sqrt{2}}\right)}\right]^{1.5}} \qquad (2\text{-}32)$$

where δ_r stands for ratio of mean surface plane separation and roughness $\delta_r = \delta/\sigma$.

2.4.5 Elastic deformation of surface asperities

In case the contact parameters indicate significant influence or dominance of elastic deformation mode, above stated equations need to be modified.

Mikic, 1973, [6]

As is derived by [6], thermal contact conductance under elastic deformation h_e comes with a slightly higher coefficient and does not depend on microhardness H and nearly not on shape of asperities $tan\theta$.

$$\frac{h_e\,\sigma}{k\,tan\theta} = 1.55\left(\frac{p\sqrt{2}}{E'tan\theta}\right)^{0.94} \quad \text{or} \quad \overline{h_e} = 1.55(P_e)^{0.94} \qquad (2\text{-}33)$$

2.4.6 Gap conductance

So far purely conduction through solids in vacuum and under negligible radiation conditions was considered. But such can be hardly expected in industrial use. While keeping the condition of negligible radiation, let us now include the contribution of thermal conduction through interstitial fluid. As gap thickness would vary at order of thousandths or hundredths of mm, pure conduction would occur. The gap conductance is strongly prevailing for lower pressures and so its' precise evaluation is critical for estimation of the combined contact conductance. See comparison in the Figure 18.

Gap conductance by Yuncü, 2006, [12]

May thermal gap conductance be denoted as h_g. It can be determined as stated, [12]

$$h_g = \frac{k_g}{\delta + M} \qquad (2\text{-}34)$$

where k_g $(\mathrm{W/(m \cdot K)})$ stands for interstitial fluid thermal conductivity, δ (m) for distance of mean planes of mating surfaces and M for fluid parameter

$$M = \alpha\beta\Lambda \qquad (2\text{-}35)$$

$$\alpha = \frac{2-\alpha_1}{\alpha_1} + \frac{2-\alpha_2}{\alpha_2} \qquad \beta = \frac{2\gamma}{(1+\gamma)\mathrm{Pr}} \qquad \Lambda = \Lambda_0 \frac{TP_0}{T_0 P}$$

where $\alpha_{1,2}$ are the accommodation coefficients at solid-fluid interface. Their values for steel-air combination can be found for instance in [13]. Typically, it varies around $\alpha \cong 0.9$.

Fluid parameter β is determined as a fraction of *specific heat ratio* $\gamma = c_p/c_v$ and Prandtl number.

And Λ, molecular mean free path, refers to itself under changed conditions from T_0, P_0 to actual T, P.

Gap conductance by Yovanovich, 2005, [8]

Another more complex formula with maximum error of 2 % at borders of its interval of validity gives Yovanovich in [8]. Using similar notation to Yuncü, it stands

$$\overline{h_g} = \frac{h_g\,\sigma}{k\,tan\theta} = \frac{\kappa}{tan\theta}\frac{f_g}{\left(\frac{M}{\sigma}+\frac{\delta}{\sigma}\right)} \qquad (2\text{-}36)$$

where κ stands for ratio k_{gas}/k_{solid} and in range $2 \le \delta/\sigma \le 4$ the f_g stands

$$f_g = 1.063 + 0.0471\left(4-\frac{\delta}{\sigma}\right)^{1.68}\left(\ln\left(\frac{\sigma}{M}\right)\right)^{0.84} \qquad for \quad 0.01 \le \frac{M}{\sigma} \le 1$$

$$f_g = 1 + 0.06\left(\frac{\sigma}{M}\right)^{0.8} \qquad for \quad 1 \le \frac{M}{\sigma} < \infty$$

Yovanovich support his formula with experimental data shown in Figure 9. Note the good agreement of the experimental data and theoretical estimation for both situations – with and without contribution of gap conductance.

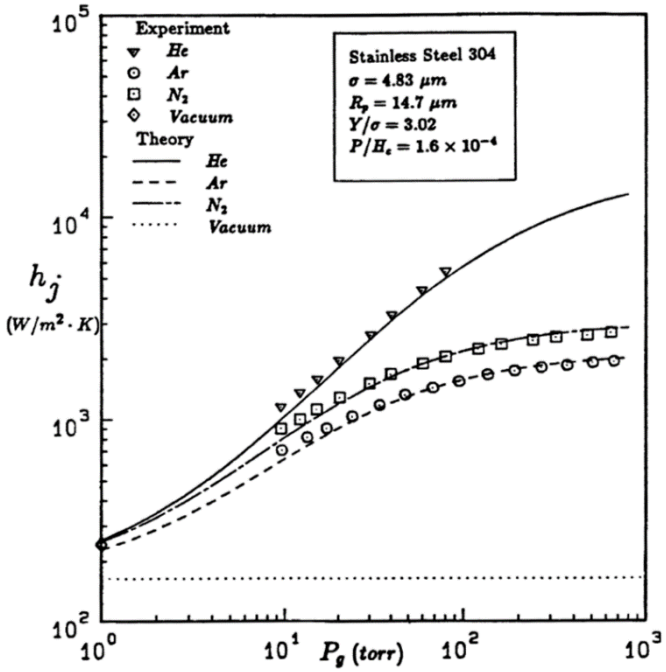

Figure 9: Joint conductance as function of atmospheric pressure and interstitial gas, [8]

Gap conductance by Wahid, Madhusudana, 2000, [14]

For predominant gap conductance Wahid and Madhusudana, [14] use formula based on modified – effective mean plane separation distance δ_{eff}

$$h_g = \frac{k_g}{\delta_{eff}} \qquad (2\text{-}37)$$

where k_g stands for thermal conductivity of gas and δ_{eff} is mean plane separation distance extended by temperature jump distance $g_{1,2}$ between individual solids and interstitial gas.

$$g_i = \frac{k_g}{P_{atm}} \frac{2-\alpha_i}{\alpha_i} \left(\frac{2\pi T_{int}}{R}\right)^{\frac{1}{2}} \frac{\gamma-1}{\gamma+1}$$

where P_{atm} is atmospheric pressure, α_i stands for accommodation coefficient, T_{int} for contact temperature, γ for specific heat ratio (defined earlier in this chapter) and R is universal gas constant.

Then δ_{eff} is defined as follows

$$\delta_{eff} = \delta + g_1 + g_2$$

2.4.7 Radiation across the interface

In conditions of significant radiation across the contact it is necessary to calculate the radiation heat transfer coefficient h_j. The radiation heat transfer is mostly by orders smaller than solid spot conductance or gap conductance, but gains on volume with increasing temperature of the interface or in situations of low contact pressure. In situation of actual gap in vacuum, it is the only possible heat transfer. In atmospheric conditions, the gap conductance is the prevailing heat transfer contributor.

Radiation heat transfer coefficient, Madhusudana, 2000, [15]

By [15], the radiation heat transfer coefficient across the joint is defined as

$$h_r = \sigma_{SB} \frac{\varepsilon_1 \varepsilon_1 (T_1^4 - T_2^4)}{(\varepsilon_1 + \varepsilon_1 - \varepsilon_1 \varepsilon_1)(T_1 - T_2)} \qquad (2\text{-}38)$$

where σ_{SB} stands for Stefan – Boltzmann constant and $\varepsilon_{1,2}$ stand for emissivity of individual materials in contact. And $T_{1,2}$ are the surface temperatures of the solids.

2.4.8 Combined thermal contact and gap conductance

Combined joint thermal conductance h_j can be estimated as a sum of contact conductance h_c and gap conductance h_g as follows, [11]

$$h_j = h_s + h_g \ (+h_r) \qquad (2\text{-}39)$$

where for spot contact conductance h_s stands h_p or h_e depending on prevailing mode of asperity deformation.

In case of high contact temperatures, the radiation heat transfer coefficient h_r would be added to the formula for h_j. Nevertheless, the radiative contribution is negligible in most of the situation with contact temperature under 450 K, [15].

2.5 Thermal contact conductance experiments

A number of experiments were performed and compared to the named models. The methodology is similar across most of them. Nevertheless, some experiments outstand by setup or explore usability of the models under specific conditions. The experiments selected and described lately are related to area of thermal properties of bearing ring and housing contact. The comparison with outlined theories is provided.

2.5.1 Experimental investigation of thermal contact conductance for nominally flat metallic contact (Tariq, Asif)

The investigation of contact conductance of brass, copper and steel is performed in vacuum chamber in [16]. Contact conductance as function of pressure and roughness is plotted and compared to both elastic and plastic theories.

The test chamber was constructed as shown in Figure 10. Tested specimens are pressed together and insulated from outer influences. Thermal load is created by a heater on the top of one specimen and a cooling block underneath the second one. A thermocouples are located on the surface of tested solids.

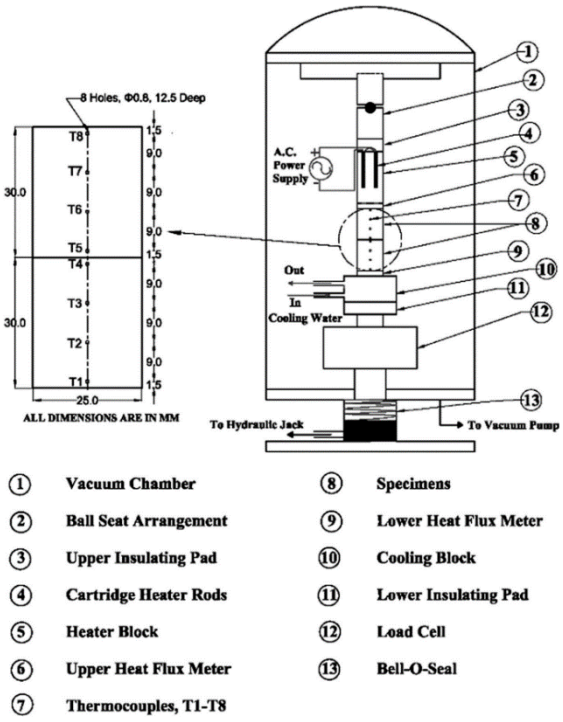

Figure 10: Experimental setup in vacuum chamber, [16]

The influence of surface roughness, pressure and material of tested couples was examined. Among other results, the most fitting model for stainless steel was identified. See Figure 11 and Figure 12 for the comparison of thermal contact conductance of stainless steel couple with both plastic and elastic theories.

Note the significant drop of experimental results against more less identical lines of individual plastic theories.

On the other hand, Mikic's elastic theory fits precisely. But more investigation is necessary to say how far this could be generalized among stainless steels. Also note that roughness turned to be almost insignificant, at least within used spectrum of values.

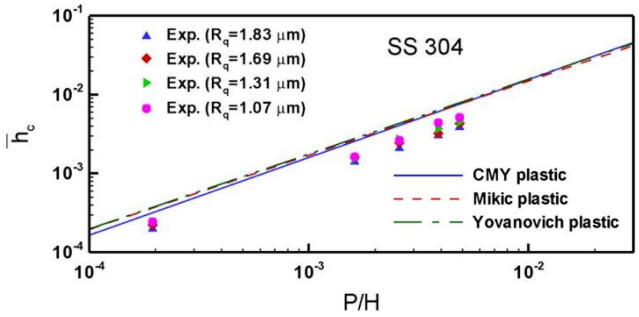

Figure 11: Dimensionless thermal contact conductance vs. dimensionless pressure. Comparison of stainless steel and plastic theories, [16]

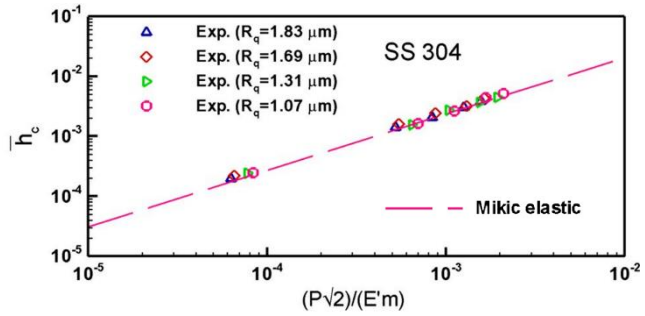

Figure 12: Dimensionless thermal contact conductance vs. dimensionless pressure. Comparison of stainless steel and Mikis's plastic theory, [16]

2.5.2 Thermal contact conductance of nominally flat surfaces (Yüncü)

A number of materials with various roughness and applied pressure were tested by Yüncü in [12]. In Figure 13 comparison of test couples to the Yovanovich plastic theory, [11], is plotted. Measured thermal joint conductance as function of applied pressure lies within an over-all error of less than 35% from theoretical curve.

Experimental setup worked under atmospheric conditions and was insulated from surrounding by mineral wool and asbestos. The data seem to have big over-all error, but their general trend is in good agreement with Yovanovich theory.

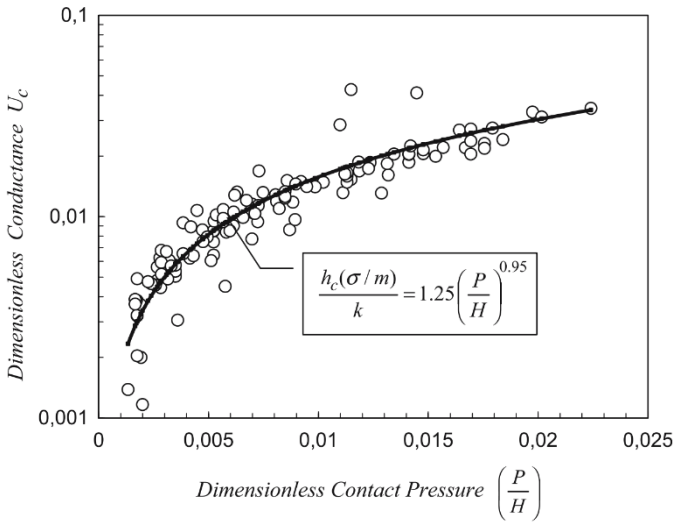

Figure 13: Yüncü's comparison of various experimental specimen, [12] to Yovanovich's plastic theory, [11]

2.5.3 Heat transfer trough contact of hastelloy and silicone steel with narrow air gap (Zhu, Zhang, Gu)

The experiment investigating heat transfer between hastelloy and silicone steel was described by [17]. This experiment outstands by providing insight to pure gap conductance.

In atmospheric conditions a transient heat transfer was tested in order to examine inadequately explored area of contact conductance with prevailing gap contribution.

See Figure 14 with shown diagram of experimental device. The two bars wrapped in insulation are heated to required temperature. Once the temperature distribution reaches a steady state, the heater and thermal insulation are removed from the right specimen. The left specimen is quickly moved towards the right one to achieve the required air gap. In the same moment, data recording starts.

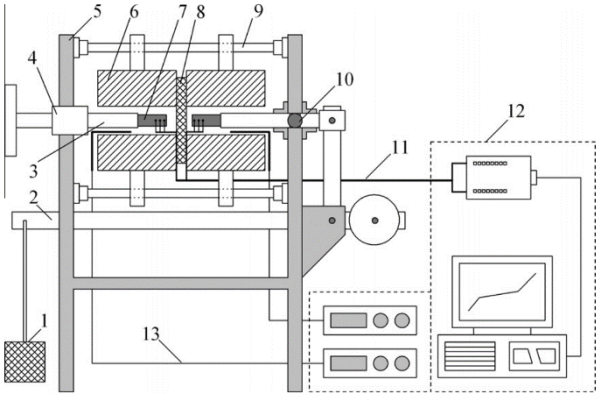

Figure 14: Experimental device for narrow gap conductance investigation, [17]: 1 weight, 2 articulated arm, 3 metal bar, 4 transmission, 5 support, 6 resistance heater, 7 tested specimen, 8 thermal insulation, 9 slide rail, 10 bearing, 11 thermocouple measuring, 12 data recording, 13 control thermocouple

The experiment shows rapid decrease of contact conductance with increasing air gap between surfaces. Unfortunately, the experimental device was unable to perform tests of gaps smaller

than 0.2 mm, so the data from the most rapidly changing part of the curve are missing. See Figure 15 plotting thermal contact conductance against gap dimension. Even though experimental data in the most interesting part of the curve are not present, it is obvious that the thermal contact conductance with only gap (and radiation) contribution is heavily dependent on gap thickness – especially for very narrow gaps.

Authors suggest the following formula to approximate the results.

$$h_g = A \exp\left(-\frac{\delta}{B}\right) + C \qquad (2\text{-}40)$$

where δ is air gap thickness and A, B, C are material and temperature related constants. The constants need to be obtained experimentally for each pair of specimens. Suggested values are valid only for Hastelloy and silicon steel pair of bars and are based on very limited number of experiments with uneven spacing.

Presented data are not compared to any theoretically estimated value of gap conductance.

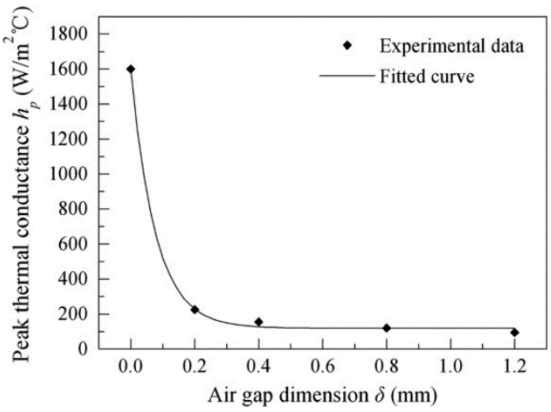

Figure 15: Effect of air gap thickness to thermal contact conductance. Data obtained by transient experiment with starting temperature of 100°C, [17]

2.5.4 Accuracy in thermal contact conductance experiments (Madhusudana)

As the majority of types of experimental attitudes were described above, it is interesting to explore the most challenging problems that similar experiments face. In publication [15] author claims that the errors associated with temperature measurement are likely to be in the order of 10 % and may be the predominant source of uncertainties.

The conclusions of author's study stand (only relevant conclusions noted):

- The heat loss to the surroundings represents the major source of uncertainty, especially in cases of:
  - Low contact pressure
  - Testing of poor conductors
  - High flatness deviations of contact surfaces
- At temperatures above 450 K radiation becomes significant heat loss
- Most of the heat loss can be significantly reduced by radiation shield

2.5.5 A new method of measuring thermal contact conductance (Rosochowska, Chodnikiewicz, Balendra)

In this study [18], authors research experiments performed in the area of thermal contact conductance and propose a new method of measurement under atmospheric conditions. This method deals with some of the uncertainty conclusions of Madhusudana presented above.

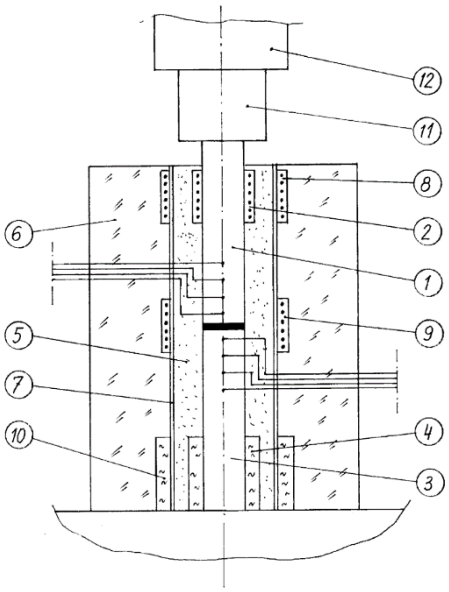

Figure 16: Proposed experimental device, [18]: 1 upper tool, 2 heater, 3 lower tool, 4 heat sink, 5 ceramic insulation, 6 wool insulation, 7 sleeve, 8 -9 compensating heaters, 10 compensating heat sink, 11 insulating element, 12 load-cell

Authors state that transient measurements require more responsive and precision equipment and suggest steady state experiment instead. To ensure one dimensional heat flow with minimal losses to the surroundings, the device is equipped with sufficient insulation and secondary heaters and heat sinks minimizing temperature gradient across the insulation. See Figure 16 depicting schema of proposed experimental device.

Note that no thermometers are placed directly in measured specimen between upper and lower tool. This precaution minimises distortion of data by interrupting heat flow by holes drilled for thermometers close to contact. Also note that the actual contact conductance is measured on two contacts at once, leading to natural averaging.

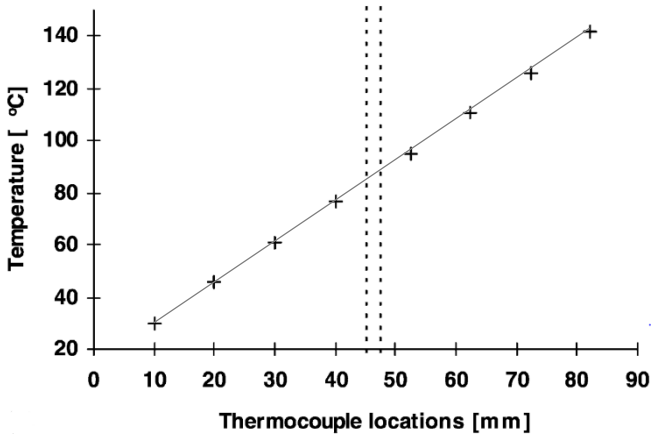

Figure 17: Temperature distribution across contact of grounded surfaces under pressure of 10 MPa, [18]

An interesting fact for the application on bearings ring shows Figure 17. Plotted measurement was carried under high contact pressure of 10 MPa with tools made of N1019 chrome steel and interstitial specimen of C8C (Ma8) steel with grounded contact surfaces (Ra 0,3 µm). Note the almost insignificant drop of temperature distribution across two contacts.

2.5.6 Thermal gap conductance at low contact pressures (Prashant Misra, J. Nagaraju)

The experiments [19] proves validity of Yovanovich's model of gap conductance for low pressures. Data are presented from $200\ kPa$ up to $1000\ kPa$ and fit well with the estimations. See Figure 18 for comparison of gap conductance estimation with measured data.

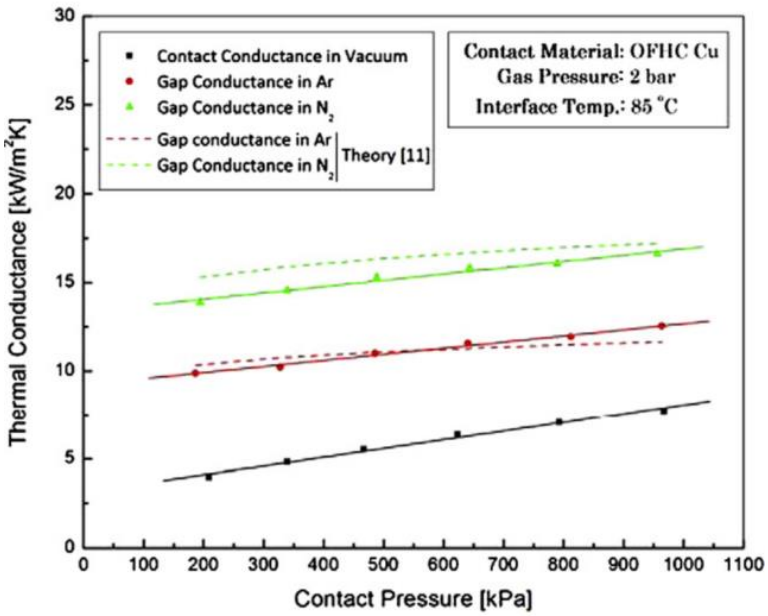

Figure 18: Pure gap conductance at low contact pressures compared to spot conductance in vacuum, [19]

Such low pressures are closer to the application in the simplified experiment presented in the chapter 3.3 . Nevertheless, the data are for copper surfaces with very smooth finishing ($\sigma = 0.55\ \mu m$) and are not presented for an air environment, thus the plot is tentative only. The data matches the models with maximum error of 7 %.

2.6 Thermal conductance across important components in machine tool design

The research of thermal conductance across other design units follows in this chapter. An experiment of thermal conductance in bolted joints and across linear guideways is presented.

2.6.1 Thermal contact conductance in bolted joints (Hasselström, Nilsson)

In the thesis [5], authors give basic overview of thermal contact conductance and follow with an experiment of bolted joint thermal conductance. This problem is more complex due to non-uniform contact pressure, conduction trough bolt bodies and three dimensional heat flow. Therefore, no presented basic theory of contact conductance can be used to be compared with experimental data. For this purpose, authors executed another experiment with pure contact of faces of cylindrical bodies, however, such measurement is very similar to the ones already presented.

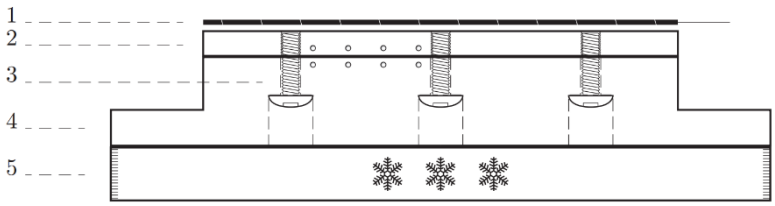

Figure 19: Experimental setup for bolted joint experiment, [5]: 1 heater, 2 top plate, 3 M3 bolts, 4 bottom plate, 5 cooled base

The experimental setup consists of two plates bolted together. Combination of various types of nickel-plated aluminium plates and gold-plated kovar (nickel–cobalt ferrous alloy) were tested. The upper plate was heated by resistance heater and the bottom one cooled by heat sink underneath. See schematic Figure 19.

In the bolted joint experiment, the authors conclude dependence of thermal conductivity on a number of bolts, applied torque and average contact pressure. The comparison of conductance of clean surface contact and conductance of surface with applied thermal interface material is provided.

The experiment is well documented and accompanied with detailed uncertainty estimation including thorough investigation of heat losses to the surroundings.

2.6.2 Experimental determination of thermal resistance across linear guideways (Morávek)

In thesis [20], investigation of heat transfer trough linear guideways is executed. The aim of the study was to investigate relation between thermal resistance and size or type of guideway and its preload.

Experiment took place under atmospheric conditions and with no external load. Number of linear guideways were tested differing in size, type of rolling elements and preload.

Figure 20 depicts layout of experimental device. Note that in a completely insulated environment is present only heater. Thus final data were obtained from transient heating process.

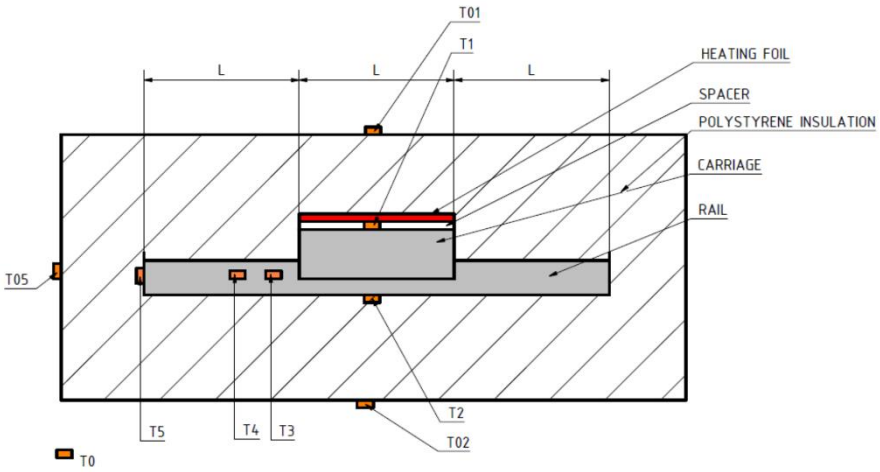

Figure 20: Experimental layout for testing thermal resistance of linear guideways, [20], (T1-T5 mark positions of internal RTD temperature sensors, T0-T05 mark position of external control RTD temperature sensor))

The study presents a comparison of computed estimation of thermal resistance and experimental data. Conclusion states that the most influential factors of linear guideways are internal preload and type of rolling elements. While size of the guideway proved to be negligible, the applied load on the carriage is expected to be another major factor.

2.7 Research of materials

For the estimation and research of thermal behaviour of bearing and housing thermal contact, an overview of used materials needs to be presented. In this chapter, an analysis of materials used for construction of spindle bearing rings and neighbouring spindle shaft and housing follows. Some general overview is provided by catalogues of bearing manufacturers, for instance [21].

2.7.1 Bearing assembly

The most frequently used units are angular contact ball bearings or bearings with cylindrical rollers mounted in pairs enabling setting of internal preload. For spindle applications there are highly demanding requirements for bearing qualities.

Used bearing must have high running accuracy and stiffness while keeping low friction. To obtain satisfactory machining precision, the bearings need to preserve minimum temperature rise over whole speed range of a spindle. Its design must fulfil following demands given by spindle application:

- High accuracy
- Minimal installation space
- High load capacity
- High stiffness
- Accommodation of axial displacements
- High speeds
- Low friction / heat generation

Consequently, most manufactures use all-steel or hybrid bearings made of high grade steel and rolling elements made of ceramics or steel of various commercial names.

Bearing rings

Generally speaking, the material mostly used for rings is high-nitrogen, carbon chromium steel hardened and tempered to range about 58-66 HRC. Variation of the steel 100Cr5 (ČSN 41 4100) under commercial name would be used, [22]. Such race material provides satisfactory corrosion resistance, fatigue strength, high degree of impact toughness, hardness and modulus of elasticity and low thermal expansion coefficient. As well good enough machinability of material before hardening is secured. The thermal conductivity would vary close to

$$k_{100Cr5} = 46\ W/mK$$

Bearing rings are usually grounded to surface roughness of Ra 0,5 – Ra 0,8 (the seat mating surfaces). The same requirements are used for housing seats.

Rolling elements

Rolling elements used for spindle applications are made of chromium carbon steel or silicone-nitride ceramics, [21].

Steel elements are used for less demanding application, especially lower speed spindles. The elements are made of similar material as their ring and are heat treated to hardness of 58-66 HRC. As stated above, the thermal conductivity would vary about

$$k_{100Cr5} \approx 46\ W/mK$$

For high precision and high speed spindles, ceramic rolling elements are more suitable. In comparison to steel, silicon-nitride ceramics provides

- Higher hardness and modulus of elasticity
- Lower density
- Much lower thermal expansion coefficient
- Higher corrosion resistance
- Electric insulation
- Insensitivity to magnetic field

Thermal conductivity of silicon-nitride ceramics is too dependent on manufacturing process and more specific data needs to be obtained from manufacturer. Range for orientation can be stated as, [23]

$$k_{Si_3N_4} \approx 29{\sim}170\ W/mK$$

2.7.2 Spindle shaft and housing

The range of steels usable for spindle shaft construction is wide, therefore let us present a representative case hardening alloy steel 20NiCrMo2-2 (ČSN EN 10084) with thermal conductivity

$$k_{20\mathrm{NiCrMo2-2}} \approx 46\ W/mK$$

Since for the spindle housing the range is even wider, only the estimated range is stated for construction steel and cast iron suitable for spindle housing construction, [24].

$$k_{\text{steel housing}} \approx 45 \sim 50\ W/mK$$

$$k_{\text{cast iron housing}} \approx 45 \sim 50\ W/mK$$

2.7.3 Lubricants

In any application, bearings must be sufficiently lubricated to function well. Regular intake of lubricant secures a thin film between relatively moving parts resulting in lower wear, lower friction coefficient, corrosion resistance and cooling of the bearing.

The outer surfaces of the ring are also lubricated during the assembly process to ease the installation and preserve the surfaces.

Direct implication of lubrication is liquid present between bearing rings and their housings affecting significantly the thermal qualities of the contact.

Varying with application, grease lubricants and oil lubricants are used in spindles. In general, low viscosity oil is used for high speed spindles. Grease lubricants are recommended, if speed requirements allow [21].

For grease lubrication, initial fill and refilling of bearing in regular intervals is required. For bearing oil lubrication, oil bath, circulating oil, oil jet, oil drop, oil mist or oil-air system is used. For detailed description see [21] or other catalogues of bearings or lubricants manufacturers.

Thermal conductivity of most of the lubricants would vary about

$$k_{oil} \approx 80 \sim 200 \text{ mW/(m K)}$$

As there is number of a different lubricants with varying thermal properties and those are additionally function of temperature and cleanliness, the exact values need to be obtained from manufacturer or experimental measurement has to be performed.

3 Experimental measurement – simplified approach

Although the theoretical predictions of the thermal contact conductance are available, none of them may be directly used to determine a thermal properties of a spindle units (necessity of experimental verification of models, [25]). Furthermore, many unknown or more-less random inputs have a significant influence on a final thermal properties and thus an experimental measurement and a comparison to those estimations is performed.

Two stage experiment was established. First, the simplified approach described in the following chapters is constructed in order to determine thermal properties of used material and thermal contact conductance of planar surfaces.

The second stage is carried out to determine the thermal contact conductance of a cylindrical contact of an outer bearing ring and a bearing housing, where presence of random inputs (such as cylindricity) is even more significant. This full scale setup also allows comparison of gathered temperature fields to field of ideal contact with no thermal contact resistance at all. The full scale experiment is described in chapter 4.

Measurements on the simplified experimental setup are presented below. First of all, a measurement with a reference specimen made of a steel of well-known thermal properties is to be taken in order to determine the actual heat flow through the object. For the following measurement the specimen made of the same material as in the full scale experiment is inserted into the measuring device and its thermal properties are determined. Moreover, two separated specimens machined to the same roughness, as the surfaces in the full scale experiment, are inserted in the same setup. A measurement follows to roughly determine the thermal contact conductance of flat surfaces under negligible contact pressure.

The setup is constructed to allow a repeatable and simple measurement of a thermal properties of other steels or materials with thermal conductivity of the same order.

3.1 Reference measurement

To measure the actual heat flow through the reference specimen made of steel of known thermal conductivity, a constant temperature gradient is produced by a heater on top and by a heat sink under the specimen. For material properties of reference material, see Table 1.

Table 1: Thermal conductivity of reference steel

T	k
$[°C]$	$[W/mK]$
20.3	44.0
35.0	44.7
50.2	45.3
80.6	46.9

3.1.1 Reference measurement - setup

A constant power input into the heater and sufficient and constant cooling power of the heat sink eventually, after the transient effect, provide linear temperature distribution. The obtained temperature profile accompanied with the known thermal conductivity leads to actual heat flow through the specimen. To minimize heat losses to surroundings and to restrict external

influences, the heater, the cylindrical specimen and the heat sink are cased in a thermal insulation material. In steady state a linear temperature distribution can be assumed and so two thermometers should be sufficient (equation (2-3). Nevertheless, four thermometers are placed along the cylindrical axis in regular intervals allowing more precise linear interpolation and reducing error of measurement.

Figure 22 depicts schematic view of the experimental setup and the Figure 23 photo of the actual experimental device.

The tested specimen is a steel cylinder with drilled holes for thermometers to measure the temperature along the axis of the cylinder. The four thermometers are sunk into thermally conductive paste and are secured with the temperature sensitive element in contact with the end of the hole.

The type of used thermometers was resistance temperature detector (RTD). See the Figure 21 for the thermometers' location and simplified dimensional insight. The actual holes for the thermometers were drilled in helical pattern to ensure their minimal influence on temperature distribution. Full technical specification is provided by technical drawings number DP1731-01-01.

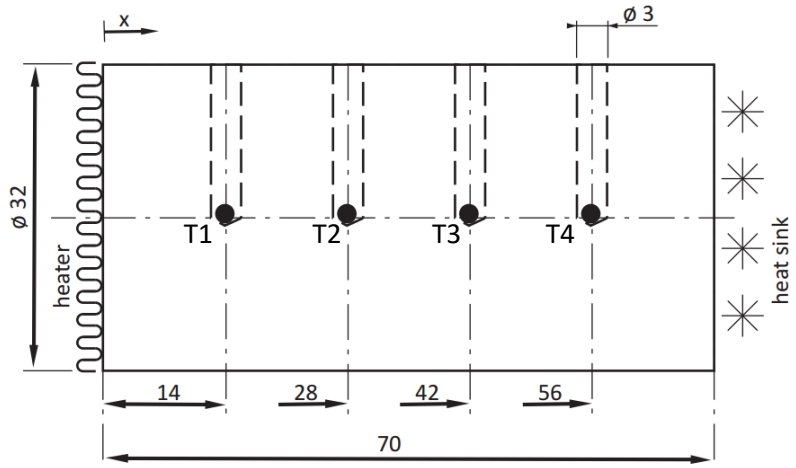

Figure 21: Detail of reference specimen layout with location of thermometers

To heat the specimen, an electrical heater is placed to the top of the cylinder. To minimize the thermal resistance of the heater – specimen contact, layer of a thermally conductive paste is spread in the interface.

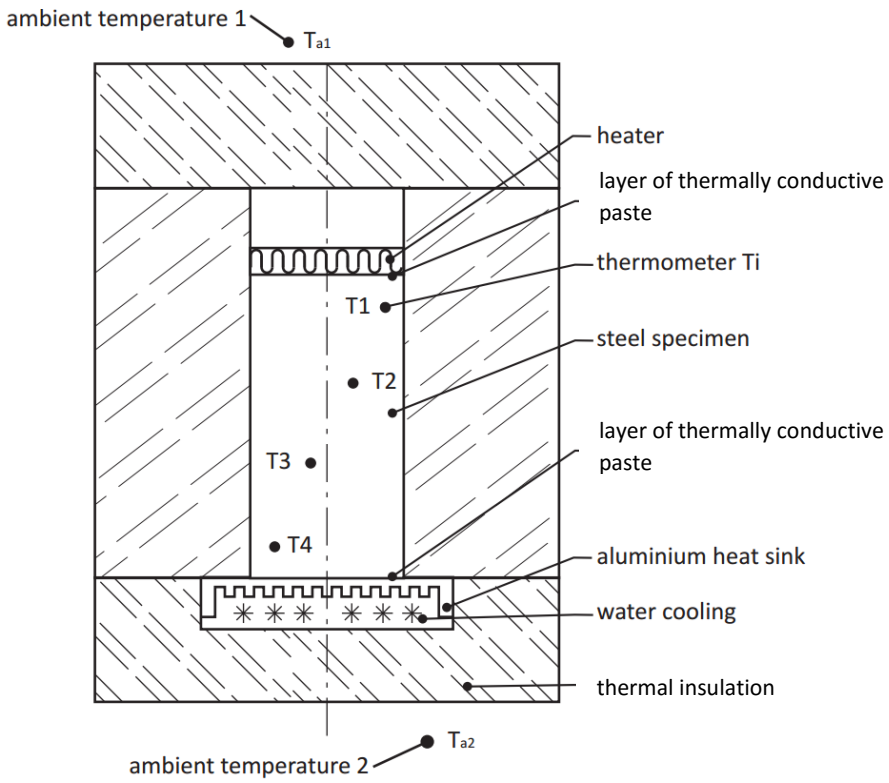

Figure 22: Schema of simplified experimental setup

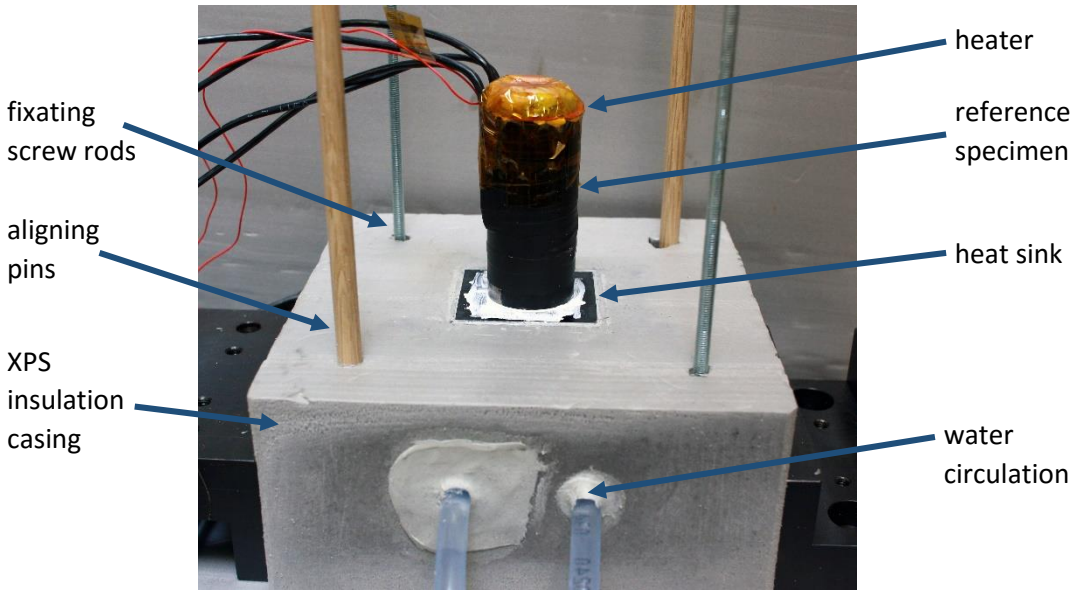

Figure 23: Photo of simplified experimental setup - heat insulation taken down, one-piece cylinder of reference steel is installed

To sink the heat from the specimen, water – cooling system is placed under the tested cylinder. Again, a thermally conductive paste is placed in the interface. The water – cooling system itself consists of a water reservoir of volume big enough to accommodate heat input without substantial temperature increase. An electrical water pump to circulate the water is at the intake of the tubing and a heat exchanger is placed in direct contact with the tested specimen. The exchanger is constructed of an aluminium and is built in a body of XPS polystyrene with drilled

input and output channels for the cooling water. At the outlet a radiator with fans is connected to the tubing to cool down the warm water by ambient air. Nevertheless, in case of simplified experiment the radiator's fans are switched off as are not applicable for such small power inputs used in this part of measurement. See schema of water cooling system in the Figure 24.

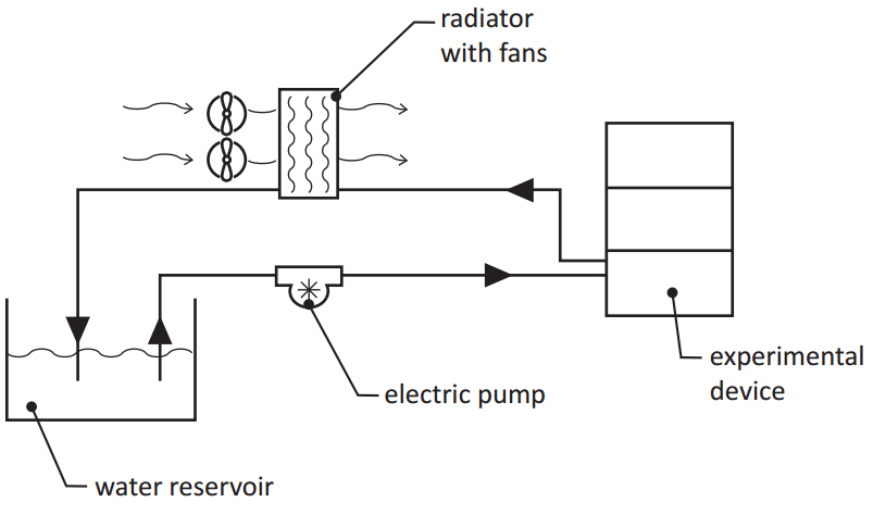

Figure 24: Schema of water cooling system, for simplified experiments with cylinders, the radiator is not used

A housing made of XPS polystyrene accommodating all the key elements consists of three detachable blocks tightened together by two screw rods. The XPS blocks are aligned against each other by two pins. Such setup allows repeatable assembly and the hand-tightened nuts produce slight pressure on the cylinder ensuring full contact of the surfaces. See Figure 23 depicting half disassembled setup with inserted reference cylinder.

3.1.2 Reference measurement – procedure

Following measurement was taken to determine the actual heat flow through a steel cylinder in the experimental device.

The experimental device including tested specimen and water reservoir was placed in laboratory with stable temperature of 20 °C and was let to temper. Precautions against direct sunlight were implemented by covering the device with XPS polystyrene boards. The water pump was set on and due to slightly different temperature of the water reservoir and the device, the temperatures of the cylinder dropped. After the transient process of tempering the cylinder to temperature of the cooling water faded out, the heater was turned on.

The measurement of the temperatures was taken under steady state conditions, which were considered to prevail after 20 minutes of temperatures not changing by more than 0.5 K. Totally flat final conditions might not be expected as all the experimental setup and the cooling circuit is a closed system with a limited heat loss to the surrounding and with two significant heat sources – the heater and the water pump.

3.1.3 Reference measurement – obtained data

In Figure 25 is shown typical time development of the temperatures along axis of the reference cylinder. Temperatures are marked from 1 to 4 ascending with its distance from the heater. In the lower figure a gradient of sum of all the temperatures is plotted. Gradient is smoothened over 100 samples to reduce influence of noise.

A sampling of temperatures is carried out at the moment of minimum of the absolute value of the gradient. Those values are used in further calculations. The sampling moment is marked in the figure by green dotted line. The smoothening of the gradient line decreases its accuracy during dynamic changes, but helps identifying steady moments. For the sampling was used a 2 s period as accurate enough but keeping the data files reasonably small.

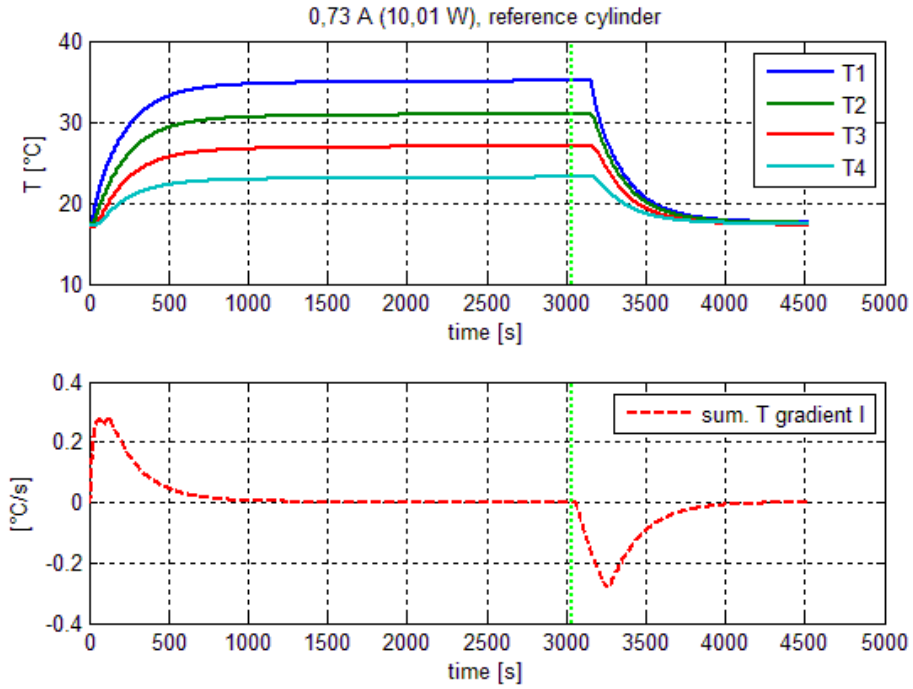

Figure 25: Temperatures vs. time in the reference cylinder, lower plot shows time gradient of sum of all the temperatures, the green line marks the sampling of the temperatures in the most steady moment

Several measurements were executed in the same manner with input power of the heater of approximately 10 W and 15 W. Sampled temperature profiles are plotted against axial coordinate in Figure 26. Data points are fitted by least square line.

Figure 26 shows that for the same power input a steady state levels up on different temperatures. This is due to slight variations of the ambient temperature. Moreover, the water in the reservoir warms up by longer series of measurement which influences the results. Nevertheless, it is the slope of the line defining the heat flow through the cylinder. See the equation (2-4) for heat flux in infinite plane wall showing that the absolute terms are subtracted and their difference determines the flux.

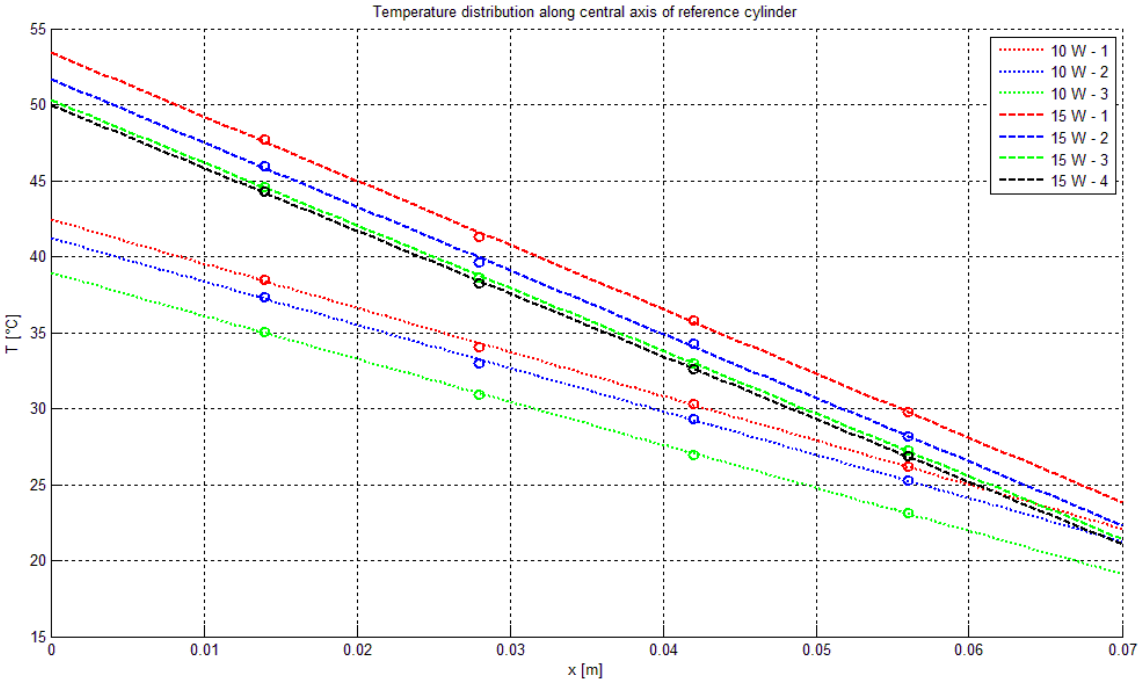

Figure 26: Temperature profiles of reference cylinder for input power 10 W and 15 W

Respecting unimportance of the absolute terms, Figure 27 depicts only the slopes obtained by individual measurement. The lines fitted closely each to other predicate usable repeatability of the experiment and lead to wide usability of the experimental setup across different ambient temperature and varying temperature of the cooling water.

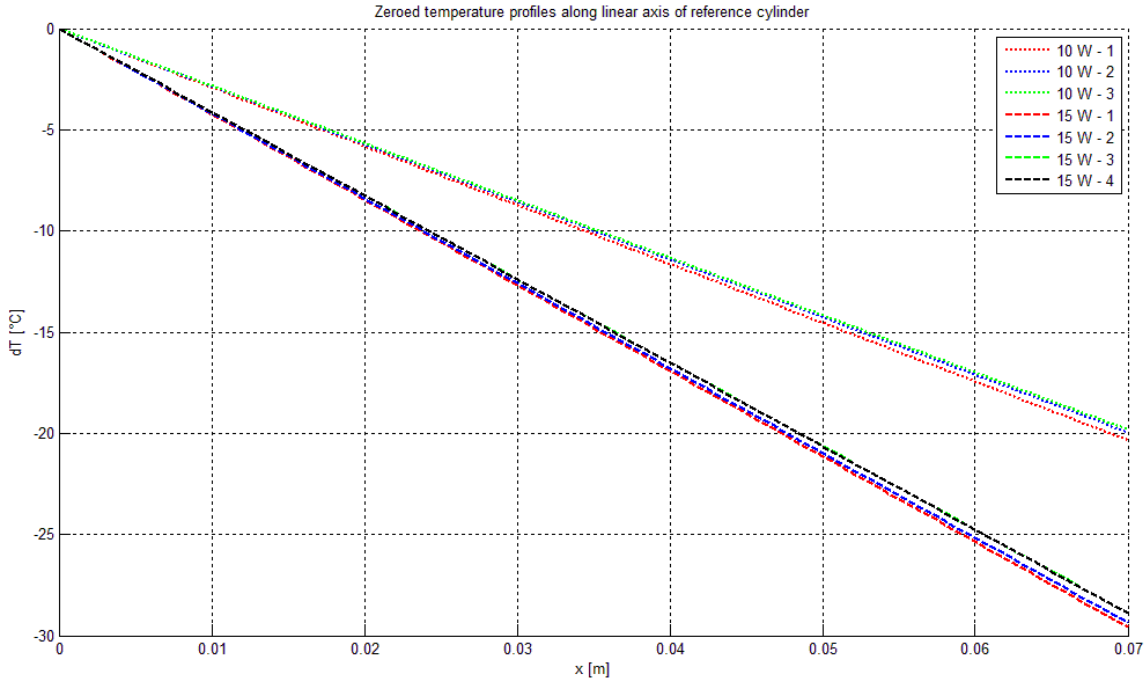

Figure 27: Temperature profiles of reference cylinder without absolute terms

Results in the Table 2 show that calculated heat flow $q\ [W]$ fits closely to power input $P\ [W]$ with average deviation of $1.32\ \%$ (and maximum deviation $3.51\ \%$). So the measuring device ensures that most of the ingoing energy is transferred through the measured specimen and diverted out of the device by cooling system.

It also shows that measurement with higher energy input does not necessarily lead to noticeably higher heat losses to the surrounding. But for higher heat flows can be expected greater insensitivity to external sources of errors such as indirect sunlight or indoor air movements.

Higher power inputs than $15\ W$ were avoided to ensure thermal stability of insulation material (XPS polystyrene).

Table 2: Reference measurement - comparison of power input and actual heat flow through the reference cylinder

	power input			ref. data	calculated	
N°	$U\ [V]$	$I\ [A]$	$P\ [W]$	$k\ [W/mK]$	$q\ [W]$	$dev.q\ [\%]$
10 W input power						
1	13.73	0.73	10.02	44.50	10.36	3.36
2	13.70	0.73	10.00	44.50	10.12	1.19
3	13.71	0.73	10.01	44.40	10.02	0.12
15 W input power						
4	16.61	0.88	14.62	44.86	1513	3.51
5	16.70	0.88	14.70	44.78	15.04	2.34
6	16.83	0.88	14.81	44.72	14.72	-0.61
7	16.84	0.88	14.82	44.71	14.72	-0.67
					avg. dev.	1.32

3.1.4 Reference measurement – data processing

In this chapter a step-by-step processing of the data presented above is provided.

First of all, the power input of the heater is calculated. As its resistance varies slightly with its temperature, the power input $P\ [W]$ was obtained from values of voltage U and current I

$$P = I\ U \qquad (3\text{-}1)$$

where I and U were read at the moment of sampling temperatures – the steadiest moment – on digital power source powering the heater. Those data are presented in "power input" section of the Table 2.

The thermal conductivity $k\ [W/mK]$ in column "ref. data" is linearly interpolated from values shown in Table 1. The temperature used for the interpolation is the average of values given by individual thermometers. Ideally the average temperature is the one at the middle plane of the cylinder.

Determination of the heat flow $q\ [W]$ begins with fitting the data by line using the least square method. One can compare the equations of a line (3-3) and of a temperature profile (3-2) and derive relation for heat flux.

$$T(x) = T_{w1} - \frac{\dot{q}}{k}x \tag{3-2}$$

$$y\,(x) = \; b + a\,x \tag{3-3}$$

which (while leaving out the absolute terms) yields to

$$\dot{q} = -k\,.\,a \tag{3-4}$$

And by transferring heat flux to absolute heat flow, the amount of heat actually being transferred through the specimen is calculated

$$q = -k \;\; a \;\; A_{red} \tag{3-5}$$

where A_{red} stands for reduced cross section area. The actual cross section is reduced to take the influence of holes for thermometers into account. The cylinder with cross section A_{red} has the same volume as cylinder with cross section A after drilling the holes. For A_{red} a simple formula is used.

$$A_{red} = \frac{V - n \;\; V_{hole}}{L} = \frac{\pi \;\; d^2 \;\; L - n \;\; \pi \;\; d_{hole}^2 \;\; L_{hole}}{4 \;\; L} \tag{3-6}$$

In case of the reference cylinder the number of holes $n = 4$, their diameter $d_{hole} = 3\ mm$, their length $L_{hole} = 16\ mm$. The length of the specimen $L = 70\ mm$ and its diameter $d = 32\ mm$. Reduction yields decrease of area by $0.8\ \%$ from A to A_{red}

$$A = \; 8.0425e^{-04}\ m^2$$

$$A_{red} = 7.9779e^{-04}\ m^2$$

To compare above calculated heat flow to power input, deviation "$dev.q$" was calculated

$$dev.q = 100\ \frac{q - P}{P}\ \% \tag{3-7}$$

3.2 Measurement of material properties

For construction of the device for measurement of the thermal contact conductance of a cylindrical interface was used a chromium-mangan steel (see Table 3 for designation). Chemical composition of used steel follows in Table 4. Table 5 shows material properties. Let us denote the steel as 16MnCr5 for the further use.

In order to verify declared material properties of the steel – which may vary slightly with individual batches and do not necessarily fit to the individual pieces used – measurement of thermal properties is described in following lines.

Table 3: Designation of steel used for experimental setups

designation	
ISO	TYPE 5 ISO 683/11-70
EURO	16MnCr5 EN 10084-94, EN 84-70
ČSN	ČSN 41 4220

Table 4: Chemical composition of the used steel, [27]

Chemical composition

C%	Si% max	Mn%	P% max	S% max	Cr%
0,14-0,19	0,40	1,00-1,30	0,025	0,035	0,80-1,10
± 0.02	+ 0.03	± 0.05	+ 0.005	+ 0.005	± 0.05

Table 5: Material properties of the used steel, [27]

Thermal Expansion	$10^{-6} \cdot K^{-1}$	►	11.1	12.1	12.9	13.5	13.9
Mod. of Elasticity long.	GPa	210					
Mod. of Elasticity tang.	GPa	80					
Specific Heat Capacity	J/(Kg•K)	460					
Thermal Conductivity	W/(m•K)	41					
Density	Kg/dm^3	7.85					
Specific Electric Resist.	$Ohm \cdot mm^2/m$	0.16					
Electrical Conductivity	$Siemens \cdot m/mm^2$	6.25					
°C		**20**	**100**	**200**	**300**	**400**	**500**

The symbol ► indicates temperature between 20 °C and 100 °C, 20 °C and 200 °C …

3.2.1 Measurement of material properties – setup

The setup used to identify the thermal properties of the steel 16MnCr5 is described in chapter 3.1 and was tested in chapters 3.1.2 to 3.2 and proved itself as usable. Now the specimen made of the reference steel is replaced by the one made of steel 16MnCr5 and another set of measurements is performed.

The rest of the setup stays unchanged. Circular heater is on the top of the cylinder. In the holes filled by thermally conductive paste are placed thermometers and are secured with their thermo sensitive elements in direct contact with the material of the specimen. The cylinder is placed on the aluminium heat sink which is cooled by water cooling system. The fans of the radiator are switched off.

The specimen inserted in the setup is shown on the Figure 28. The cylinder has holes for thermometers drilled in helical pattern to ensure minimal distortion of the temperature field (not respected in the simplified figure). The faces are ground for further experiments and to secure best possible contact with the heater and heat sink. The thermally conductive paste is spread on the mating surfaces to further facilitate heat flow through the specimen. The spacing

of the holes is modified to enable use of the cylinder for further experiments. See the technical drawings number DP1731-01-02 for full specification.

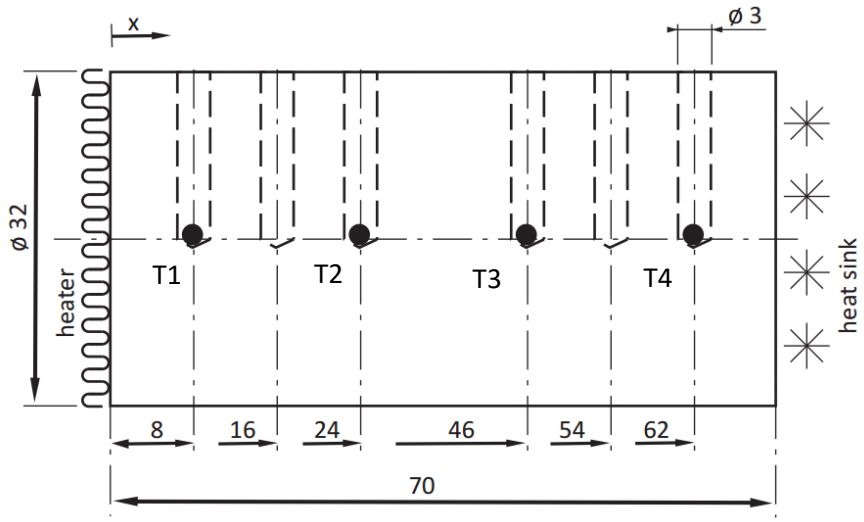

Figure 28: Specimen for investigation of thermal properties of the steel 16MnCr5

3.2.2 Measurement of material properties – obtained data

The typical time development of the temperatures is shown in Figure 29 with thermometers marked from 1 to 4 ascending with its distance from the heater as marked in Figure 28. The lower plot shows a gradient of a sum of all the temperatures. The gradient is smoothened over 100 samples to minimize the influence of the noise.

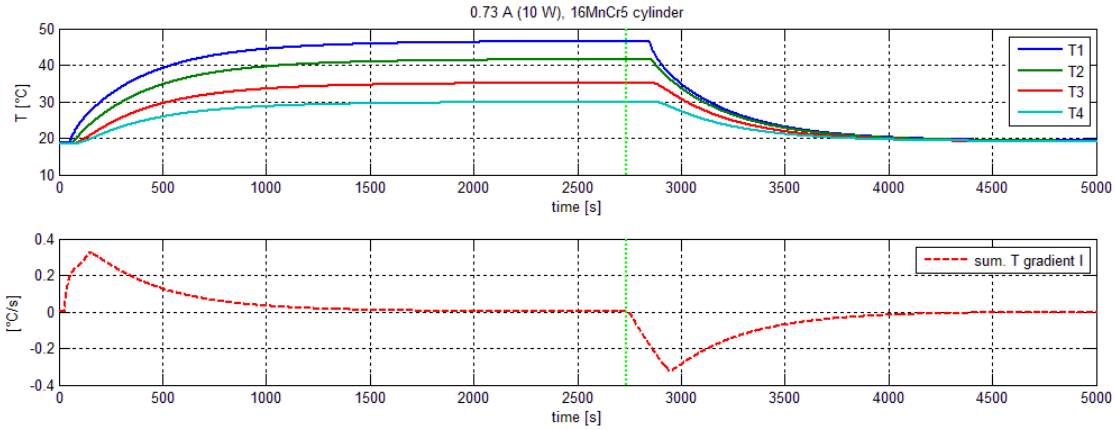

Figure 29: Temperature vs. time in the 16MnCr5 cylinder, lower plot shows time gradient of sum of all the temperatures, the green line marks the sampling of the temperatures in the most steady moment

The measurement took place in ambient temperature of 20 °C and the apparatus was shadowed from direct sunlight by XPS polystyrene boards. Before powering up the heater, the equipment was tempered to the ambient temperature and the transient state after turning on the cooling circuit was let to fade out.

At the moment of the minimal overall gradient the temperature sampling is carried out (marked with green dotted line in the plot). Those temperatures are used for further calculations.

In the same manner as with the reference cylinder, several measurements were executed using input power of the heater approximately 10 W and 15 W. The temperature profiles are plotted in Figure 30. The obtained profiles along the central axis of the cylinder were fitted by line using the least square method.

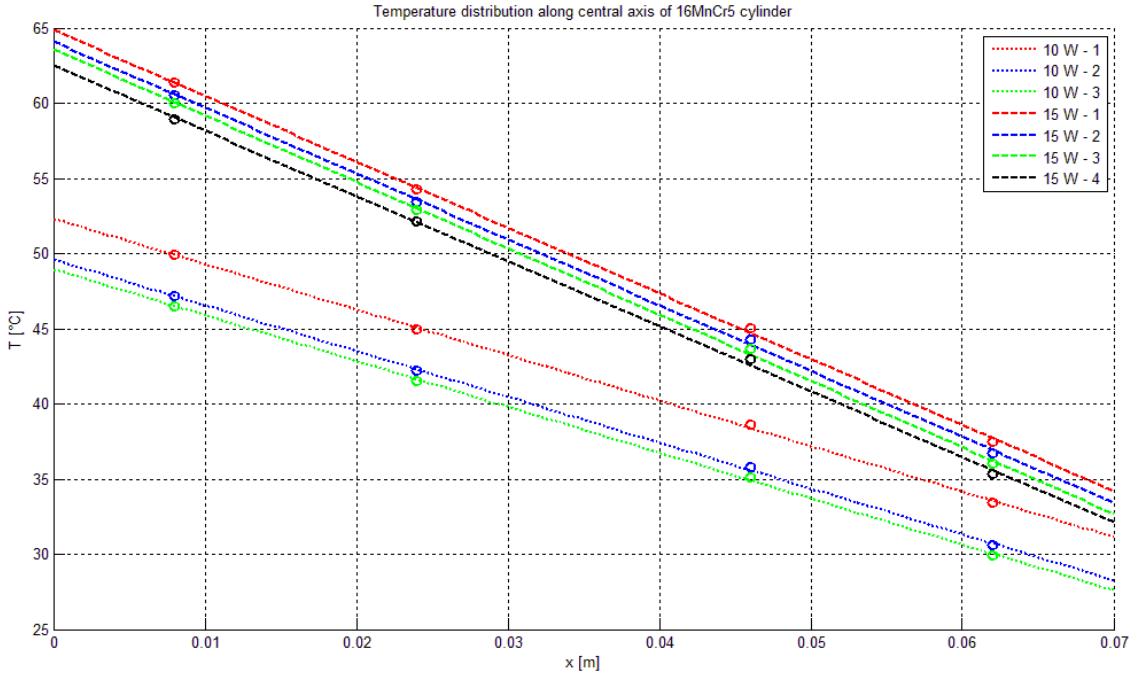

Figure 30: Temperature profiles of the 16MnCr5 cylinder for input power 10 W and 15 W

Note that lines of individual profiles in the Figure 30 vary in their absolute values, this is both due to an environmental changes as due to the temperature rise of the cooling water caused by longer series of measurement.

This effect is neglected by subtraction of the absolute terms – as explained in the chapter 3.1.3 and so more explicatory presentation of the data provides the Figure 31 plotted without the absolute terms.

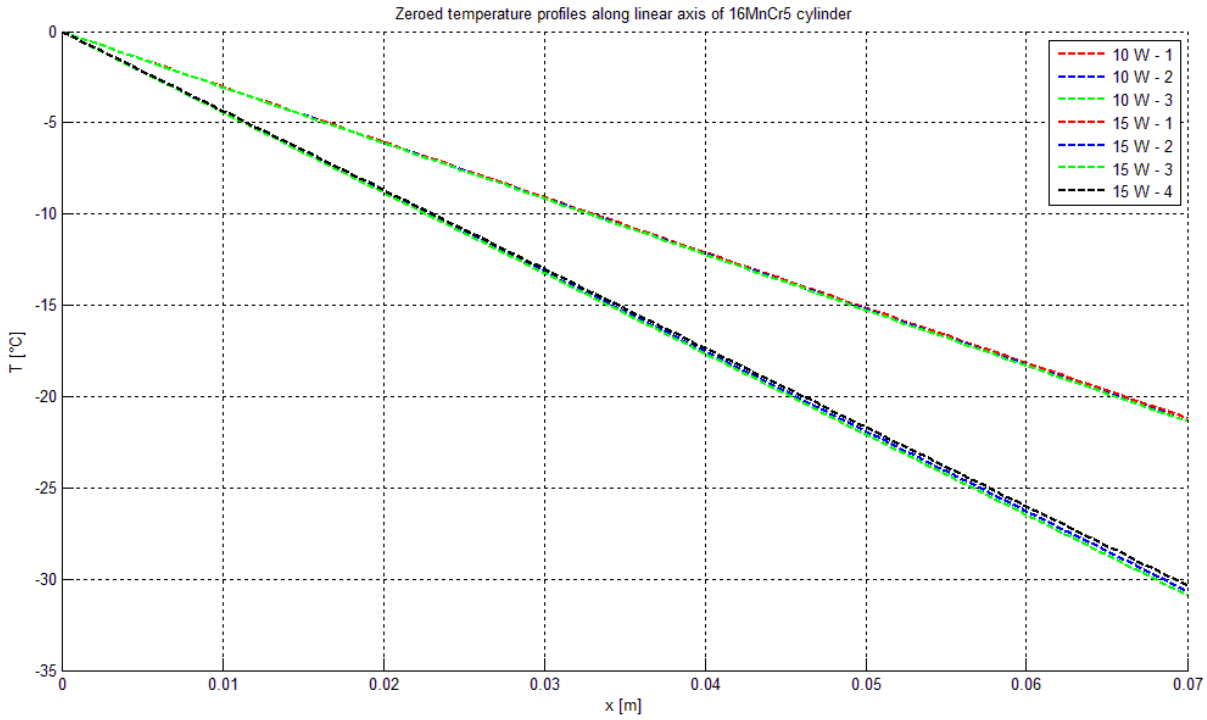

Figure 31: Temperature profiles of the 16MnCr5 cylinder without the absolute terms

With known input power – which proved itself as very close to actual heat flow through the inserted specimen – and with known slope of the lines, the thermal conductivity k $[W/mK]$ of the 16MnCr5 steel can be calculated. The results of individual measurements are presented in Table 6.

Table 6: The results of the measurement of thermal conductivity k of the 16MnCr5 steel

	power input			calculated
N°	U $[V]$	I $[A]$	P $[W]$	$k[W/mK]$
10 W input power				
1	13.91	0.73	10.15	41.93
2	13.91	0.73	10.15	41.96
3	13.84	0.72	9.96	41.63
4	13.90	0.73	10.15	41.10
15 W input power				
5	16.80	0.88	14.78	42.47
6	16.70	0.88	14.70	42.23
7	16.83	0.88	14.81	42.24
8	16.78	0.88	14.77	42.40
		average k		42.00
		uncertainty		0.32

Table 6 shows that the measured thermal conductivity $k = 42\ W/mK$ is slightly higher than the claimed one $k = 41\ W/mK$ in Table 5. Slight difference can be explained by measuring

uncertainty as well as by material difference. Nevertheless, this difference is small enough and for the next calculations is used the value of $k = 42\ W/mK$.

The uncertainty presented in the table is only of type A since random influences can be expected as major source of errors. The uncertainty also needs to be confronted with the average deviation of experimental device presented in Table 2. Further analysis of uncertainties follows in chapter 3.5 .

3.2.3 Measurement of material properties – data processing

The data processing was very close to the one described in the chapter 3.1.4 . The power input was acquired in the identical manner.

The used cross sectional area A_{red} was obtained as described in chapter 3.1.4 . However, for the conductivity measurement was respected the different number of the holes $n = 6$, leading to area reduced by $1.2\ \%$ to

$$A_{red} = 7.9455e - 04\ m^2$$

The equation (3-4) for determination the heat flux from the line slope was modified as the wanted output is changed from heat flux to thermal conductivity.

$$k = -\frac{\dot{q}}{a} \qquad (3\text{-}8)$$

And modifying the equation for power input instead of heat flow yields following

$$k = -\frac{q}{a\ .A_{red}} = -\frac{P}{a\ .A_{red}} \qquad (3\text{-}9)$$

3.3 Thermal contact resistance of planar interface

The setup used for measurement of the thermal conductivity can be easily modified for measurement of thermal contact conductance under atmospheric conditions and negligible pressure. Measuring the thermal properties of a planar interface gives a better insight into the problematics and may reveal unpredicted difficulties. Moreover, the setup enables measurement under non or minimal contact pressure which is comparable to the conditions of the cylindrical contact with a small backslash and may predict the interval of values obtained from the full scale cylindrical setup.

The measurement also serves as data collection for comparing two substantially different methods of data processing. While this section samples data at steady states, the following section 3.4.1 determines the values of the thermal contact resistance using recorded cycle including both the transient states. Comparison of obtained results shall be presented and may suggest suitability of one of the methods for further measurements.

The steady state extraction method is utilised first as it is less demanding on the measuring devise, precision of the sensors and is more insensible to environmental changes. Also the method leads to simple mathematical relations and thus is more overly robust.

3.3.1 Thermal contact resistance of plane interface – setup

While using the same experimental device described in the chapter 3.1.1 , the one-piece cylindrical specimen made of the 16MnCr5 steel is now removed and lathe turned into identical halves. Its faces ground to surface roughness $Ra\ 0.8$ are turned to mate each other. See the technical drawings number DP1731-01-03 for full specification.

While investigated contact surfaces are cleaned by technical alcohol, faces mating the heater and the heat sink are covered by thermally conductive paste. The thermometers placed into the holes were secured with direct contact with the ends of the holes and covered with thermally conductive paste as well.

Coaxiality of the two specimens – leading to full face contact – is ensured by XPS polystyrene housing. Because of the cutting process, the overall length of the cylinders is reduced. In the Figure 32 is shown simplified schema of the specimens in contact. Air gap between the surfaces is eliminated by vertical positioning of the device as well as by slight pressure produced by hand tightening of the screw rods holding all the device compact.

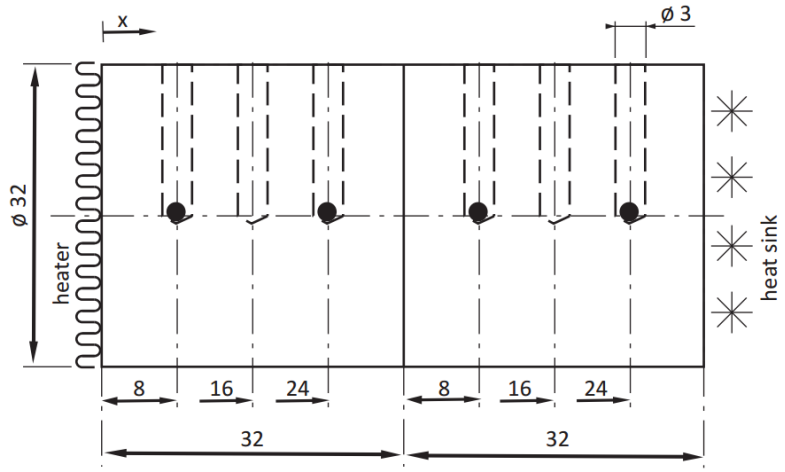

Figure 32: Schema of the separated specimens for measuring the thermal contact conductance in simplified approach

The fans of the radiator of the cooling system are kept switched off. The gap between the XPS polystyrene housing and heater surface caused by cutting the cylinder into halves is filled by XPS polystyrene spacer. The equipment was tempered up and the transient phenomena of switching on the cooling circuit was let to fade out before beginning of actual measurement and turning on the heater. Ambient temperature was 20 °C and precautions against direct sunlight were applied.

3.3.2 Thermal contact resistance of plane interface – obtained data

Figure 33 shows the typical time development of the temperatures along central axis of the cylinders. The temperatures are marked from 1 to 4 ascending with its distance from the heater. In the lower plot a gradient of a sum of all the temperatures is depicted. The gradient is smoothened over 10 samples to reduce the noise influence. The green dotted line marks the moment of the minimal gradient when the temperatures are sampled for the further calculations. For sampling was used $2\ s$ period.

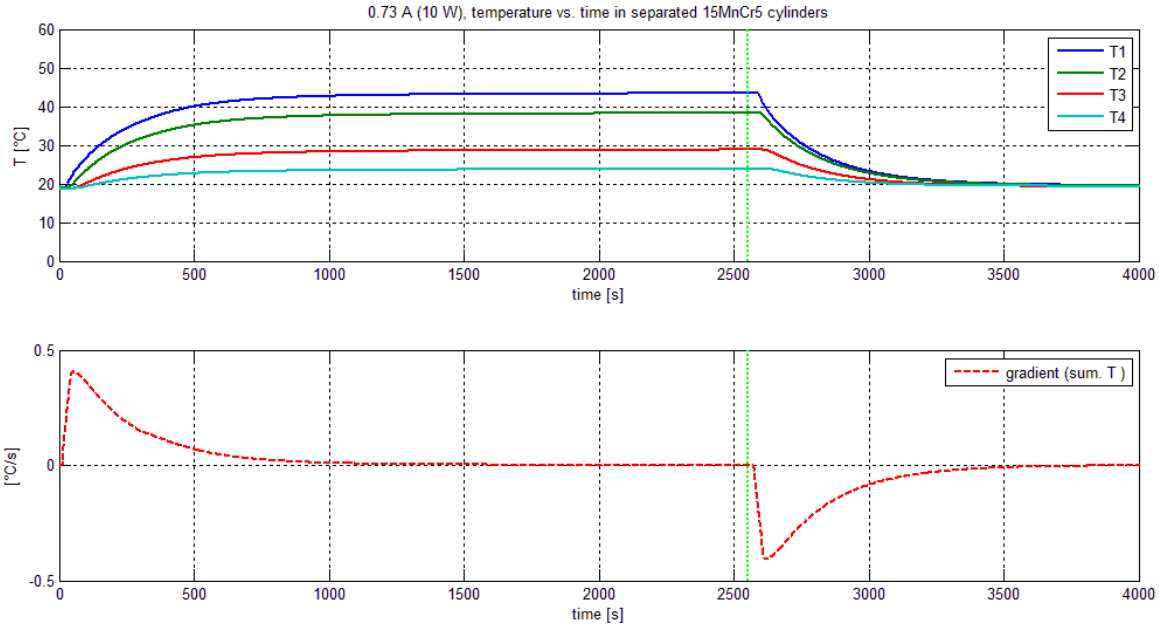

Figure 33: Temperature vs. time in the two cylinders of 16MnCr5 steel, green line marks the steadiest moment for sampling the temperatures, note the uneven distribution of the temperatures

Note that even though the overall length of the specimens was reduced and so the inner thermometers are closer to each other, temperature distribution is modified in the opposite manner – the inner temperatures have grater gap caused by the thermal resistance of the interface.

Similar measurements were taken for power inputs of $10\ W$ and $15\ W$. In Figure 34 are plotted temperature profiles along central axis of the cylinders. The data are fitted with lines by the least squares method, where the lines noted as 1 are of the cylinders next to the heater and lines noted as 2 are of the ones in contact with the heat sink. Only two profiles are plotted for clarity of the figure, other obtained profiles would vary with absolute position of the lines, but their slope would be very close to the presented one and the temperature drops at the interface ΔT would be very similar as well. Detailed data of all the measurement are shown in the Table 7.

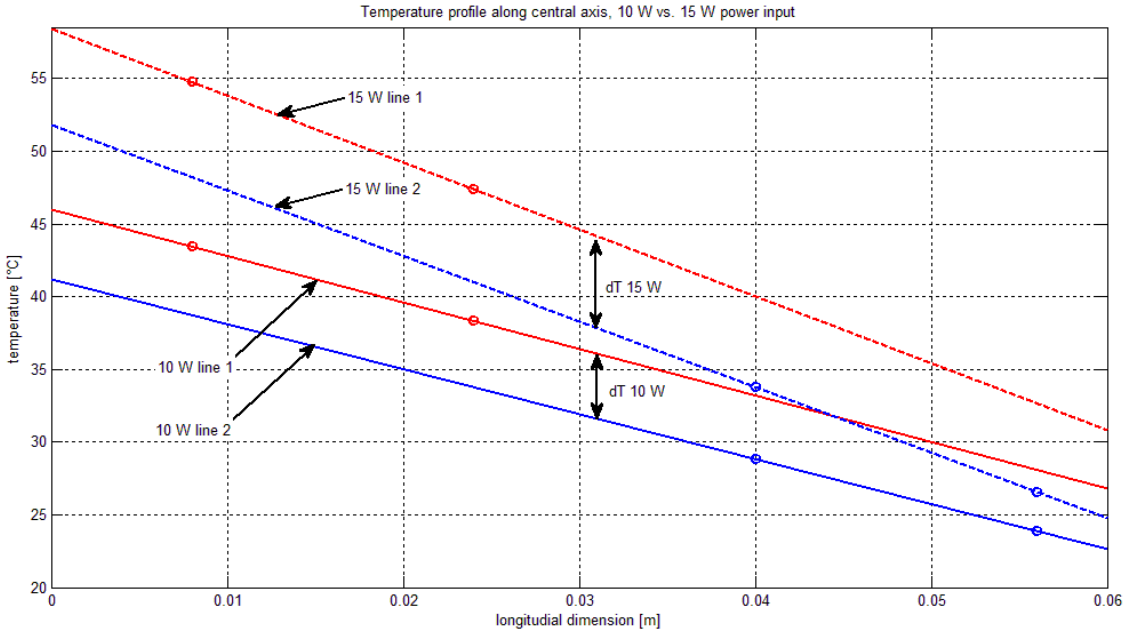

Figure 34: Temperature profiles along the central axis of the cylinders, only one representative for each power input is shown, temperature drops at the interface ΔT marked in the figure as dT

Note that not only the slope rises with the increasing power input but the temperature drop at the interface grows as well.

While for all the previous calculations the heat flow was determined from the provided power input, the greater thermal resistance of the assembly of two cylinders may cause significantly higher heat loses to the surroundings and so the heat flow is furthermore calculated as the average of the rates through individual specimens using the identified thermal conductivity $k_{16MnCr5} = 42\ W/mK$.

Calculated values of thermal resistance of the interface obtained by individual measurements are presented in Table 7. The power input section of the table shows data read on the power source. The extrapolated section contains values of the temperature drop ΔT which is obtained by extrapolating the data to the coordinate of the interface. The last section contains values of the thermal contact resistance R_c calculated using the extrapolated temperature drop and heat flow obtained by temperature profile slope and experimentally determined thermal conductivity k.

Table 7: Thermal contact resistance R_c calculated from repeated measurements

	power input			extrapol.	k=42
N°	$U\ [V]$	$I\ [A]$	$P\ [W]$	$\Delta T\ [K]$	$Rc[Km2/W]$
10 W input power					
1	13.95	0.73	10.18	4.52	3.43E-04
2	13.99	0.73	10.21	4.80	3.66E-04
3	13.99	0.73	10.21	4.48	3.39E-04
15 W input power					
4	16.87	0.88	14.85	6.34	3.31E-04
5	16.89	0.88	14.86	6.83	3.54E-04
6	16.89	0.88	14.86	6.37	3.32E-04
			avg. R_c		3.44E-04
			uncertainty		1.11E-05
			uncertainty [%]		3.22

Note that the actual heat flow through the interface does not inflict any significant changes of the contact resistance of the interface. The values across the various power inputs are approximately constant and repeatable. The type A uncertainty is shown as the prevailing one since major random error sources are present.

Let us now compare the acquired contact resistance with the models presented in the section 2.4 .

Because the pressure on the interface was insignificant, the resistance of the interface would be mainly determined by gap conductance. To further refine the estimation, the gap conductance may be summed up with spot conductance contribution. The contribution of a radiation conductance over the interface for the temperatures limited under 50 °C is of lower orders and is not taken in account. Higher temperatures of the interface are not considered because of the limitation by the XPS polystyrene insulation temperature stability. Moreover, the temperatures of the interface in the actual spindle application should not exceed the stated values significantly.

Table 8 shows estimations of the gap resistance calculated by Yuncü – eq. (2-34), by Yovanovich – eq. (2-36) and by Wahid and Madhusudana – eq. (2-37). Calculation details are presented in following chapter 3.3.3 .

Table 8: Estimation of gap contact resistance

gap resistance	$R_g[Km^2/W]$
Youncü	7.70E-05
Yovanovich	6.35E-05

As the specimens were placed without an actual gap and with slight pressure, let us estimate the solid spot conductance contribution. The Table 9 presents values of solid spot resistance determined by models of Cooper, Mikic, Yovanovich – eq. (2-29), Mikic – eq. (2-30) and Yovanovich – eq. (2-31). The models for plastic deformation of asperities were used since the

plastic deformation is prevailing for given parameters (see chapter 2.4.3). Details and input values for the calculations are provided in the 3.3.3 .

Table 9: Estimation of solid spot resistance

solid spot resistance	$R_s[Km^2/W]$
Cooper, M. , Y.	6.90E-04
Mikic	5.53E-04
Yovanovich	5.55E-04

The values of spot and gap conductance (resp. resistance) may be simply summed up to obtain the total contact conductance – see eq. (2-39). As the values presented in the Table 8 and Table 9 may be combined arbitrarily, let us find the value interval by summing the two highest and the two lowest conductivities respectively.

The following Table 10 shows the interval bordered by combined Yovanovich's model of gap conductance and Mikic's model of solid spot conductance at the lower limit and by Youncü's model of gap conductance and Cooper's model of solid spot conductance at the upper limit.

Table 10: Interval of combined contact resistance

	gap resistance	s. spot resistance	$R_c[Km^2/W]$
min	Yovanovich	Mikic	5.7E-05
max	Youncü	Cooper, M. , Y.	6.93E-05

The model values are of one lower order than the experimental ones. Since the models for the gap conductance have been proved accurate enough for the flat metal surfaces under low pressures – see the [19] experiment – other sources of errors must be identified.

The values of gap resistance are by order lower than the values of solid spot resistance which is corresponding to data presented by [19]. This means the error is mainly by combination of measurement uncertainty and estimation of the gap resistance.

For the analytical estimations were used only table values of the material properties, often calculated by approximate relations from related qualities. See the following chapter 3.3.3 for input data and the chapter 3.5 analysing error sources.

3.3.3 Thermal contact resistance of plane interface – data processing

Let us describe the manner in which the above presented values were obtained. The experimental contact resistance processing is described first, the description of estimating the gap and solid spot conductance follows.

Experimental data processing

The temperatures were sampled in the steadiest moment during the measurement as shown in the Figure 33. The temperature points are fitted with one line for each specimen using the least square method, see graphically in the Figure 34, gaining two line equations

$$T(x) = a\,.\,x + b \qquad (3\text{-}10)$$

By evaluation of the equation of each line at coordinate of interface $x = 0.032\ m$, the theoretical temperature drop at the interface is calculated

$$\Delta T = (0.032a_1 + b_1) - (0.032a_2 + b_2) \quad (3\text{-}11)$$

The actual thermal contact resistance is gained as fraction of temperature drop and heat flow as states the eq. (2-6).

$$R_c = \frac{\Delta T}{\dot{q}} \quad (3\text{-}12)$$

where the heat flux $\dot{q}\ [W/m^2]$ is calculated as the mean of the heat fluxes in the individual specimens.

The heat fluxes are determined from the slope of the lines as is shown in the chapter 3.1.4 by evaluating the equation (3-4)

$$\dot{q}_\iota = -k\,.\,a_i \quad (3\text{-}13)$$

where the $k = 42\ W/mK$ is the experimentally identified value from measurement described in chapter 3.2 .

Gap resistance evaluation

For estimation of the gap conductance were used models reviewed in the chapter 2.4.6 . Critical for correct evaluation of the gap conductance are the input parameters. The Table 11 shows values used for calculations.

Table 11: Input parameters for the evaluation of the models

parameter	notation	unit	value
th. conductivity - air	k_g	W/mK	0.0271
th. conductivity - 16MnCr5	k	W/mK	42
interface temperature	T_{int}	K	313.15
atmospheric pressure	p_{atm}	Pa	101325
Avogadro constant	R	$J/molK$	8.31446
Prandtl number - air	Pr	-	0.711
specific heat ratio	γ	-	1.4
th. accommodation coeff.	α	-	0.8
surface distance	δ	m	0
surface roughness	Ra	m	$8.00E-07$
surface roughness RMS	σ	m	$1.00E-06$
mean abs. slope of profile	$tg\theta$	-	0.7
Young's modulus	E	Pa	$2.10E+11$

The used interface temperature T is estimated from the measured data, nevertheless, the gap conductance is limited function of the interface temperature and its small deviation has minor effect.

Potential error source is thermal accommodation coefficient value. It was not possible to measure directly and so was used value extrapolated from table presented by [13]. According to authors of the study the value of the accommodation coefficient varies with the surface quality including the machining, the aging process and surface impurities. Thus the coefficient – having major influence on the value of the conductance – seems to be considerable mean of potential improvements.

Another uncertain input RMS of the surface σ which was not measured directly but estimated by relation (2-19) from the value of Ra. While the relation was recognized as reasonably accurate - [5], direct roughness measurement of σ may be additional contribution to greater accuracy.

Another indirectly determined surface quality $tan\theta$ was estimated by relation (2-21) which – although is used within its interval of validity – is recognized as not enough accurate, [9].

Solid spot resistance evaluation

Models presented in chapter 2.4.4 were evaluated using the same set of input parameters as presented in the Table 11 extended by microhardness H and contact pressure P.

The microhardness was estimated by using the equation (2-22). Since the relations for the microhardness presented in the chapter 2.4.2 were commented as underestimating the true values, [5], the relation (2-22) was chosen as the one returning the highest values of the microhardness and was preferred as not as overly complex as the relation (2-23).

$$H = 3\sigma_u = 3 * 7e8 = 2.1e^9\ Pa \qquad (3\text{-}14)$$

For better estimation, series of measurement of Vickers' hardness should be performed followed by microhardness calculation using the equation (2-23).

The major source of error for the solid spot conductance is the estimation of applied pressure. Since the setup was designed for determination of the material properties, it lacks a force sensor for measuring applied force on the cylinders. The hand tightened nuts provide only slight pressure ensuring full contact of all inserted parts. The applied pressure was estimated with a weight scale placed under the device while tightening the nuts loose on the compressed surface of the device. The pressure P is calculated as sum of contributions due to gravity force of the upper specimen and the applied force during the assembly of the setup. The value of tightening force expressed in kg measured by the scale was $5\ kg$.

$$p = \frac{5g + \pi\frac{d^2}{4}L\,\rho g}{\pi\frac{d^2}{4}} = 63\,453\ Pa \qquad (3\text{-}15)$$

where g stands for gravitational acceleration, d for specimen's diameter, L for its length and ρ for material density (Table 5).

3.4 Thermal contact resistance of the planar interface – dynamic approach

This chapter utilises the data gained in the chapter 3.3 , no other measurement was made. On the contrary not all the data recorded previously were possible to reuse in this chapter and so the data base is for the following calculations restricted. For details about setup and measuring process see the chapter 3.3 .

To enable comparison of the results obtained from steady state presented in the Table 7 with results of dynamic approach, the temperature time development was recorded including both the transient states. Therefore, the recording started before the switching on of the heater and was stopped after cooling down of the switched off device. Since such procedure is extremely time demanding, only one such experiment was completed.

3.4.1 Dynamic simulation – layout

To extract data from the transient state, the cylindrical specimens were substituted by one dimensional model. Figure 35 depicts the substitution of the two cylinders with four thermometers and aluminium water cooled heat sink by 8 linear 2-node elements.

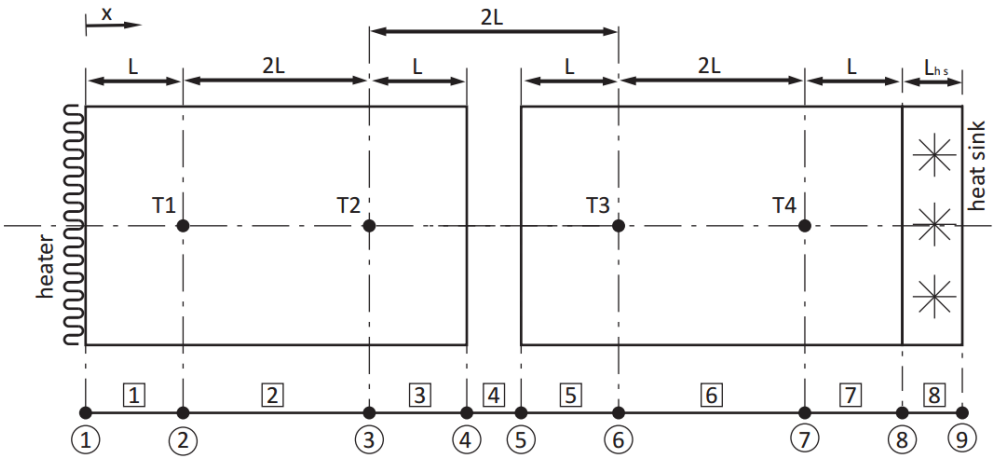

Figure 35: One dimensional FEM substitution of the cylinder assembly

Note that the thermal contact resistance is inserted element number 4 while having no physical thickness from macroscopic point of view.

See the technical drawing number DP1731-01-03 for full specification of the two identical specimens and appendix A for dimensional and material details.

The usage of one dimensional model does not reflect the heat dissipation to the surroundings, but this should not imply greater error than in ones of % - see reference measurement verifying construction of the setup in the chapter 3.1 . Furthermore, the heat capacity of the specimens and of the heat sink were tuned up to compensate the influence of the radial heat flow.

The node number 1 represents the top surface of the upper cylinder and serves for application of boundary condition of constant heat flow from the heater.

The second boundary condition is constant temperature at node 9 maintained by water circulation.

For each i^{th} element was compiled an equilibrium equation consisting of thermal transmissibility matrix $\boldsymbol{K}_i$, thermal inertia matrix $\boldsymbol{C}_i$, temperature vector $\boldsymbol{T}_i$, its time derivation $\dot{\boldsymbol{T}}_i$ and vector of nodal heat flows $\boldsymbol{Q}_i$. The equilibrium equation stands

$$\boldsymbol{C}_i\dot{\boldsymbol{T}}_i(t) + \boldsymbol{K}_i\boldsymbol{T}_i(t) = \boldsymbol{Q}_i(t) \qquad (3\text{-}16)$$

where the matrixes have following forms

$$\boldsymbol{T_i} = \begin{bmatrix} T_{i1} \\ T_{i2} \end{bmatrix} \qquad \boldsymbol{Q_i} = \begin{bmatrix} q_{i1} \\ q_{i2} \end{bmatrix} \qquad \text{(3-17 a, b,}$$

$$\boldsymbol{K_i} = \begin{bmatrix} 1 & -1 \\ -1 & 1 \end{bmatrix} \frac{Ak}{L} \qquad \boldsymbol{Q}_i = \begin{bmatrix} 1 & 0 \\ 0 & 1 \end{bmatrix} \frac{\rho\, c_p\, A\, L}{2} \qquad \text{c, d)}$$

where A stands for cross section of an element, L for its length and $\boldsymbol{q_{i1}}$, $\boldsymbol{q}_{i2}$ for power rate through the beginning and end node of i^{th} element respectively. The values of density ρ and specific heat c_p are stated in the Table 5 and the thermal conductivity $k_{16MnCr5} = 42\ W/mK$ was measured in chapter 3.2 .

The compiled matrixes of whole assembly $\boldsymbol{K}_{1,2}$ and $\boldsymbol{C}_{1,2}$ are presented in the appendix A. The matrixes were assembled for elements number $1{\sim}3$ and for $5{\sim}8$ respectively, which leaves the resistance element number 4 free as the connecting one for parametrization. The left and the right element assembly are denoted as 1 and 2 respectively. Since the interface has no physical length (macroscopically), the connecting transmissibility matrix of the 4th element stands

$$\boldsymbol{K_4} = \begin{bmatrix} 1 & -1 \\ -1 & 1 \end{bmatrix} \frac{A}{R_c} = \begin{bmatrix} 1 & -1 \\ -1 & 1 \end{bmatrix} A\, h \qquad \text{(3-18)}$$

Once the left and right part of the assembly are summed up and initial guess of conductance of element number 4 is submitted, the system can be rewritten as follows

$$\boldsymbol{C}\dot{\boldsymbol{T}}(t) + \boldsymbol{K}\boldsymbol{T}(t) = \boldsymbol{Q}(t) \qquad \text{(3-19)}$$

and the equilibrium equation in time domain can rewritten in frequency domain by Fourier transform

$$i\ \omega\ \boldsymbol{C}\ \boldsymbol{\tau}(\omega) + \boldsymbol{K}\ \boldsymbol{\tau}(\omega) = \boldsymbol{q}(\omega) \qquad \text{(3-20)}$$

which yields expression for system transfer function $\boldsymbol{H}$

$$(i\ \omega\ \boldsymbol{C} + \boldsymbol{K})\ \boldsymbol{\tau}(\omega) = \boldsymbol{q}(\omega) \qquad \text{(3-21 a}$$

$$\boldsymbol{Z}\ \boldsymbol{\tau}(\omega) = \boldsymbol{q}(\omega) \qquad \text{b}$$

$$\boldsymbol{H} = \boldsymbol{Z}^{-1} \qquad \text{c)}$$

Corresponding parts of the transfer function $\boldsymbol{H}$ can be now compared to measured partial transfer functions. The input excitation (heat flow) were was applied on the node 1 and the temperatures were measured at the nodes $2,3,5,7$. Based on this input-output relation, following transfer functions were identified

$$\widetilde{\boldsymbol{H}}_{12}\ ,\ \widetilde{\boldsymbol{H}}_{13}\ ,\ \widetilde{\boldsymbol{H}}_{16},\ \widetilde{\boldsymbol{H}}_{17}$$

where the functions in frequency domain were obtained as ratio of fast Fourier transform of the temperature time response and fast Fourier transform of excitation on the heater in time domain as follows

$$\widetilde{\boldsymbol{H}}_{1j} = \frac{\mathcal{F}\left(\boldsymbol{T}_i(t)\right)}{\mathcal{F}\left(\boldsymbol{Q}_i(t)\right)} \qquad \text{(3-22)}$$

To identify if the correction to the guess based on steady state is needed, the corrective contribution $b\boldsymbol{uv}^T$ is introduced to be added to Z matrix. The minima of coefficient b marks the best initial guess. The coefficient b is found from following equation

$$\boldsymbol{O}^{\boldsymbol{T}}\,(\boldsymbol{Z}+\boldsymbol{buv}^{\boldsymbol{T}})^{-\boldsymbol{1}}\boldsymbol{Q}=\widetilde{\boldsymbol{H}} \qquad (3\text{-}23)$$

where the $\boldsymbol{O}$ stands for the output matrix extracting the elements corresponding to the measured partial transfer functions. And the $\widetilde{\boldsymbol{H}}$ stands for $\widetilde{\boldsymbol{H}}=[\widetilde{\boldsymbol{H}}_{12}\ \ \widetilde{\boldsymbol{H}}_{13}\ \ \widetilde{\boldsymbol{H}}_{16}\ \ \widetilde{\boldsymbol{H}}_{17}]^{T}$. The correction term $b\boldsymbol{uv}^T$ stands for following

$$b\boldsymbol{uv}^T=b\begin{vmatrix}1\\-1\end{vmatrix}\,|1\quad -1|$$

3.4.2 Dynamic simulation – obtained values

The previously obtained data were modified to present only the temperature rise over the initial temperatures. To ensure the switch-off transient state finishes back on $0\ °C$, the slow creep of the temperatures was zeroed by the temperature rise measured in water (therefore the water reservoir keeps temperature rise $T_{water}=0\ °C$ for all the time period). See Figure 36 for refined values used for dynamic analysis.

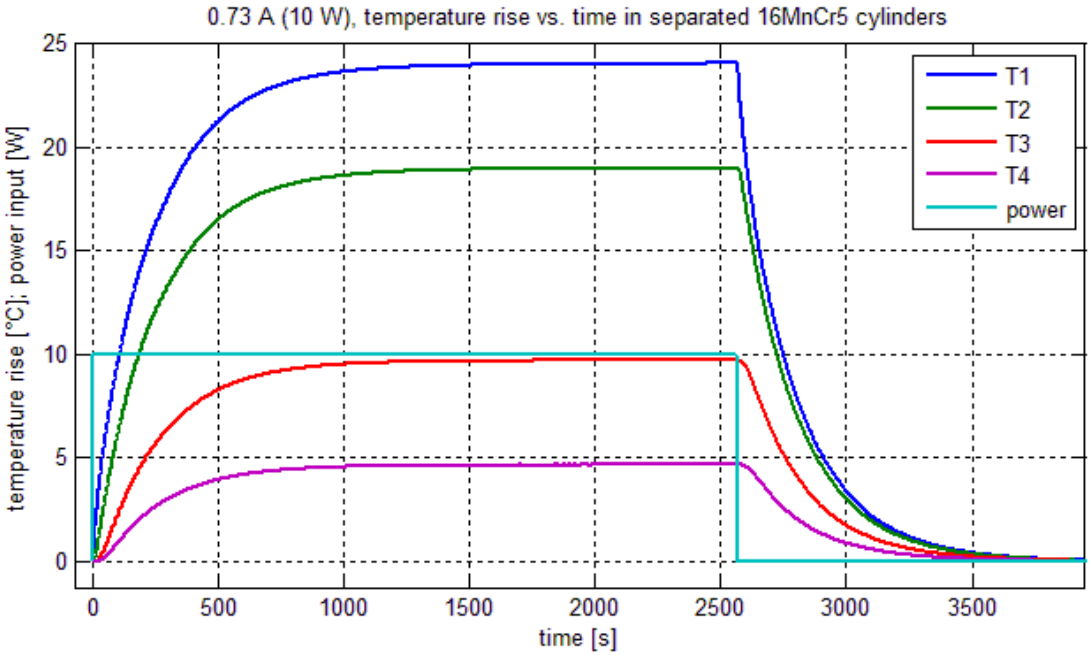

Figure 36: Temperature rise in separated 16MnCr5 cylinders, the light blue line represents power input to the heater

Now the data were fast Fourier transformed and processed as shown by eq. **(** 3-22) to obtain partial transfer functions. Due to experimental origin of the data, a significant noise occurred. Not to carry the noise further in calculation, obtained curves were fitted by rational function by the least squares method. See Figure 37 for plotted partial transfer function.

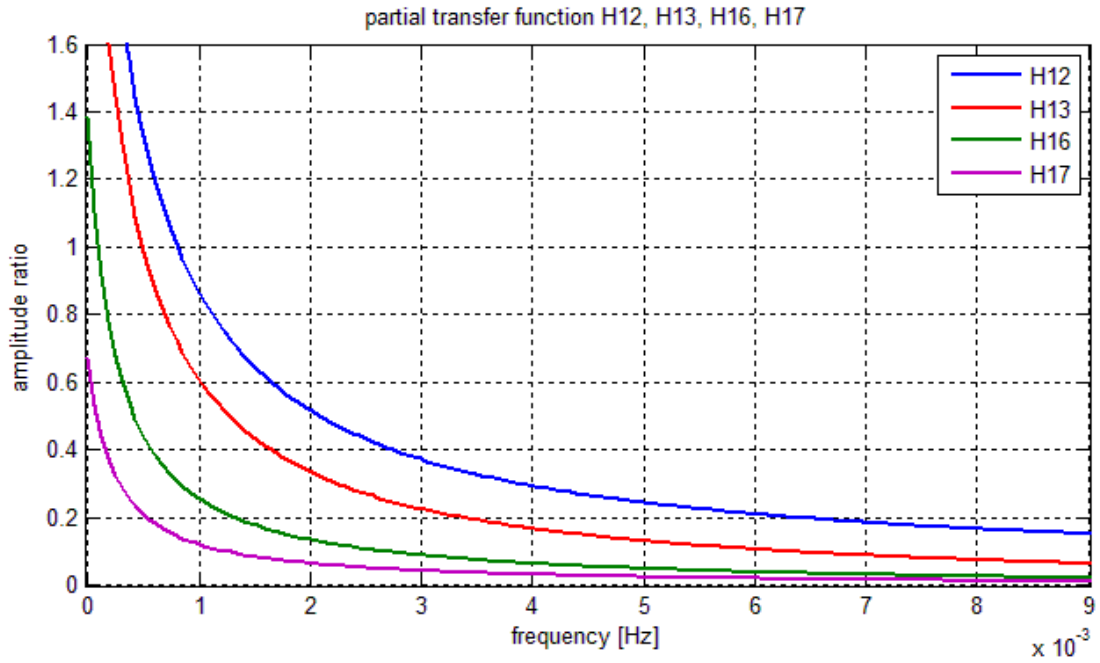

Figure 37: Partial transfer function, for illustrative reasons, only substitution by rational function is plotted

By several iterative changes of initial guess of k_{40} and localizing the minima of correction member b by eq. (3-20), the wanted value of thermal conductance of the fourth member k_4 $[W/K]$ is found. The gained value stands

$$k_4 = 2.8598\ W/K$$

which leads to thermal contact conductance by dividing the k_4 by area of contact A

$$h_c = \frac{k_4}{A} = 2.9096e^3\ W/m^2K$$

or to thermal contact resistance as follows

$$R_c = \frac{1}{h_c} = 3.4967e^{-4}\ Km^2/W$$

Subsequently the eq. (3-19) can be completed and solved for $\boldsymbol{T}(t)$ by fifth order Runge-Kutta method. For verification, the resulting temperature time development can be compared to the measured one, Figure 38. The plotted data are very consistent and thus the curves overlap each other on major part of the figure.

For comparison of thermal contact conductance determined from steady state and the one obtained by dynamical approach, see Table 12.

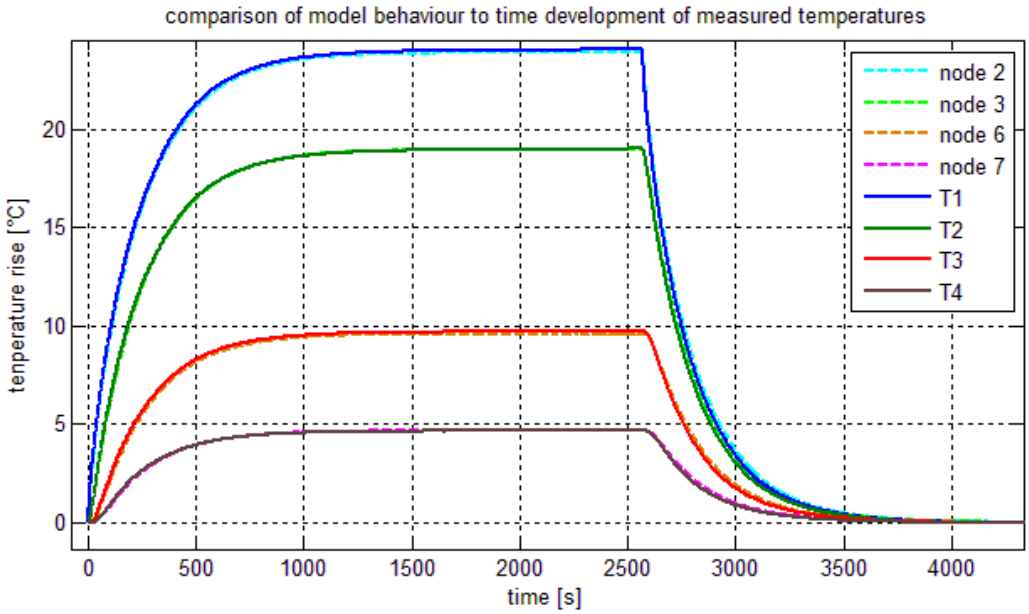

Figure 38: Comparison of model time behaviour to measured temperature rise

Since the one dimensional model does not fully cover the behaviour of the system, some tuning of parameters was necessary. First, to obtain the corresponding steady state level, the power input had to be increased by $4\ \%$ to cover the heat dissipation through the insulation in radial direction. Furthermore, the assumption of constant temperature of the water circulating through the heat sink does not correspond the real situation. Thus the thickness of the heat sink had to be multiplied approximately by factor of 3 to substitute the water heat accumulation and temperature rise.

To obtain the same transient state, the specific heat c_p of the 16MnCr5 steel had to be increased by $15\ \%$ to cover heat capacity of the insulation. See Table 12 for specific values and appendix A for input data and Matlab script.

Table 12: Comparison of thermal contact resistance calculated by evaluation of steady state and transient state respectively, tuned parameters are presented below

	satate	
	steady	transient
$R_c\ [m2K/W]$	3.44E-04	3.50E-04
$P_{input}\ [W]$	10	10.4
$c_p\ [J/kgK]$	460	530
$L_{hs}\ [mm]$	-	35

Comparing the presented time development and parameters of the model to the real system, one can conclude, that the obtained results are transposable. Thus thermal contact resistance value can be obtained by steady state evaluation and afterward used in dynamic model and conversely. Nevertheless, to iteratively tune the FE model and to measure sufficient amount of data is a time demanding process. Therefore, and accordingly to recommendation of [18], the steady state approach is utilized for further measurement.

3.5 Estimation of uncertainties of the simplified experiment

Let us now identify the most influential uncertainties common for the 3.1 to 3.3 sections.

The measuring device

Even though the device is designed to ensure the maximum possible majority of the heat flow is transferred through the specimen toward the heat sink, the insulation material XPS polystyrene has non-zero thermal conductivity and dissipates some of the energy to the surroundings.

The polystyrene thermal conductivity varies in the interval of $k_{XPS} = 0.035 \sim 0.045\ W/mK$. It is of 3 orders lower than the conductivity of the steel $k_{16MnCr5} = 42\ W/mK$. Still the dissipating heat influence the values of the measurement. However, the only way of total elimination of this source of error is a vacuum chamber and so sufficiently insulated devise verified by reference measurement is acceptable.

Material properties

The thermal conductivity of steel 16MnCr5 measured in the chapter 3.2 suffer with the error of the measuring device (average $1.3\ \%$, max $3.5\ \%$) as well as with its own type A uncertainty of $\sim 0.3\ \%$.

Furthermore, both the thermal conductivity of the steel and of an air are temperature dependent, which incorporates another source of minor error.

Input power uncertainty

Not only the power source displays the provided values of the voltage and the current with its measuring error, but the long power line to the heater behaves as resistance losing heat to the surroundings.

However, errors in electrical setup are marginal in comparison to the others.

The error of the thermometers

The thermometers placed in tempered environment measure the temperature with maximum difference under $0.1\ K$ which does not guarantee their absolute accuracy, but ensures their difference – most important for the calculation – is precise in order of $0.1\ °C$.

A more influential error connected to the measurement is the placement of the thermometers. While the machining of the holes for the thermometers does not inflict any significant error (position error of maximum order of $10e-4\ m$).

The prevailing error source is the position of the actual contact spot of the sensitive element of the thermometer to the end face of the hole – which may vary approximately by $0.5\ mm$.

4 Experimental measurement – full scale setup

The thermal conductance of the interface of outer bearing ring and bearing housing is more complex problematics than conductance of planar interface. More random inputs are present and the actual contact pressure is difficult to utilize.

In contrast to inner bearing ring, the outer one is installed into the position with slight backslash – leading to theoretically pure gap conductance through the actual air gap. In practise, this does not stand true for several reasons.

Even perfect cylindrical surfaces would get to direct contact at one point as the ring would sit in its housing.

The backslash emerging from grinding the surfaces offset from their nominal dimensions is very small and often of the same order as achieved cylindricality – thus imperfectly cylindrical surfaces would create multiple contacts around the circumference, some of them under considerable pressure.

The temperature rise during spindle activity would deform outer ring significantly more than the housing as it is incomparably slender. The temperature changes would not only cause varying thermal properties of the material and interstitial fluid, but would change the gap thickness or the contact pressure inflicting substantially greater variations of the contact resistance.

Let us now experimentally investigate the cylindrical interface thermal contact resistance. First of all, a setup is described. Then a one-piece specimen is inserted for revealing the setup behaviour and for measuring the temperature profile of simulated perfect contact without resistance.

Then the simulated bearing housing is inserted instead of the reference one-piece specimen. The housing has ground inner surface enabling precise fit of inserted rings. Three variously ground bearing rings are then gradually interchanged to investigate the influence of grinding tolerances.

An influence of rotational position of the ring as well as presence of lubricant is eventually investigated.

4.1 Experimental setup

The equipment used for measurement of the temperature profiles in the cylindrical arrangement shall be described in following lines.

The measured object consists of the inserted specimen which is a one-piece ring or two assembled rings representing installed bearing ring in bearing housing. All samples are made of steel 16MnCr5 of which the thermal conductivity has been determined in chapter 3.2 .

Since the setup is common for both the reference measurement and the resistance measurement, it is described separately using the one-piece specimen for the reference measurement. The two-piece specimen is described in the designated chapter 4.3.1 .

The specimen has holes for thermometers drilled in spiral pattern to minimise their effect on the temperature field. The pattern is repeated 4 times around the circumference of the tube to determine the effect of the cylindricality of the ground surfaces. See the simplified diagram in Figure 39 depicting one of the 4 series of holes for thermometers located on the one-piece reference specimen. The reference specimen was used to measure the ideal temperature profile

without any thermal resistance for comparison with two-piece assembly. The schema is accompanied by photography of the actual reference specimen in Figure 40. The technical drawings number DP1731-02-01 provides more details.

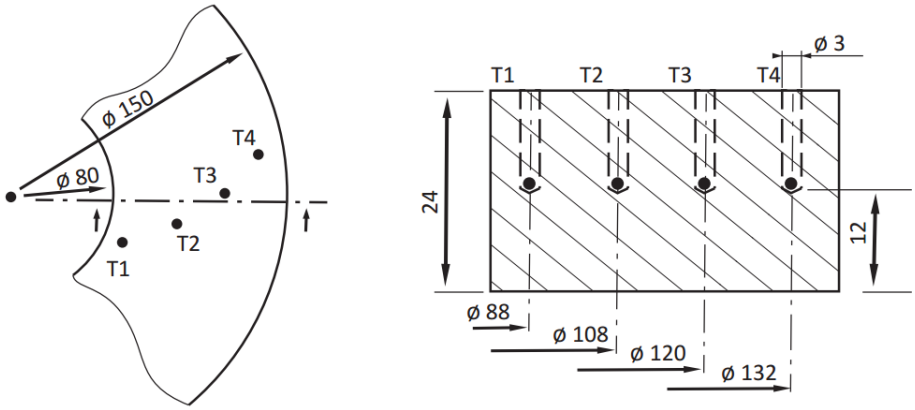

Figure 39: The reference one-piece specimen for measuring the ideal temperature profile, one of four series of thermometers in detail

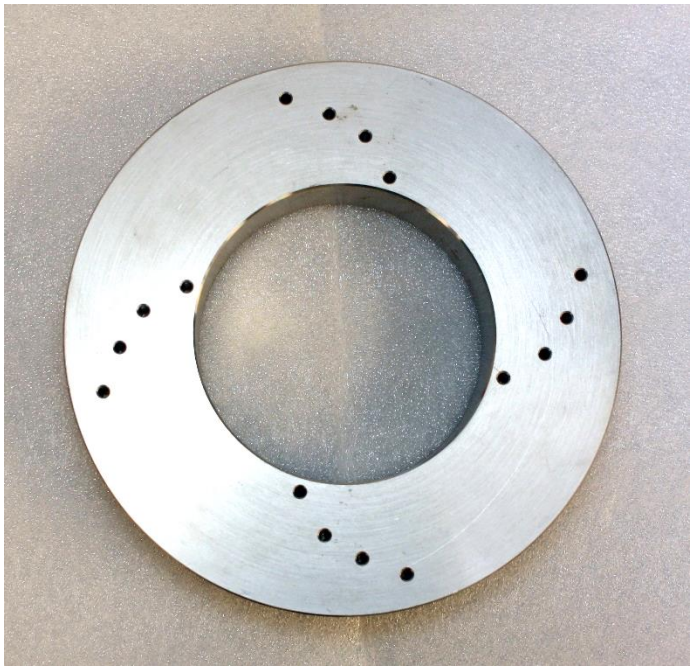

Figure 40: Photography of the one-piece reference specimen

Furthermore, the measuring assembly consists of electric resistance heater placed on the inner diameter and secured maximising the contact. The mating surfaces were spread with thermally conductive paste.

The outer diameter was cooled down by freely circulating water supplied to the device by water cooling circuit presented in the chapter 3.1.1 . To minimise corrosion of the outer diameter, thin layer of lubricant was applied on the surface. Figure 41 depicts the reference specimen inserted in the measuring device with the electric heater on its inner diameter. The cooling water

circulates in the channel between the metal surface and the insulation cover. The coolant inlet and outlet are angled and accompanied with flow restrictor between them to force the coolant to circulate through the channel.

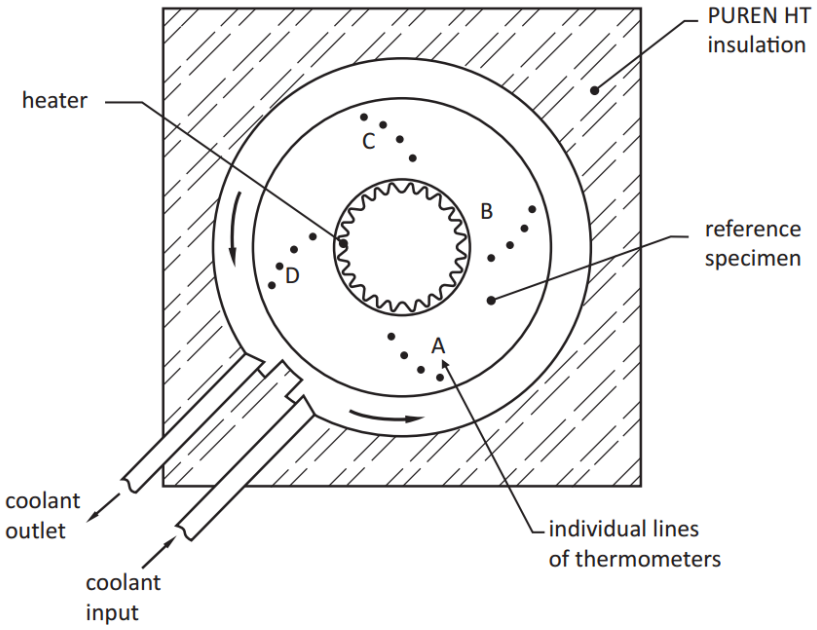

Figure 41: The measuring device with inserted reference specimen, the capital letters denote individual lines of the thermometers

Since the tubular sample is more robust in comparison to the cylinders used in the chapter 3 – its heat transferring area is greater – the heater has to supply higher heat flow leading to higher reached temperatures. Thus another type of insulation was used to withstand those temperatures. The used PUREN E 40 HT insulation – polyurethane foam – is declared stable up to $200\ °C$ which is sufficient. See the enclosed technical list in the appendix F.

An autotransformer with voltage display was used for powering the heater. And since the heater has known resistance (which does not change dramatically with the temperature – as found during measurement with digital DC power supply), no other mean of measurement was necessary for power input determination.

The ambient temperature was measured with nearby thermometer on the same level as the device and another sensor was placed on the surface of the insulation cover. The water temperature was sensed in the water reservoir.

The cooling circuit is unchanged and described in the chapter 3.1.1 . But to cool down higher power inputs without too steep temperature rise of the water in the reservoir, the fans of the radiator were switched on for all measurements on the full scale setup.

4.2 Reference measurement

To obtain the temperature profiles of the perfect connection of the bearing ring and the housing, the one-piece specimen simulating such connection is measured. The reference procedure also examines behaviour of the device and provides data to identify errors and deviations not caused by the ring – housing interface.

4.2.1 Reference measurement – procedure

All the equipment was let to temper and the transient state due to switching on the cooling circuit was let to fade out.

The ambient temperature was $20\ °C$ and protection against direct sunlight was placed over the assembly.

The temperature sampling took place in the steady state which was considered to supervene after $10\ min$ of temperature changes no bigger than $0.5\ °C$. This limit was lowered in comparison to simplified experiment as the time constant of the tubular system was significantly shorter.

Limited number of thermometers was used – all four positions were occupied on the D series, the series A, B and C had thermometers placed at the 1st, 2nd and 4th position (as marked in the Figure 39).

4.2.2 Reference measurement – obtained data

Several measurements were performed with various input power rates. In limited extend the switch on and the switch off transient states were recorded. Sampling period is $2\ s$. Figure 42 shows the typical time development of the temperatures, the plotted data were recorded by the D series of sensors. The lower plot represents the time gradient of sum of all the temperatures for determining the steadiest moment – marked by the green dotted line. The gradient is smoothened over 10 samples to reduce the noise.

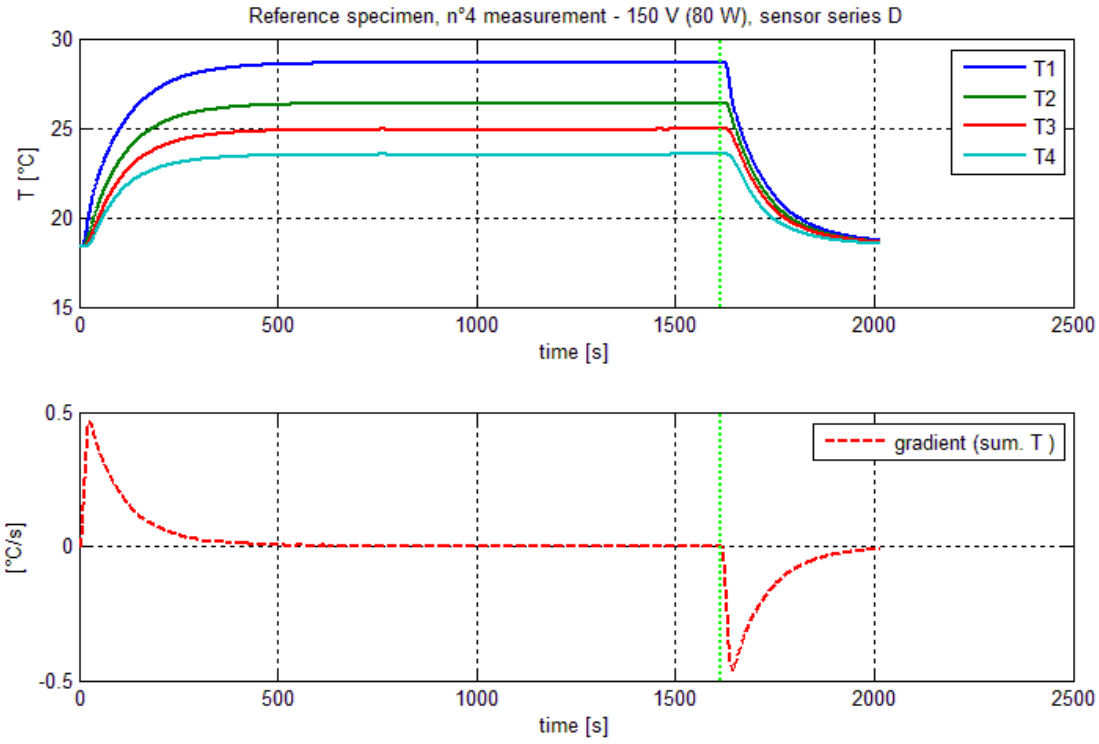

Figure 42: Temperatures vs. time in the reference specimen, lower plot shows the time gradient of sum of all the temperatures, green dotted line marks the sampling moment

Note that the temperature distribution is irregular – respecting the logarithmic distribution given by the equation (2-8) for temperature profile in cylindrical wall. Though the gap between

$T1$ and $T2$ is mainly due to the uneven distribution of the thermometers along the radial axis. The uneven distribution was chosen to enable exchangeable inserts – the rings – described in the chapter 3.1.1 .

Several measurements were completed with input voltage on heater of $250, 251, 120$, $150, 200$ and $140\ V$. The higher power rates at the beginning help to rise the temperature of the cooling water increasing the effectiveness of the water cooling radiator.

Temperature profiles are obtained by plotting the steady state values along the radial axis r. Figure 43 presents the profile gained by measurement shown in Figure 42. Individual lines represent distribution along each series of sensors. Temperature profiles for other power parameters see in appendix B.

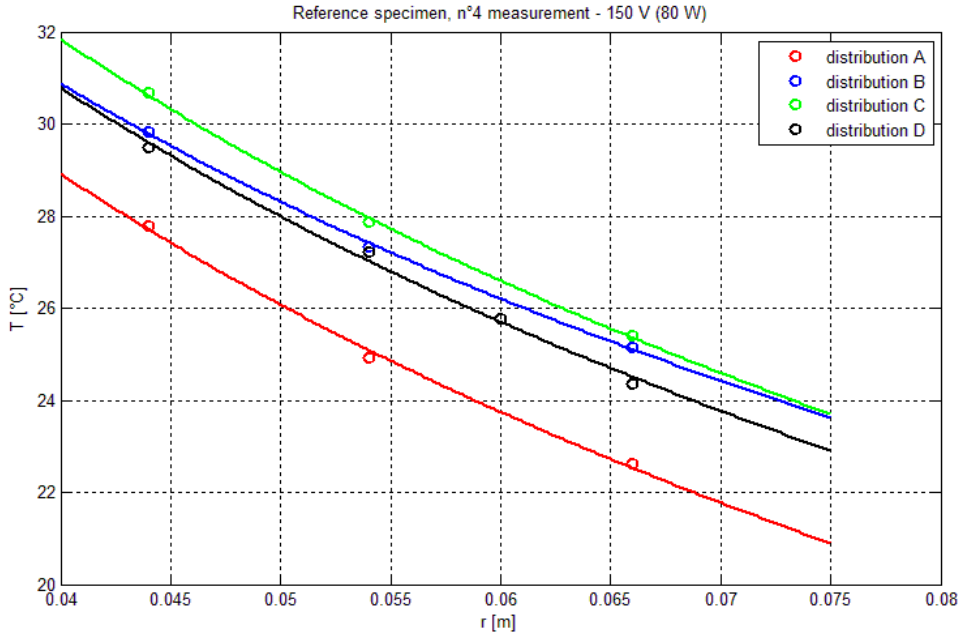

Figure 43: Temperature profile along the radial axis measured by individual series of sensors

Gathered temperatures were fitted by logarithmic curves given by equation (2-8) by the least squares method. Note that even though the lines vary by approximately $3\ °C$, their slope is constant – with the exception of line B. Those differences are due to uneven heat distribution by the heater which may not perfectly contact the inner radius or due to uneven water circulation around the outer circumference. Slight deviations may be due to not exact positions of the thermometers, but this effect was not observed by repeated insertion of the sensors.

By comparing the equation (2-8) for logarithmic temperature profile with the fitted lines, the heat flows along the individual sensor series were identified. Table 13 presents the values of heat flows accompanied with their average values and their deviations from the input power rate. Processing of the data is presented in the following chapter 4.2.3 .

Table 13: Measured heat flows through the reference specimen and comparison to input power rates

	power input		calculated					
N°	$U\ [V]$	$P\ [W]$	$q\ [W]$				$q_{avg}\ [W]$	$dev1_{avg}\ [\%]$
	Position		A	B	C	D	-	-
1	250	219.30	218.29	203.59	218.27	218.00	214.54	-2.17
2	251	221.06	218.16	204.70	218.55	217.83	214.81	-2.83
3	120	50.53	53.51	46.17	51.17	51.04	50.47	-0.10
4	150	78.95	80.93	73.14	82.17	79.52	78.94	-0.01
5	200	140.35	138.99	127.55	145.88	142.63	138.76	-1.13
6	140	68.77	70.14	61.22	72.25	71.76	68.84	0.10
		$dev2_{avg}\ [\%]$	1.28	-8.44	2.13	0.94		

The column of average heat flow q_{avg} represents the mean value of the rates measured by individual sensor series. Its deviation expresses the difference from the input power rate. Note the pattern of smaller deviations for lower power rates. Such effect is due to higher temperature gradient towards the surroundings occurring with the higher rates and consequent higher heat dissipation. Nevertheless, lower relative sensitivity for external factors may be expected for higher power rates.

The bottom line of average deviations represents the average deviation of each individual sensor line. While the sensor series A, C and D have the individual deviations small and random and so their average is relatively small, the B sensor line exhibits constant and significant heat flow drop. The most significant inconsistency - on this otherwise very uniform system - causing such drop may be the heater's ends overlap. As the heater has form of a rectangular foil slightly longer than the inner circumference, its ends overlap each other creating area of imperfect contact.

Now the temperature profiles in specimen without any contact resistance are known and possible errors caused by the measuring device are identified. Replacing the compact specimen by assembly of simulated bearing ring and housing and comparing obtained profiles shall reveal the influence of the thermal contact resistance.

4.2.3 Reference measurement – data processing

In this chapter is provided an explanation of all the data processing.

First, the input power rate $P\ [W]$ is determined using the nominal heater resistance $R_h = 285\ \Omega$ and the power source voltage $U\ [V]$. The value of U was read on display of autotransformer after reaching the steady state. The values of input power rates are presented in "Power input" section of the Table 13.

$$P = \frac{U^2}{R_h} \qquad (4\text{-}1)$$

Determination of the heat flow through the material starts with fitting the measured temperatures with line using the least squares method. Equation (2-8) is utilised to form the line equation (4-3) with linear coefficient a equal to heat flux per axial unit length $\dot{q}_l$. See the following equations for comparison.

$$T = -\frac{\dot{q}_l}{2\pi k} ln \frac{r}{r_1} + T_{w1} \quad (4\text{-}2)$$

$$y(x) = -\frac{a}{2\pi k} ln \frac{x}{r_1} + b \quad (4\text{-}3)$$

The heat flux per axial unit length is then multiplied by the thickness of the specimen $L = 0.024\ m$ and the heat flow passing the line of sensors is obtained.

$$q = \dot{q}_l\, L \quad (4\text{-}4)$$

The deviation of the measured average heat flow from input power rate $dev1_{avg}$ is determined as follows

$$dev1_{avg} = \frac{q_{avg} - P}{P}\ 100\ \% \quad (4\text{-}5)$$

The average deviation of each sensor line $dev2_{avg}$ stands for the average value of all deviations reached during individual measurements. The X stands for individual sensor lines $A \sim B$.

$$dev2_{avg\,X} = \frac{1}{6}\sum_{i=1}^{6} \frac{q_{X\,i} - P_i}{P_i}\ 100\ \% \quad (4\text{-}6)$$

4.3 Measurement of the thermal contact resistance – cylindrical interface

The following chapter describes experimental investigation of the thermal contact resistance of cylindrical interface. The measurements cover influence of several variables. Gradually is identified effect of the heat flow and of the air gap thickness, eventually the relative position of the surfaces and their cleanliness is investigated.

Since the experiment utilises the setup described in chapter 4.1 , only the description of the tested specimens is provided.

4.3.1 The bearing ring and housing specification

To simulate the bearing housing, a flat ring with ground inner diameter is inserted into the device. It has 4 series of thermometers spaced by 90 °. The holes for thermometers are drilled in spiral pattern to minimise their interference with the temperature field. The individual sensor lines are denoted $A \sim D$. See the Figure 44 showing the insulation cover with channel for water cooling and with the inserted assembly of the simulated housing and bearing ring.

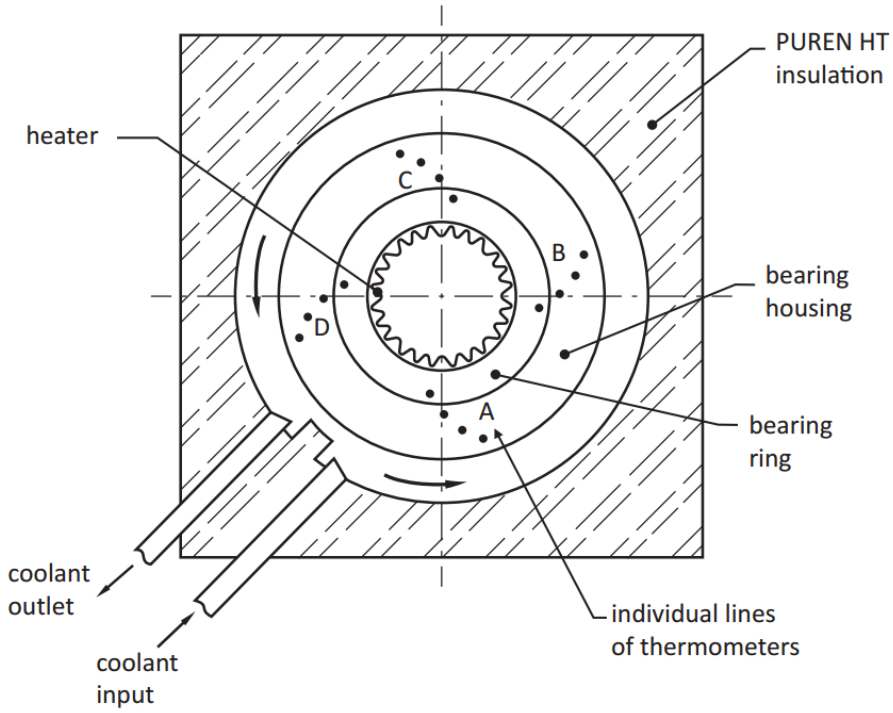

Figure 44: Assembled bearing housing and bearing ring inserted to insulation cover with water cooling and heater

Simplified section of the assembly provides the Figure 45 depicting the real situation with bearing as the source of heat on the left and on the right its substitution with marked positions of the thermometers.

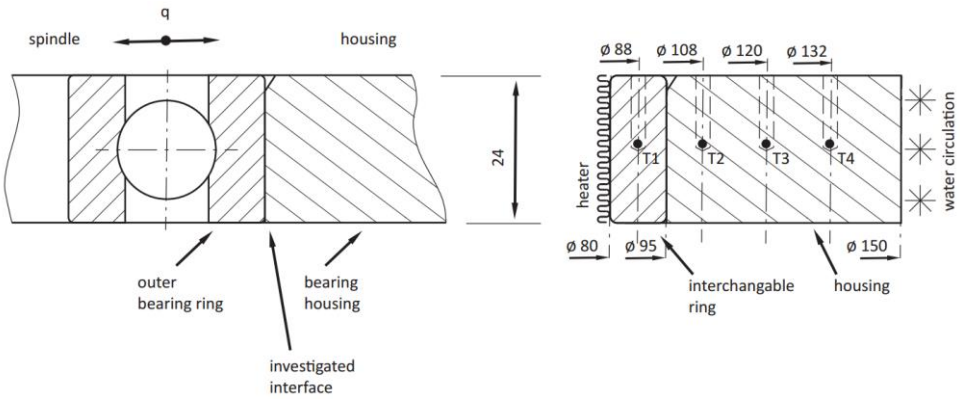

Figure 45: Cross section of the simulated bearing ring and housing on the right ant its comparison to real situation on the left

The following Figure 46 shows photography of the assembly. The bearing ring is not fully pressed in for illustrative purposes.

For details, the technical documentation is enclosed. See the drawing number DP1731-02-02 of the housing and the drawing number DP1731-02-03 of the rings.

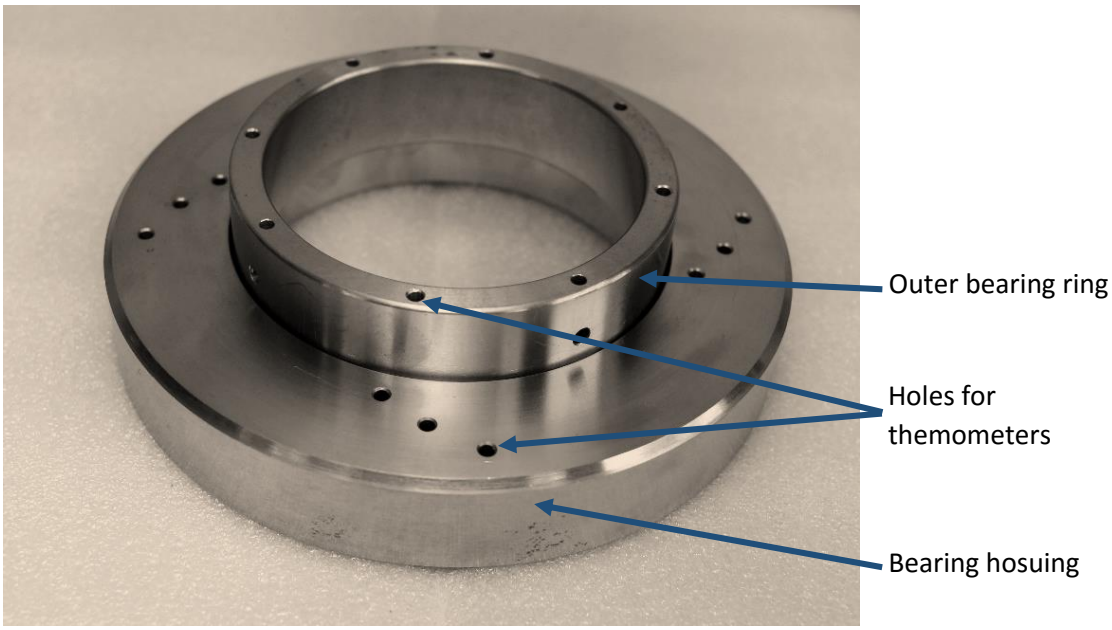

Figure 46: Photography of the semi assembled simulated bearing ring and its housing

To investigate the influence of the initial backslash between the ring and the housing, three different rings were made with their outer circumference ground to different dimensions. The measured values provided by manufacturer and their average is listed in the Table 14.

Table 14: Measured outer diameters of the rings and their average value

ring number	measurement		d
	1	2	$[mm]$
1	94.995	94.998	94.9965
2	94.997	94.998	94.9975
3	94.997	94.999	94.998

The housing dimension measurements and their average value is in the following Table 15

Table 15: Measured inner diameter of the housing and its average value

measurement - housing				$d\ [mm]$
95.002	95.004	95.003	95.006	95.00375

All the rings and the housing were made of 16MnCr5 steel. Its properties are presented in Table 5 and its thermal conductivity was measured in chapter 3.2 .

4.3.2 Experimental investigation – procedure

The surfaces of the ring and the housing were cleaned with technical alcohol and pressed together. Assembled, the setup was let to temper and transient state connected to switching on the water cooling system – including its fans – was let to fade out. The ambient temperature was $20\ °C$.

When the system reaches the steady state, considered to prevail after $10\ min$ without changes greater than $0.5\ °C$, the temperatures were sampled. Thermometers were placed in positions $1, 2$ and 4 in lines $A{\sim}C$, the line D was occupied fully.

After finishing the measurement for each input voltage, the inserted bearing ring was exchanged with the next one and all the series was repeated. Each ring was tested with input voltage of

$$100, 125, 150, 175, 200, 225, 250, 275\ V$$

The Table 16 of results contains the corresponding power rates.

Eventually, the bearing ring 1 was measured rotated by $180\ °$ and the ring 3 was used to investigate influence of a lubricant present in the interface.

4.3.3 Experimental investigation – obtained data

For measurement of the thermal contact resistance of the cylindrical interface only the steady state method of data processing was chosen. Therefore, most of the measurements do not cover the full cycle of the transient state – steady state – transient state. Due to time limitations, only minor part of the steady state was recorder. To minimise the noise influence, records of length over $1\ min$ were created with sampling period of $2\ s$.

Representative record of part of the steady state is plotted in Figure 47. The thermometers are numbered from $T1{\sim}T4$ increasingly with their radial distance from the heater.

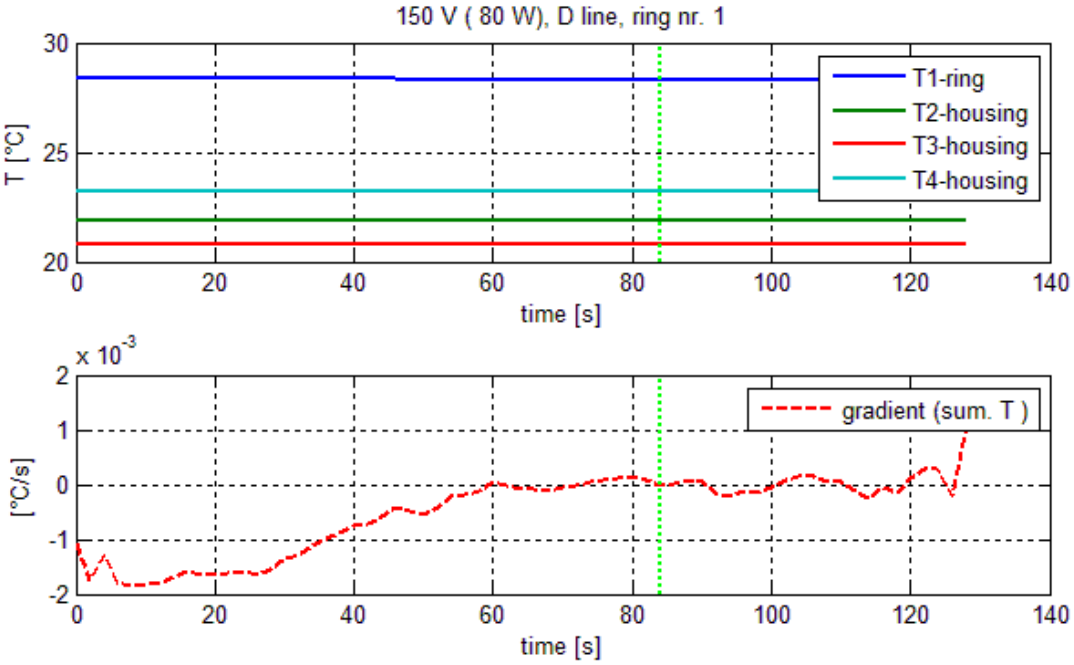

Figure 47: Temperature vs. time in the ring and housing assembly along the D series of sensors, ring no. 1 inserted, lower plot marks the gradient of the sum of the temperatures, the green dotted line marks the sampling moment

Note the major difference of the temperature distribution in comparison to the Figure 42. Especially the temperature jump from $T1$ to $T2$. The two figures plot the data obtained under identical conditions – the difference is only due to the imperfect contact between the ring and its housing. The data for further evaluation are sampled at the time marked by green dotted line.

To obtain the temperature profile in the assembly, the values from each line of sensors are plotted against the radial coordinate.

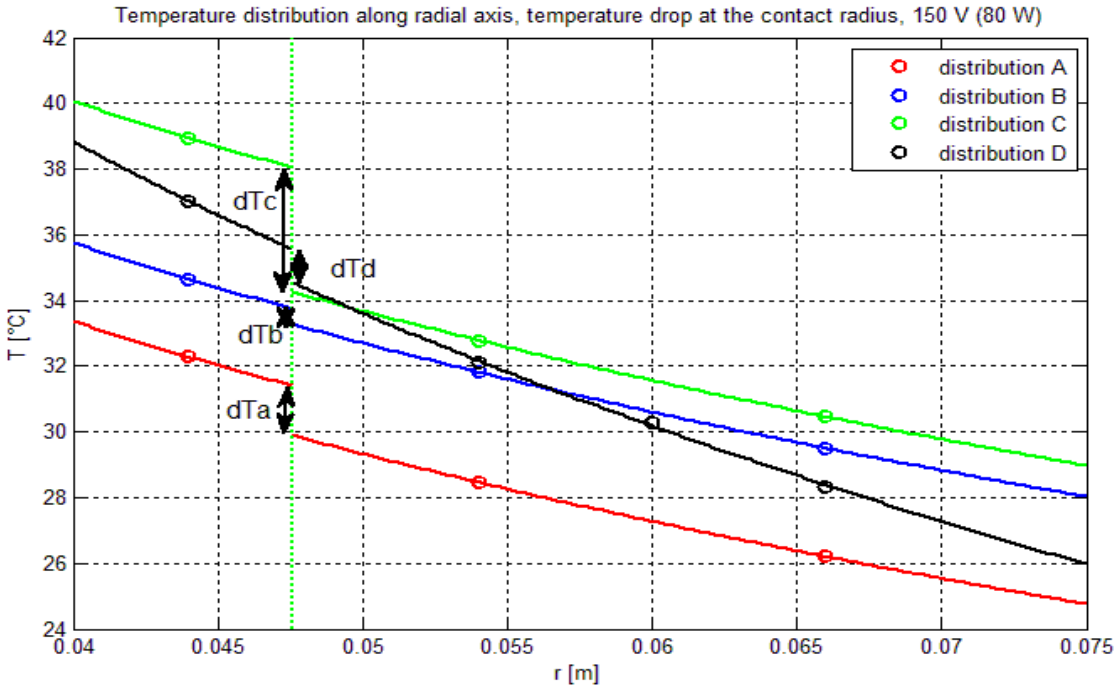

Figure 48: Temperature vs. radial coordinate, input 150 V (80 W), ring no. 1, the green dotted line marks the contact location

The Figure 48 shows the typical distribution of the temperatures along the individual lines of sensors. The profiles obtained from other performed measurements are presented in appendix C, D and E. Data are fitted with logarithmic curve accordingly to the eq. (4-3) and the corresponding heat flux per unit length $\dot{q}_l$ through the adjacent part of the ring is calculated using the slope of this line, eq. (4-4).

Note the difference from Figure 43 plotting the distribution in solid material. Though the heat flow is identical, reached temperatures of the inner surface of the assembly are by $2{\sim}11\,°C$ higher and the spread of the profiles is wider by factor of 2.

The lines are extrapolated towards the interface and the temperature drop ΔT, in the figure marked dTx, is determined.

While the lines $A{\sim}C$ show somewhat identical slope, the line D deviates remarkably. An investigation of possible source of this phenomena was carried out.

The D line proved to be consistent across several exchanges of the sensors as well as repeated insertions of the ring and heater. Thus the prevailing source of the deviation is in the contact. Since the deviation occurred in the measurements with all individual rings inserted, the surface deformation of the inner diameter of the housing is presumably the cause.

Potentially, local elevation of the inner surface of the housing located close to the $T1$ thermometer would cause temperature decline of the adjacent area of the ring. Furthermore, such elevation would increase the temperature in the inner part of the housing while having negligible influence on the outer part. Thus such deviation of the inner diameter of the housing wold be sufficient explanation.

The results are presented in Table 16. For each ring is stated the input power rate. Then is determined the ΔT and the heat flux per unit length $\dot{q}_l$. The thermal contact resistance is calculated accordingly to the eq. (2-6). The bearing rings are denoted as sated in the Table 14 – from 1 to 3 increasingly with their measured diameter.

Table 16: Results of measurement of the thermal contact resistance of cylindrical interface

N°	Power input		Ring 1							
	U [V]	P_{in}[W]	ΔT [K]				R_c [Km^2/W]			
Position			A	B	C	D	A	B	C	D
1	100	35.1	0.890549	0.304332	2.413552	0.790555	0.000156	5.28E-05	0.000456	8.4E-05
2	125	54.8	1.220619	0.357876	3.191871	0.980445	0.000141	4.14E-05	0.00037	6.82E-05
3	150	78.9	1.500271	0.466508	3.778732	1.009812	0.000123	3.76E-05	0.000299	4.92E-05
4	175	107.5	1.790289	0.552149	4.21228	0.646641	0.000109	3.27E-05	0.000243	2.36E-05
5	201	141.8	2.018515	0.611948	4.61294	0.141369	9.29E-05	2.77E-05	0.000198	3.86E-06
6	225	177.6	2.156761	0.643873	4.712023	-0.48322	7.99E-05	2.33E-05	0.000161	-1.1E-05
7	250	219.3	2.261561	0.664776	4.567276	-1.31239	6.83E-05	1.99E-05	0.000124	-2.3E-05

N°	Power input		Ring 2							
	U [V]	P_{in}[W]	ΔT [K]				R_c [Km^2/W]			
Position			A	B	C	D	A	B	C	D
8	100	35.1	1.024454	0.637908	1.427779	0.225301	0.000188	0.000109	0.000257	2.4E-05
9	125	54.8	1.341415	0.920182	1.980276	0.281445	0.000165	0.000102	0.000225	1.96E-05
10	150	78.9	1.576021	1.203597	2.578921	0.306077	0.000136	9.2E-05	0.0002	1.5E-05
11	175	107.5	1.685634	1.421069	3.123082	0.282392	0.000109	8.12E-05	0.000178	1.05E-05
12	200	140.4	1.713533	1.619666	3.634639	0.195307	8.43E-05	7.07E-05	0.000157	5.54E-06
13	226	179.2	1.68977	1.819503	4.041801	0.069717	6.5E-05	6.29E-05	0.000137	1.56E-06
14	249	217.5	1.598338	1.976257	4.300578	-0.05927	5.06E-05	5.59E-05	0.000119	-1E-06
15	276	267.3	1.615143	2.153974	4.466474	-0.20374	4.22E-05	5.07E-05	0.000102	-3.4E-06

N°	Power input		Ring 3							
	U [V]	P_{in}[W]	ΔT [K]				R_c [Km^2/W]			
Position			A	B	C	D	A	B	C	D
16	100	35.1	0.548607	0.836609	1.114652	0.205614	9.85E-05	0.000152	0.000203	2.2E-05
17	125	54.8	0.700783	1.026445	1.441295	0.208374	8.44E-05	0.000117	0.000163	1.45E-05
18	150	78.9	0.832498	1.196894	1.728878	0.173439	7.12E-05	9.53E-05	0.000132	8.47E-06
19	175	107.5	0.920203	1.255828	1.983711	0.108875	5.92E-05	7.26E-05	0.00011	3.93E-06
20	200	140.4	1.080028	1.423466	2.304086	0.059707	5.4E-05	6.33E-05	9.71E-05	1.68E-06
21	225	177.6	1.246302	1.57857	2.648272	-0.01142	5.03E-05	5.59E-05	8.87E-05	-2.6E-07
22	250	219.3	1.369952	1.708198	2.99404	-0.12477	4.49E-05	4.89E-05	8.1E-05	-2.3E-06
23	275	265.4	1.44573	1.849124	3.321042	-0.27635	3.94E-05	4.41E-05	7.49E-05	-4.3E-06

Note that in contrast to the data obtained from the planar experiment - Table 7, the thermal contact resistance of the cylindrical contact is substantially dependent on the input power rate. This dependence will be further examined. Generally, the values of the resistance decline with rising heat flow.

The anomalous D line stands very small values for both the temperature drop and the thermal contact resistance. While the temperatures were actually measured, it is not possible to conclude ΔT or R_c could reach negative values. It is its very local effect of tightly mating surfaces that make such appearance from macroscopic point of view. To investigate this phenomenon more comprehensively, a 3 dimensional analysis of adjacent area needs to be performed.

Nevertheless, keeping in mind the impossibility of such values, the data can be used for statistical processing to obtain macroscopically more accurate results.

4.3.4 Interpretation of the results

First of all, let us now investigate the dependence of the calculated values on the directly measurable input power rate. Furthermore, the input power rate is equivalent to power loss in the spindle bearings and so the obtained plot might be directly used for estimation of the actual thermal contact resistance in the spindle bearings. But so far, the data are valid only for the cases identical with the measured assembly, including the nominal diameters, the clearances and the roughness as well as the interval of the heat flow and condition of clean surfaces.

The Figure 49 shows the dependency of the thermal contact resistance of individual rings on the input power rate. For each ring are plotted resistances measured by all 4 lines.

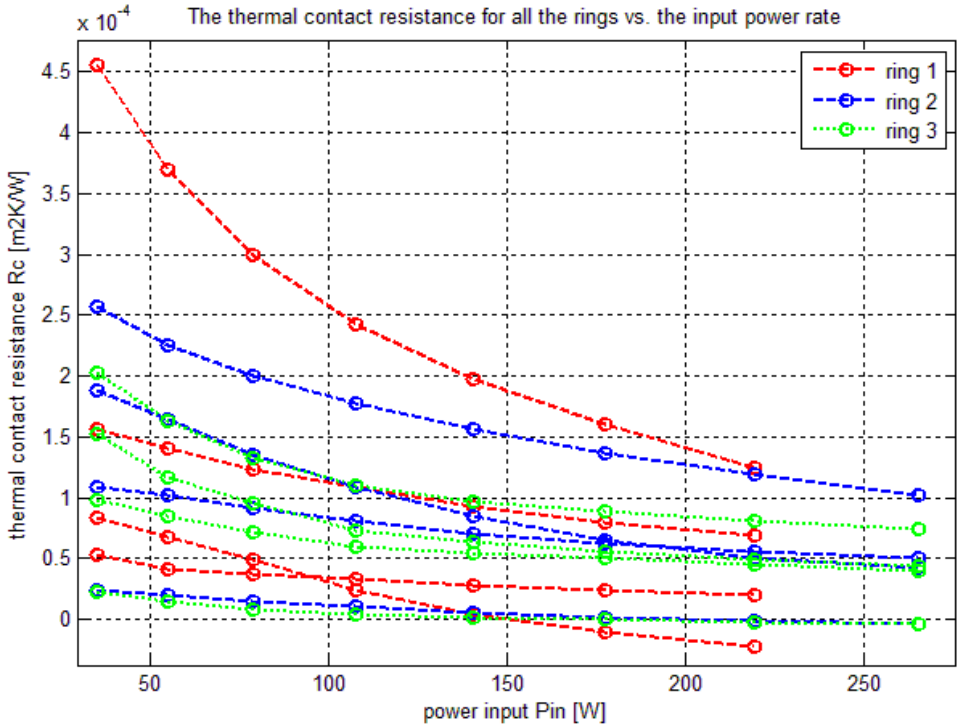

Figure 49: Thermal contact resistance vs. power input rate, comparison of all the rings

Note that the distribution of the resistances is concentrated lower for the rings of bigger diameter. Though the interval covered by each ring is wide enough to conclude that the cylindricality of the mating surfaces prevailingly determines the local contact resistance. While the actual air gap or interface pressure influence the resistance more from the macroscopic point of view as shown on the Figure 50.

Let us now fit the above presented lines with the first order polynomials and plot their average values in the Figure 50.

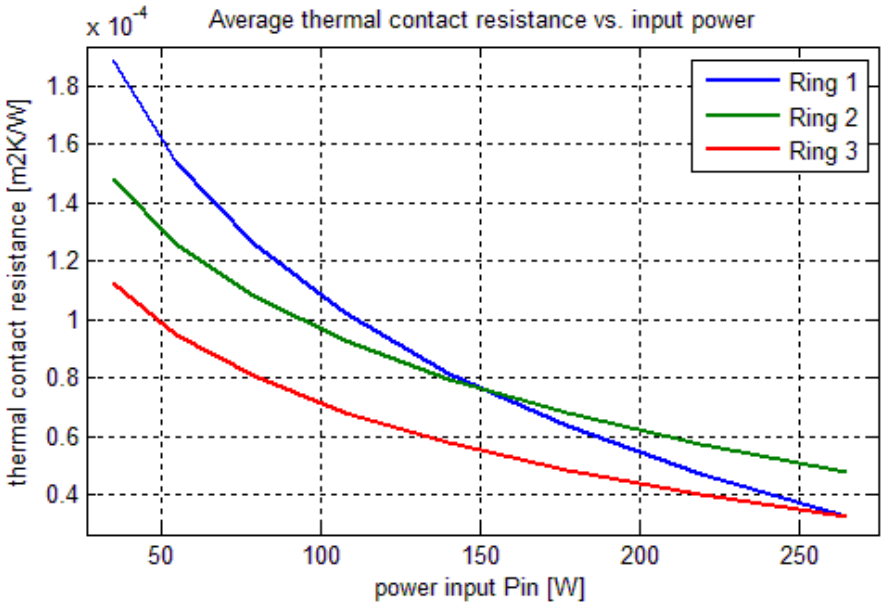

Figure 50: Average values of the thermal contact resistance of each ring as function of the input power rate

Note that the thermal contact resistance lines are initially sorted accordingly to the measured diameters of the individual rings – see the Table 14. Such distribution confirms that the actual thickness of the theoretical air gap determines the resulting resistance for low power rates and consequently for low temperature changes. Moreover, the resistance of each ring is intensely dependent on the input power rate.

A comparison of individual measured temperature profiles (see the Figure 48 for representative, the appendix C, D, and E for other measured profiles) shows relation of the reached temperatures on the input power rates. With higher power rate, higher temperatures of the inserted ring are reached, accompanied with steeper temperature decline towards the heat sink.

Let us now determine the thickness of the air gap as function of the average values of temperatures for each input power rate. See the chapter 4.3.7 for step by step data processing.

The found value is only hypothetical and stands for the air gap between the ideal cylindrical surfaces. While the real specimens have limited physical contact and variable air gap, a statistical approach is used for generally usable results. The Figure 51 shows the dependence of airgap thickness on the input power rate.

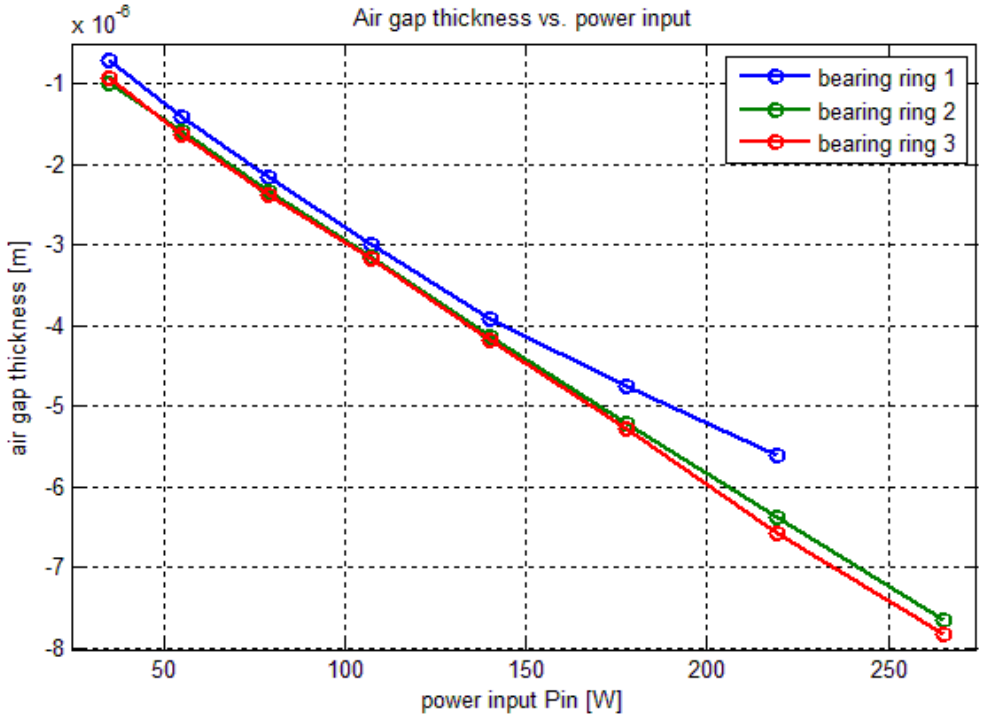

Figure 51: Estimated airgap thickness vs. input power rate

The above plotted values are for the ideal cylindrical surfaces and do not reflect the physical aspect, thus the negative values. Real ring with increasing power rate firstly adapts its imperfect shape to more rigid housing while decreasing the air gap. Presumably, at power rate of about $20\ W$ the rings would fit to the housing without significant gaps. Further increasing of the energy rate would lead to deformation of both the ring and housing and creation of pressure field.

Observe that the thermally inducted deformation has prevailing influence in comparison to influence of the initial air gap. The rings are stepped by 1 and $0.5\ \mu m$ (if taken as perfectly cylindrical and of diameter equalling to the average of the measured ones, see the Table 14). This initial difference disappears quickly since the ring with grater air gap (~greater R_c) heats up rapidly and expands even for relatively low heat flows.

To estimate the interface pressure, the actual dimensions of the used ring and its seating must be measured. To demonstrate what the initial thickness of the air gap is possible, tolerances for machine-tool spindle bearing and its seating recommended by manufacturer are presented in the Table 17. Observe that the recommended values are for diameter measure, while the hypothetical interference overlap / airgap plotted in Figure 51 is assumed evenly distributed and are referring to radius measure.

Table 17: Recommended seat tolerances and ring production tolerances given by manufacturer, [26]

size	mm	80 - 120 mm	
ring - outer diameter	μm	0	-5
seat - inner diameter - fixed		5	-5
seat - inner diameter - floating		13	3

The Figure 52 shows the dependence of the interface pressure on the input power rate. The figure presumes that the housing is rigid in comparison to the relatively slim ring and so all the deformation takes the ring. The figure interprets the theoretical values of the negative air gap and presents the contact pressures corresponding to equal deformations.

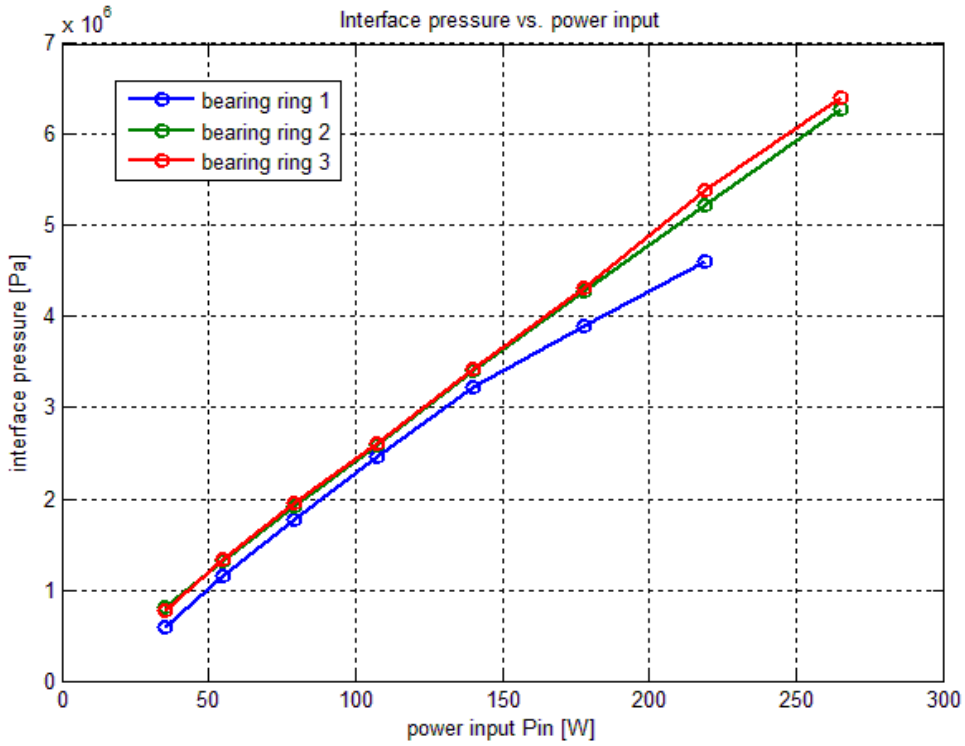

Figure 52: Interface pressure as a function of the heat flow through the specimen.

The theoretical air gap in the Figure 51 or the corresponding contact pressure in the Figure 52 of the ring 1 suggest that its average temperature did not rise as linearly as the temperatures of the other rings. Some surface unevenness creating firstly thick air gap and with increasing deformation loosing influence may cause such behaviour. The steep decrease of the thermal contact resistance of the ring 1 shown in the Figure 50 ratifies similar conclusion. With decline of the resistance, the temperature difference drops and thus resulting interface pressure is lower.

So far all the values are usable only for the presented setup. To extend the validity of obtained data, the Figure 53 shows dependency of the thermal contact resistance on the contact pressure. While the power rate measure cannot be generalised as its influence would vary for individual spindle setups, the contact pressure can be determined from estimated temperatures (i.e. by thermographic camera) and measured diameters of the bearing ring and its housing.

More over, the Figure 53 presents a comparison with the combined Yovanovich's model of solid spot and gap conductance – see chapters 2.4.4 –Yovanovich, 1981, and 2.4.6 – Gap conductance by Yovanovich, 2005, . The model was chosen as it is one of the newest presented and for its relative straightforwardness. The input data are easy to mesure or acquire by approximate

relations. Other combinated models for gap and solid spot reisstance do not fit significantly better.

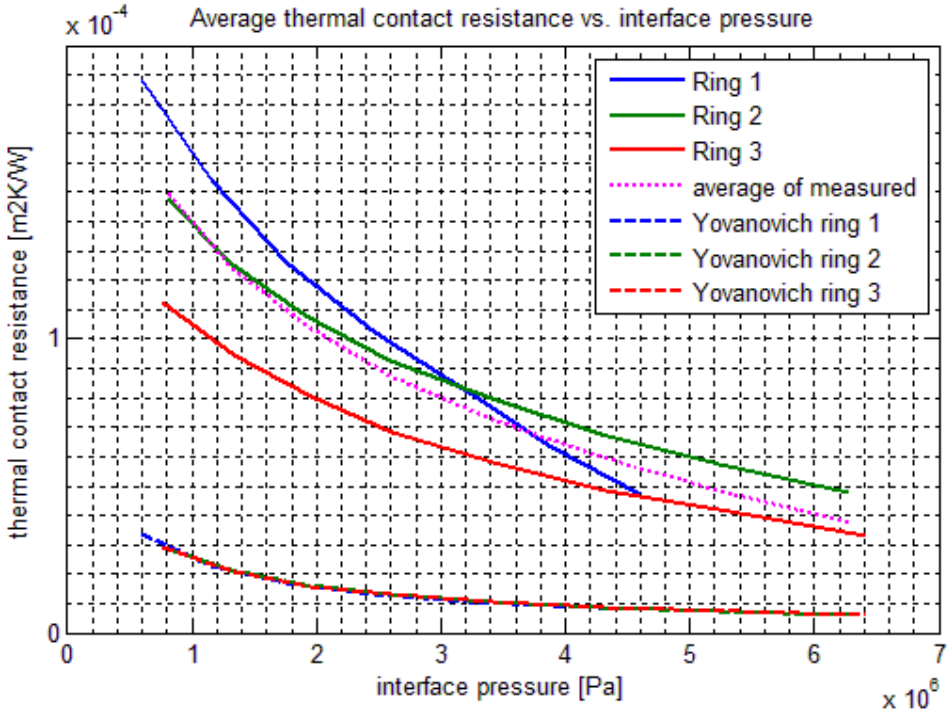

Figure 53: The thermal contact resistance as a function of the interface pressure, the overlapping dashed lines presents combined gap and spot resistance estimated by Yovanovich's model for each ring, dotted line represents the average of measured data

Observe that the lines of Yovanovich's model for each ring perfectly overlay. The most influential parameters of the model are the mean surface plane separation δ (defined by surface roughness – constant for all rings) and interface pressure p, thus the model data as a function of pressure would plot identical lines for all the rings, even though the initial air gap was different.

On the other hand, the measured data shows higher overall resistance and steeper decline. While the model assumes a perfect cylindrical surfaces, uniform pressure and no actual air gap, the specimens mate in limited number of spots due to their ovality. And actual air gap is located between those mating areas. With increasing pressure, the mating area non-linearly grows and leads to lower resistance due to higher contact pressure as well as due to greater area of physical contact – conducting steep decline of measured resistance.

Since the measured data are plotted against the interface pressure, the initial air gap has no influence and so the variances are due to the different cylindricality of the individual rings. Thus the average value can be presented, see the dotted line in Figure 53.

Comparing the average values to the Yovanovich's combined model, the ratio $e = \frac{R_{c\,measured}}{R_{c\,Yovanovich}}$ is obtained and plotted in Figure 54.

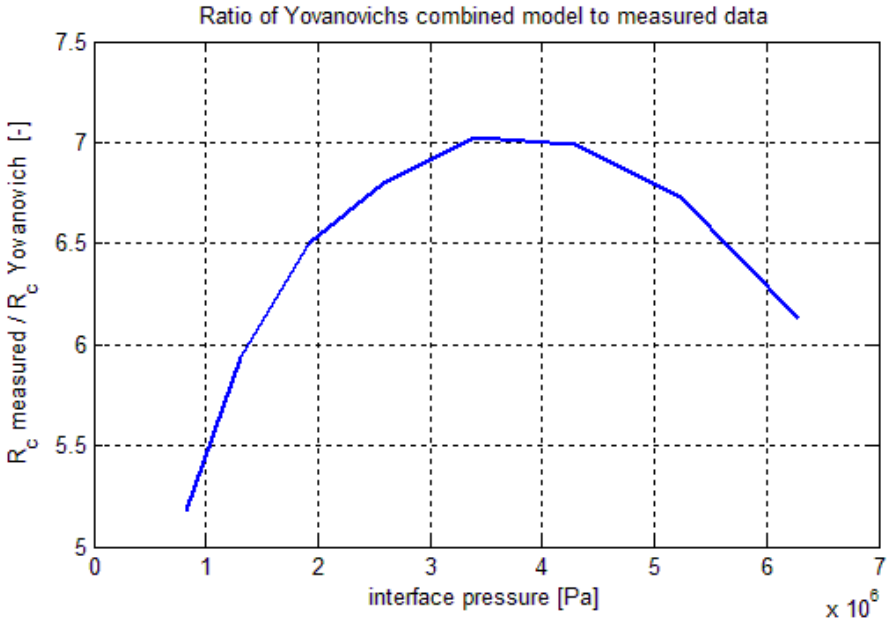

Figure 54: Ratio of the average of measured data to Yovanovich's combined model as a function of estimated interface pressure

Observe that not only the measured data states higher values of the thermal contact resistance in comparison to the Yovanovich's combined model, but also the shape of the dependency is altered. As mentioned, the area of physical contact of the mating surfaces increases nonlinearly with increasing temperature drop as the bearing ring deforms and adapts to the more rigid housing.

The absolute difference of the values can be interpreted as result of present air gaps, which presumably disappear at pressures high above the tested range.

4.3.5 Investigation of other factors

Let us now investigate the influence of other factors. In the first part of this chapter, a ring is measured in two different positions and the resulting thermal contact resistance is compared. The second part considers influence of presence of lubricant in the interface.

Rotational position

The ring 1 was measured in original position and the results are presented in the chapter 4.3.3 , then the ring was rotated by $180°$ and the measurement was repeated. The measuring scale was restricted to fewer number of input power rates corresponding to heater voltage input of

$$150, 200, 260 \ V$$

The Figure 55 shows a comparison of measured thermal contact resistance along each series of sensors for original and rotated position. See the Figure 44 for the sensors' positions.

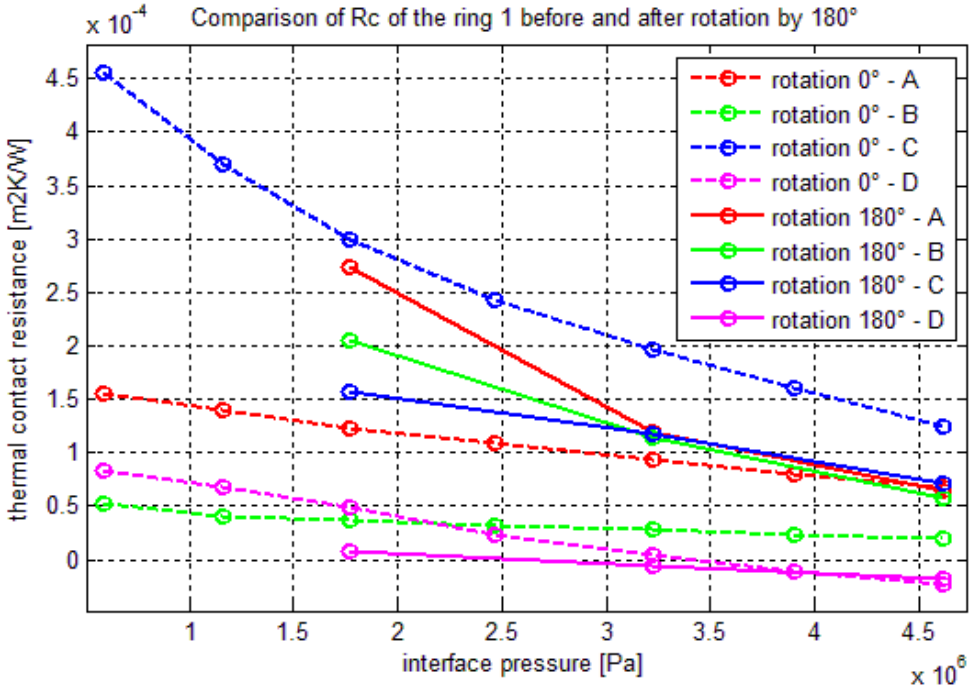

Figure 55: Rc as function of interface pressure, dashed line represents the original position, the solid line marks the Rc of ring rotated by 180°

Observe that the acquired values are in the same range and so the resulting overall cotnact resistance would not change significantly. To determine the prevailing direction of the heat flow, thorough elaboration of shape of surfaces must be performed.

Investigating the pattern of changes from the obtained data, one can assume that significant surface elevation is located on the housing's inner surface near the D line of sensors. Note that for both orientation of the ring, the resistance measured by D sensors is extremely low – see the chapter 4.3.3 for possible explanation of the negative values.

While the resistances measured by A and C line of sensors exchanged without significant change in range. Thus possible areas of lower surface are located on the outer diameter of the ring at the corresponding positions close to A and C sensor lines.

Presence of lubricant

Since the surfaces are slightly lubricated to ease the assembly of spindle units, investigation of such intervention was performed. The volume of applied lubricant varies widely and so its effect. To evaluate the possible range of thermal contact resistance, the experimental setup was tested with the surfaces cleaned by technical alcohol – see the results in the chapter 4.3.3 – and with the interface fully saturated with a lubricant.

The ring no. 3 was firstly measured clean and then was lubricated by bearing oil PARAMO OL-J32. The thermal conductivity of oil was estimated to

$$k_{oil} = 0.14\ W/mK$$

A series of measurements was taken with heater voltage input from $100\ V$ to $225\ V$ by $25\ V$ increments.

Since the lubricants may create layer of substantial thickness resulting in unknown interface pressure, the values are plotted against the input power rates. Thus the Figure 56 is presented only as comparison of non-lubricated and lubricated contact.

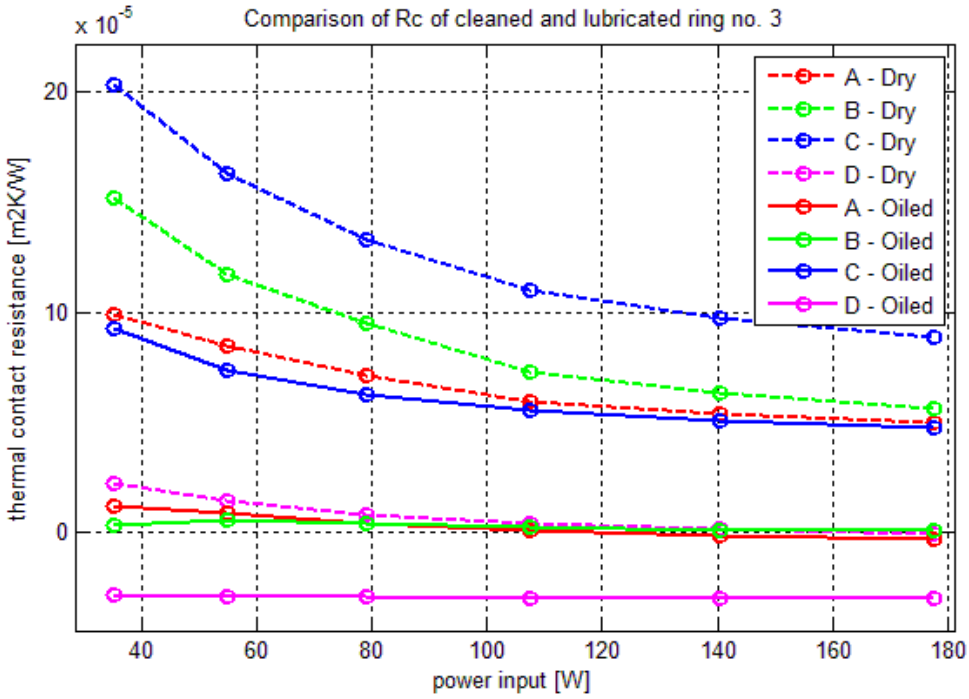

Figure 56: Study of influence of presence of lubricant, dashed lines present thermal contact resistance of dry surfaces measured along individual series of sensors (marked by capital letters), solid lines stand for resistance values of interface saturated with oil

Note that resistances across all sensor lines dropped significantly. The unevenness located close to D line leading to negative values is even more pronounced for the lubricated interface.

Let us now fit the values of the thermal contact resistance with the first order polynomials and find their average. The comparison of the average resistances of individual rings to resistance of the lubricated ring no.3 in shown in the Figure 57.

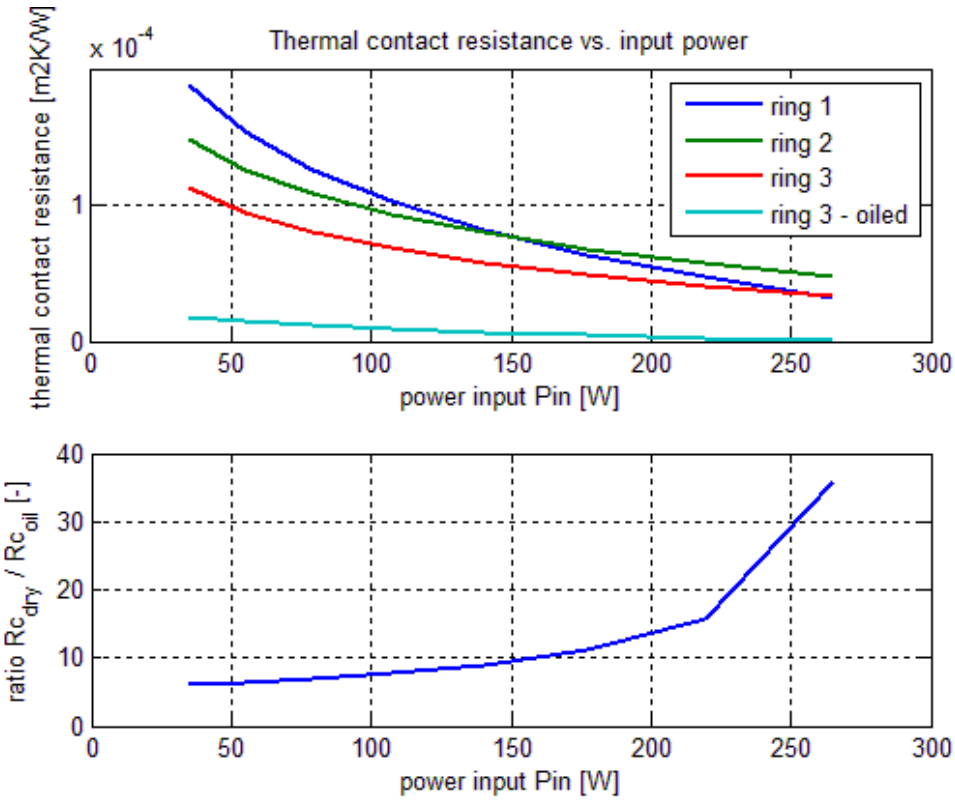

Figure 57: Comparison of average thermal contact resistance of each ring to lubricated ring no. 3, lower figure shows ratio of resistance of the dry ring no. 3 to resistance of the same ring lubricated

Clearly, the overall resistance has dropped. Moreover, on the left part of the plot, the line corresponding to the oiled ring is approximately 6 times lower than the line related to the same, but clean ring. This correlates with higher lubricant thermal conductivity which is approximately 5.1 times higher than the one of the air.

With higher temperatures the ability of oil to transit heat increases and thus the thermal contact resistance drops steeply. Observe that the interface was fully saturated by lubricant prior to measurement. Presumably only a thin film of lubricant would be applied to ease the installation in manufacturing process. Specific effect of such condition needs to be further investigated, but the range is established.

Generally, the comparison shows significant influence of lubricant. Therefore, to precisely evaluate the resistance of any application, particular attention must be paid to type and volume of used oil.

4.3.6 Overall effect of thermal contact resistance

Since the value of thermal contact resistance in range of used condition was acquired in the chapter 4.3.3 , let us now investigate its influence. Comparison of temperature profile in the one-piece reference specimen and in the assembly consisting of ring and housing is given in this chapter.

Analogous tests were performed for both variants with heater input voltage of $150, 200$ and $250\ V$.

Since the influence can increase unlimitedly with rise of the gap, it is more practical to evaluate the minimal influence of the contact. Thus, the assembly with inserted ring no. 3 is chosen to be compared to the reference specimen. The Figure 58 plots the temperature profiles in the reference specimen accompanied with corresponding profiles in the assembly. The plotted lines are the average of the temperatures obtained along individual sensor lines. The absolute members of plotted polynomials were zeroed to obtain constant outer temperature (except the abs. members of the bearing ring lines, which stand for the temperature drop).

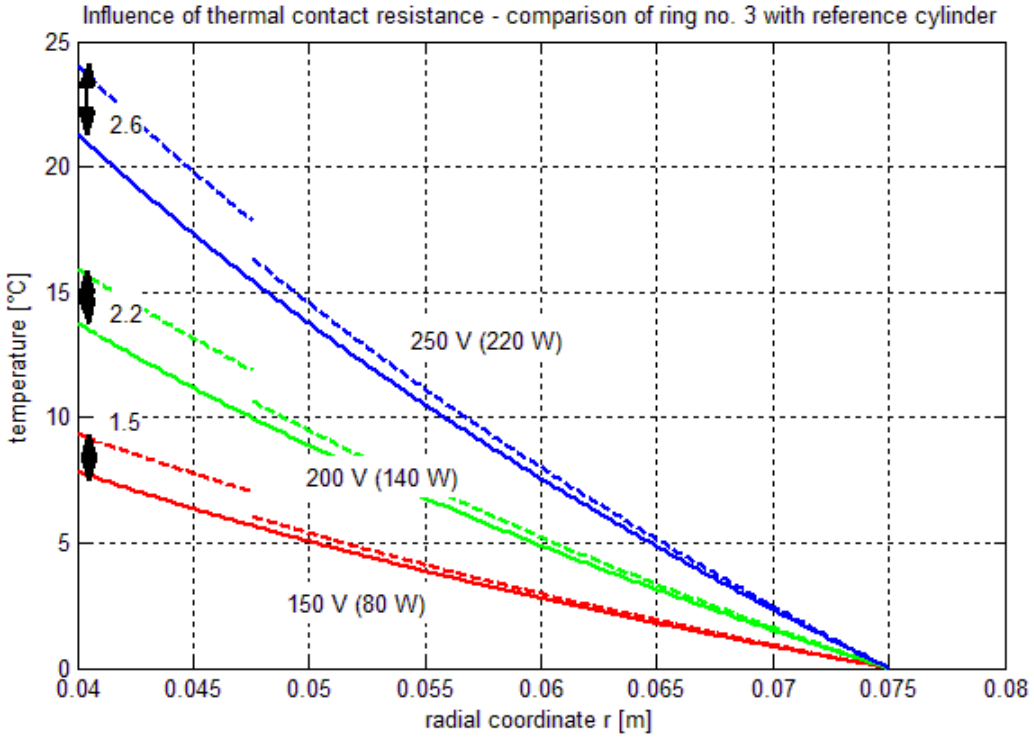

Figure 58: Comparison of the temperature profiles in the reference cylinder (solid lines) to the profiles in the assembly with ring no. 3, absolute members are zeroed to obtain constant outer temperature

Note that even though the thermal contact resistance declines with increasing power input, the resulting temperature difference from reference specimen increases. Marked values stand for the temperature rise on the inner surface of the outer bearing ring due to the thermal contact resistance. The values are the minimal ones as the ring no. 3 has maximal outer diameter from tested specimens (see the Table 14) and consequently has the least thermal resistance.

4.3.7 Experimental investigation – data processing

This chapter clarifies the calculations made to obtain data presented in the chapters 4.3.3 and 4.3.4 .

To acquire the thermal contact resistance, the local heat flow along each sensor line must be identified – the calculation does not assume constant heat flow around the circumference of the assembly. Hence to obtain the local heat flow, first order polynomial was fit to each row of measured temperatures. Similarly, as in the chapter 4.2.3 , the points were fitted by following equation of a curve using the least square method.

$$y(x) = -\frac{a}{2\pi k} ln \frac{x}{r_{inner}} + b \quad (4\text{-}7)$$

Where coefficient a stands directly to the local heat flux per unit length $\dot{q}_l$ and r_{inner} for inner diameter of corresponding specimen.

Evaluating the equations (4-7) for the interface coordinate for both the ring and the housing leads to temperatures of the surfaces in contact. Their subtraction yields the temperature drop presented in the Table 16.

$$\Delta T = y_{ring}(r_{contact}) - y_{housing}(r_{contact}) \quad (4\text{-}8)$$

In the right section of the table, there are presented the values of thermal contact resistance acquired as fraction of ΔT and heat flux $\dot{q}$ as stands the eq. (2-6).

$$R_c = \frac{\Delta T}{\dot{q}_{red}} \quad (4\text{-}9)$$

The $\dot{q}_{red}$ stands for the heat flux calculated with reduced area of actual contact A_{red}. The reduced values are used since the chamfered edges of the ring and housing reduce the area as shown in the Figure 59.

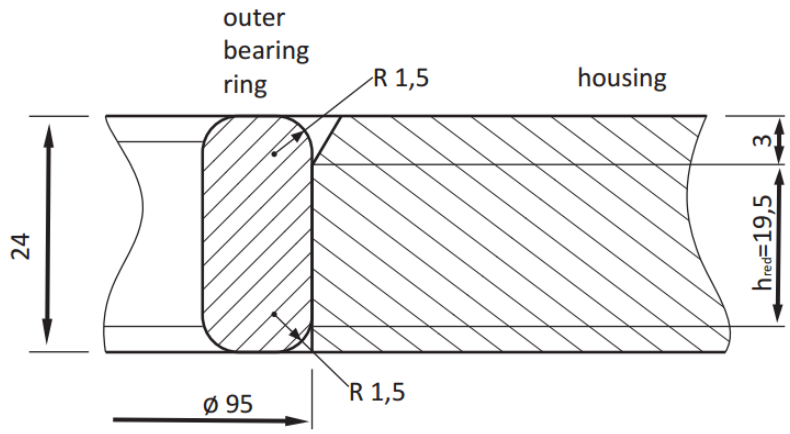

Figure 59: Reduction of the contact area by chamfered and rounded edge of housing and ring respectively

Respecting the decrease of the reduced contact height h_{red} in comparison to height at which the heat flux per unit length $\dot{q}_l$ was measured, the $\dot{q}_{red}$ stands

$$\dot{q}_{red} = \frac{\dot{q}_l \, h_{full}}{A_{red}} = \frac{\dot{q}_l \, h_{full}}{2 \, \pi \, r_{contact} \, h_{red}} \quad (4\text{-}10)$$

where the h_{full} stands for the total height of the ring and housing, the h_{red} to reduced height due to rounded and chamfered edges A_{red} for resulting reduced area of contact on radial coordinate $r_{contact}$.

The Figure 51 was plotted to specify the air gap thickness between the ideally cylindrical rings and the housing.

The values of the air gap thickness $\delta\ [m]$ were calculated using the measured outer diameter of the ring d, measured inner diameter of the housing D, the average temperature rise over the ambient temperature $\Delta t\ [°C]$ for the ring and $\Delta T\ [°C]$ for the housing. For both the ring and housing was used identical thermal expansion coefficient $\alpha\ [K^{-1}]$ stated in the Table 5.

$$\delta = \frac{d\left(\alpha_{ring}\,\Delta t + 1\right) - D\left(\alpha_{housing}\,\Delta T + 1\right)}{2} \qquad (4\text{-}11)$$

Respecting the impossibility of negative range of air gap thickness, the values were further used as thermally inducted deformation. The resulting contact pressure $p\ [Pa]$ was calculated as follows, [26]. The calculation assumes that both the ring and the housing expands correspondingly to their average temperature and that the housing is relatively rigid in comparison to the ring and so the deformation induced by temperature difference ε_{hoop} is fully taken by the comparatively thin ring.

$$p = \frac{4\,\varepsilon_{hoop}\,t\,E}{d_{nom}\,(2-\nu)} \qquad (4\text{-}12)$$

$$\varepsilon_{hoop} = \frac{\delta}{d_{nom}\left(\alpha_{ring}\,\Delta t + 1\right)} \qquad (4\text{-}13)$$

The values of pressure are further used as x axis to plot the thermal contact resistance values - Figure 53. The pressure was chosen as it is relatively simply acquired for arbitrary applications.

The values of Yovanovich's model are determined as combination of the solid spot conductance model – 2.4.4 – Yovanovich, 1981, and air gap conductance model – 2.4.6 – Gap conductance by Yovanovich, 2005, .

The input values are presented in the Table 11 except the surface microhardness, which was estimated by eq. (3-14).

4.4 Further use of acquired data

Let us evaluate shortly the possible contribution of the collected data. It seems the planar contact under even pressure is appropriately described and the available models describe it accurately. Nevertheless, the models proved to be rather sensitive if the input parameters are not accurate – see the results of planar interface experiment in the Table 7 and of the model evaluation in the Table 10.

Additionally, the cylindrical interface experiment demonstrated that the thermal contact resistance is strong function of interface temperature as it determines the pressure. Likewise, the cylindrical experiment showed that more parameters influence the resistance than the models can incorporate – mainly the cylindricality and relative position of the ring and housing. See the Figure 53 and Figure 54 comparing the model and the measured data.

4.5 FE modelling of the interface

The possibilities of FE modelling so far consist of

- Neglecting the thermal contact resistance
- Estimating the resistance using one of the listed models (and their combination)
- Incorporating experimentally obtained values

Even though the absolute value of the resistance seems rather small, neglecting its influence leads to untrue temperature distribution and thus estimated dimensional distortion suffers by unnecessary error. Effect of neglecting the resistance shows the Figure 58 which compares temperature profiles in assembly of the ring and housing to profiles in one-piece reference specimen – which equals to assembly with neglected resistance.

Estimation of the thermal contact resistance by combination of presented models erases substantially the unnecessary error. However, it does not respect specialities of the cylindrical interface and leads to underestimation of the resistance.

A suggestion is to use the combination of Yovanovich gap and solid spot estimation of the resistance and multiply the obtained values accordingly to the Figure 54. Observe that presented values have validity limited by factors as surface roughness, physical dimensions and power rate (∼bearing friction loss), thus should be used only for similar configurations.

Extra care should be provided concerning cylindricality of the surfaces and their lubrication. For precise evaluation, an experimental measurement of corresponding setup should be performed likewise it is recommended for planar interface resistance by [7].

4.6 Estimation of uncertainties

The major sources of uncertainty of data presented in the chapter Reference measurement4.2 and 4.3 are identified in this chapter.

The measuring device

The device was designed to minimize heat dissipation to the surroundings and direct the flux from the heater to the eater cooling channel. Yet the insulation layer has splits to let the wiring out and the insulation material has non-zero thermal conductivity ($k_{PUREN\ HT} = 0.023{\sim}0.026\ W/mK$) therefore an error due to the thermal leaks is present. By Madhusudana's study (chapter 2.5.4 , [15]), such error is likely the most influential.

Material properties

The thermal conductivity of the steel $k_{16MnCr5}$ used for this study was the one estimated in the chapter 3.2 and its uncertainty was described previously in the chapter 3.5 – Material properties.

The input power uncertainty

The input power was gauged by the nominal resistivity of the heater and input voltage of the power source. During the tests in the chapter 3 was verified that the resistivity of the heater varies slightly with its temperature, but those deviations are smaller than $0.2\ \%$. Generally, the error connected to the input power measurement is comparatively marginal. Furthermore, the power input value does not entry the calculations of the thermal contact conductance, it is only used as x-axis for presentational purposes.

The error of the thermometers

The sensors were the same and were used similarly as in the chapter 3. For further details, see the chapter 3.5 – The error of the thermometers.

5 Conclusion

A short review of the information given by this thesis is provided in following lines.

5.1 Review of literature

In the chapter 2.1 of the thesis a brief insight is given into the thermal issues connected to machine tool design and the main heat sources were identified. Among other disunities in machine tool construction, the point of interest was defined as the cylindrical interface between the outer bearing ring and bearing housing.

The following chapter 2.3 provides summary of the heat conduction focused on plane and cylindrical wall and their composite analogies. The concept of thermal resistance and thermal contact resistance was introduced. Basic relations were presented.

The prevailing part of the Review of literature, chapter 2.4 , deals with the thermal contact conductance models. First, the most influential parameters determining the contact qualities were listed. Elementary relations used in the models follows. The individual models of solid spot and gap conductance were presented and divided according to their assumptions. Model of radiation heat transfer and method of combination of the named models were introduced eventually.

The subsequent chapter 2.5 presents conducted experiments dealing with the thermal contact conductance of planar surfaces under various conditions. Examples of experimental setups were described and the obtained results were compared to the named models. Study of the most influential factors concerning the setup design and measurement of thermal contact conductance was reviewed. An experiment of pure gap conductance is presented lastly.

The studies concerning the thermal resistance of bolted joints and of linear guideways are described briefly in chapter 2.6 .

The last part of the literature review, chapter 2.7 , deals with materials used in spindle assembly construction. An examples of steel suitable for construction of bearing ring and bearing housing were listed. A problematics of bearing rolling elements and bearing lubrication was touched shortly and a range of thermal conductivities of used materials was established.

5.2 Experimental measurement – simplified setup

The simplified setup was built and the design is described in chapter 3.1 . The device's correct function was verified at first by inserted specimen of well-known thermal conductivity. Possible error of measurement due to the device design was established.

Consequently, the device was used to specify the material properties of steel 16MnCr5 further used for following measurements. The experiment is presented in chapter 3.2 and the results in Table 6.

The setup was further used to quantify the thermal contact resistance of a planar interface. Foundations of contact resistance measurement were laid and processing of resistance models was clarified. Chapter 3.3 carries through the measuring process and the results are presented in Table 7 and compared to the evaluated gap conductance models in Table 8 and the solid spot conductance models in Table 9. The experimentally obtained values of thermal contact resistance did not show significant dependence on the input power rate.

Chapter 3.4 describes another method of processing of the acquired data. The FE model of the system was created, enabling iterative determination of the thermal contact resistance without need to reach the steady state. The results of the dynamic approach were compared to the values previously obtained from steady state in the Table 12.

The last chapter of the simplified approach section, chapter 3.5 , deals with possible error sources.

5.3 Experiential measurement – full scale setup

In the beginning of the section, chapter 4.1 explains the measuring device design – common for the rest of the experiments. The reference specimen and the accessory was described.

To verify correct function of the device, the temperature profiles of the one-piece specimen were measured in chapter 4.2 . The acquired data were used to establish possible deviations due to the device design and further served as reference to determine the contact resistance influence. The processing of the measured temperatures was explained.

In chapter 4.3 the two-piece assembly simulating the bearing ring and housing contact was described. Consequently, the procedure of measurement and the obtained data were presented. Table 16 displays the thermal contact resistance values for individual inserted rings across various conditions. The results were interpreted and plotted as function of heat flow, Figure 49, Figure 50, and further as function of estimated interface pressure in Figure 53. Generally, the thermal contact resistance of cylindrical contact showed strong dependency on input power rate and consequently on the pressure on the interface. Evaluated model of thermal contact conductance was plotted as well and comparison to average measured resistance was carried out, Figure 54. Investigation of other parameters as ring rotational position or presence lubricant in the interface was performed. Furthermore, the obtained data were compared to the ones from the reference measurement and the effect of non-ideal contact was displayed, Figure 58. Eventually, the data processing was explained.

Possible effect of acquired data was analysed in chapter 4.4 and the possible error sources were identified in chapter 4.6 .

Bibliography

1. **Borský, V.** *Základy stavby obráběcích strojů.* Brno : Grafia Prostějov, 1991. ISBN 80-214-0361-6.

2. *Thermomechanics.* **Jílek, Miroslav.** Praha : Česká technika - nakladatelství ČVUT, 2011.

3. **Nožička, Jiří.** *Sdílení tepla.* Praha : Vydavatelství ČVUT, 1997.

4. **Yaman Yener, Sadik Kakac.** *Heat Conduction.* 4th ed. New York : Taylor & Francis Group, LLC, 2008.

5. **A. K J. Hasselström, U. E. Nilsson.** *Thermal contact conductance in bolted joints.* Gothenburg : Chalmers University of Technology, 2012.

6. *Thermal contact conductance; Theoretical considerations.* **Mikic, B. B.** 1973, International Journal of Heat and Mass Transfer, vol.17, pp. 205-214.

7. **M. G. Cooper, B.B Mikic, M.M Yovanovich.** Thermal Contact Conductance. *International Journal of Heat and Mass Transfer.* 1969, Vol. 12, 3.

8. *Four decades of research on thermal contact, gap, and joint resistance in Microelectronics.* **Yovanovich, M. Michael.** 2, Waterloo, Canada : IEEE transactions on components and packaging technologies, 2005, Vol. 28.

9. *Review of thermal joint resistance models for nonconforming rough surfaces.* **M. Bahrami, J. R. Culham, M. M. Yovanovich, G. E. Schneider.** 1, Waterloo, Canada : Applied mechanics reviews, 2006, Vol. 59.

10. **V. Antonetti, T. White, R. Simmons.** An approximate thermal contact conductance correlation. *Journal of electronic packaging.* 1993, Vol. 115, 1.

11. **Yovanovich, M. M.** *New contact and gap conductance correlations for conforming rough surfaces.* Palo Alto : presented at 16th thermo physics conference, 1981. AIAA-81-1164.

12. **Yüncü, H.** Thermal contact conductance of nominaly flat surfaces. *Heat and Mass transfer.* 2006, Vol. 43, 1, pp. 1-5.

13. **Ho, Wing On.** *Measurement of thermal accommodation coefficients of steel surfaces.* Rolla : University of Missoury - Rolla, 1970. Master theses.

14. **Sayed M. S. Wahid, C. V. Madhusudana.** Gap conductance in contact heat transfer. *International Journal of Heat and Mass Transfer.* 2000, Vol. 43, 24.

15. **Madhusudana, C. V.** Accuracy in thermal contact conductance experiments - the effect of heat losses to the surroundings. *International Communications in Heat and Mass Transfer.* 2000, Vol. 27, 6.

16. **A. Tariq, M. Asif.** Experimental investigation of thermal contact conductance for nominally flat metallic contact. *Heat ant Mass Transfer.* 2014.

17. **Z. Zhu, L. W. Zhang, S. D. Gu.** Experimental investigation of transient heat transfer between Hastelloy C-276 / narrow air gap / silicon steel. *Experimental Thermal and Fluid Science.* 2013, Vol. 45.

18. **M. Rosochowska, K. Chodnikiewicz, R. Balendra.** A new method of measuring thermal contact conductance. *Journal of Materials Processing Tech.* 2004, Vol. 145, 2.

19. **Prashant Misra, J. Nagaraju.** Thermal gap conductance at low contact pressures. *International Journal of Heat and Mass Transfer.* 2010, Vol. 53, 23-24.

20. **Morávek, Petr.** *Experimetnal determination of thermal resistance across linear guideways.* Prague : CTU - Faculty of Mechanical Engineering, 2015.

21. **SKF.** Super - precision bearings. *www.skf.com.* [Online] May 2014 http://www.skf.com/binary/57-129877/Super-precision-bearings---13383_1-EN.pdf PUB BU/P1 13383/1 EN.

22. **John K. Mahaney, Jr.** *Advances in the Production and Use of STEEL with IMPROVED INTERNAL CLEANLINESS.* West Conshohocken : ASTM, 1999. 0-8031-2605-0.

23. **You Zhou, , Hideki Hyuga, Dai Kusano, Yu-ichi Yoshizawa, Tatsuki Ohji, Kiyoshi Hirao.** Development of high-thermal-conductivity silicon nitride ceramics. *Journal of Asian Ceramic Societies.* 3, 2015, Vol. 3.

24. *Design of polymer concrete main spindle housing for cnc lathe.* **G. Vrtanoski, V. Dukovski.** Gliwice-Wisla : COMMENT, 2005.

25. **Frank P. Incopera, David P. De Witt.** *Introduction to Heat Transfer.* 3th. New York : Wiley, 1996. ISBN 9780471304586.

26. **Roylance, David.** Pressure Vessels. *MIT Open Course Ware.* [Online] 23. August. 2001 [Cited: 3.. July. 2016] http://ocw.mit.edu/courses/materials-science-and-engineering/3-11-mechanics-of-materials-fall-1999/modules/pv.pdf

27. **T. Holkup, H. Cao, P. Kolář, Y. Altintas, J. Zelený.** Thermo-mechanical model of spindles. *CIRP Annals - Manufacturing Technology.* 2010, Vol. 59, 1.

28. **GRUPPO LUCEFIN S.P.A.** 16mncr5en technical card. *Special and carbon steels.* [Online] [Cited: 23.. June. 2016] http://www.lucefin.com/wp-content/files_mf/16mncr5en.pdf

29. MachLine® - High Precision. *NTN-SRN.* [Online] January 2006 [Cited: 3. June. 2016] http://www.ntn-snr.com/industry/fr/en-en/file.cfm/machline_catalogue_gb.pdf?contentID=2621

Lists of contents

List of figures

List of tables

List of used software

Microsoft Office Word 2016

Microsoft Office Excel 2016

MATLAB 2014a

Autodesk Inventor Professional 2013

LabVIEW 201

Contents of enclosed CD

The thesis in .pdf format

The technical drawing in .pdf format

The measured data in .mat files

The script used for dynamic approach (chapter 3.4) in .m format

The thesis assignment

Appendix

A. The dynamic approach

The dimensional data used for evaluation of the dynamic model, subscript hs stands for heat sink.

L	0.008	m
L_{hs}	0.03	m
A	7.980E-04	m^2
cp	460	J/kgK
cp_{hs}	900	J/kgK
k	42	W/m^2K
k_{hs}	205	W/m^2K
ρ	7850	kg/m^3
ρ_{hs}	2700	kg/m^3

The compiled matrixes used for FEM dynamic analysis are listed below.

$$\boldsymbol{K}_1 =$$

4,00	-4,00			
-4,00	6,00	-2,00		
	-2,00	6,00	-4,00	
		-4,00	4,00	

$$\boldsymbol{K}_2 =$$

4,00	-4,00			
-4,00	6,00	-2,00		
	-2,00	6,00	-4,00	
		-4,00	64,18	-60,19
			-60,19	60,19

$$\boldsymbol{C}_1 =$$

11,00				
	33,01			
		22,01		
			0,00	

$$\boldsymbol{C}_2 =$$

$$\begin{vmatrix} 11{,}00 & & & & & \\ & 33{,}01 & & & & \\ & & 33{,}01 & & & \\ & & & 13{,}78 & & \\ & & & & & 2{,}78 \end{vmatrix}$$

The Matlab script used for iterative determination of the thermal contact resistance and to reconstruct the time temperature development.

```
kc =1:0.1:3;                              % [W/K] initial guess

for ii=1:length(kc)
    K3= kc(ii)*[1,-1;
        -1,1];

    n1=size(K1,1);
    n2=size(K2,1);

    B=zeros(3,n1+n2+2);
    B(1,n1)=1;B(1,n1+1)=-1;
    B(2,n1+2)=1;B(2,n1+3)=-1;
    B(3,n1+n2+2)=1;
    L=null(B,'r');

    Ka=blkdiag(K1,K3,K2);                 % overall transm. matrix
    Ca=blkdiag(C1,zeros(2),C2);           % overall th. inertia
matrix

    Kp=L'*Ka*L;
    Cp=L'*Ca*L;

    Q=zeros(size(Kp,1),1);Q(1)=1;
    O=zeros(size(Kp,1),4);
    O(2,1)=1;O(3,2)=1;O(6,3)=1;O(7,4)=1;
    h=0;
    u=zeros(size(Kp,1),1);u(4)=1;u(5)=-1;
    v=u;
    fr=HvsFRQ.frq;                        % frequency

    h=HvsFRQ.h10(:,1:4)';                 % transfer function

    tic;
    b=therm_fit2(h,Kp,Cp,u,v,O,Q,fr); % the correction for each
frequency
    toc;
    bm(:,ii)=mean(abs(b),2);              % the average correction
for each guess
    bstd(:,ii)=std(abs(b),[],2);
```

```
end
%%
kc=2.3; %

K3= kc*[1,-1;
    -1,1];

n1=size(K1,1);
n2=size(K2,1);

B=zeros(3,n1+n2+2);
B(1,n1)=1;B(1,n1+1)=-1;
B(2,n1+2)=1;B(2,n1+3)=-1;
B(3,n1+n2+2)=1;
L=null(B,'r');

Ka=blkdiag(K1,K3,K2);
Ca=blkdiag(C1,zeros(2),C2);

Kp=L'*Ka*L;
Cp=L'*Ca*L;

Q=zeros(size(Kp,1),1);Q(1)=1;
O=zeros(size(Kp,1),4);
O(2,1)=1;O(3,2)=1;O(6,3)=1;O(7,4)=1;

u=zeros(size(Kp,1),1);u(4)=1;u(5)=-1;
v=u;
fr=HvsFRQ.frq;
h=[];                              % rational substitutions of h
h(1,:)=HvsFRQ.hsub10_1';
h(2,:)=HvsFRQ.hsub10_2';
h(3,:)=HvsFRQ.hsub10_3';
h(4,:)=HvsFRQ.hsub10_4';
tic;
b=therm_fit2(h,Kp,Cp,u,v,O,Q,fr);
toc;
bm=mean(abs(b),2)
bstd=std(abs(b),[],2)

%%

Tin(1:size(Kp,1))=0;               % initial condition
Tin=Tin';
tend=4592;                         % length of simulation
th=2566;                           % length of heating ON
qi=10.4;                           % heat flow [W]
Qi=zeros(size(Kp,1),1);
Qi(1)=qi;
A = -inv(Cp)*Kp;                   % = inv(E)*A
B = inv(Cp)*Qi;

ic=[];ic(1:size(A,1))=0;
y0=ic';
```

```
atol=1e-5;                          % Create an array of all ones

% Create or alter options structure for input to ordinary
differential equation (ODE) solvers y'= f(t,y
% setting Error Tolerance Properties
options = odeset('RelTol',1e-3,'AbsTol',atol,'Jacobian',A);)

% **** integrates the system of differential equations  from
time t0 to tf with initial conditions y0 ****
%Function f = odefun(t,y) = right part of the equation

f= @(t,y) tSYS(t,y,A,B,th);

[t1,Y1] = ode45(f,0:2:tend,y0,options);

set(0,'defaultLineLineWidth', 1.5)
plot(t1,Y1(:,2),'--',t1,Y1(:,3),'--',t1,Y1(:,6),'--
',t1,Y1(:,7),'--')
hold on
plot(separated.Ttime10Wlin(:,1),separated.Ttime10Wlin(:,2:5))
hold on, grid on, zoom on
xlabel('time [s]');ylabel('tenperature rise [°C]')
title('comparison of model behaviour to time development of
measured temperatures')
legend('node 2','node 3','node 6','node 7','T1','T2','T3','T4')
```

The function used in the script: therm_fit2

```
function b=therm_fit2(h,Ki,Ci,u,v,O,Q,fr)

syms w real

A=1i*w*Ci+Ki;
Ai(w)=inv(A);

vAiu(w)=v'*Ai*u;
oAiq(w)=O'*Ai*Q;
x1(w)=O'*(Ai*vAiu-(Ai*u)*(v'*Ai))*Q;
vAiuF=matlabFunction(vAiu);
oAiqF=matlabFunction(oAiq);
x1F=matlabFunction(x1);

VAIU=vAiuF(2*pi*fr');
OAIQ=oAiqF(2*pi*fr');
X1=x1F(2*pi*fr');

y=h-OAIQ;
x=X1-h.*repmat(VAIU,size(O,2),1);

b=x.\y;
```

```
end
```

The function used in the script: tSYS

```
function [ dy ] = tSYS( t,y, A, B,th )
dy = zeros(size(y,1),1);
if t<=th
    u = 1; % creates zero column
else
    u=0;
end

dy = A*y+B*u;

end
```

B. Temperature profiles - reference specimen

The temperature profiles obtained by steady state measuring of the reference one-piece specimen are presented below.

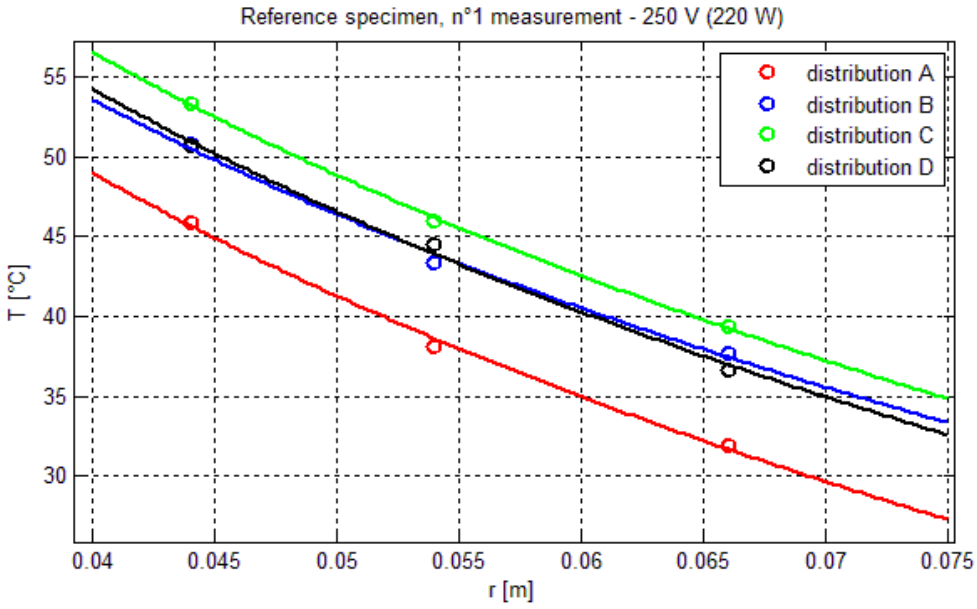

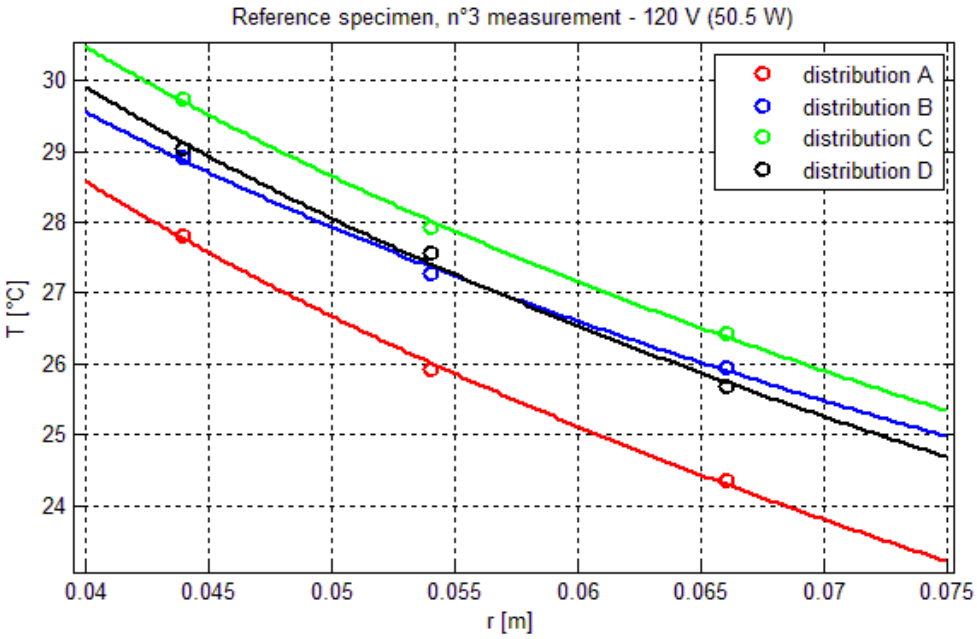

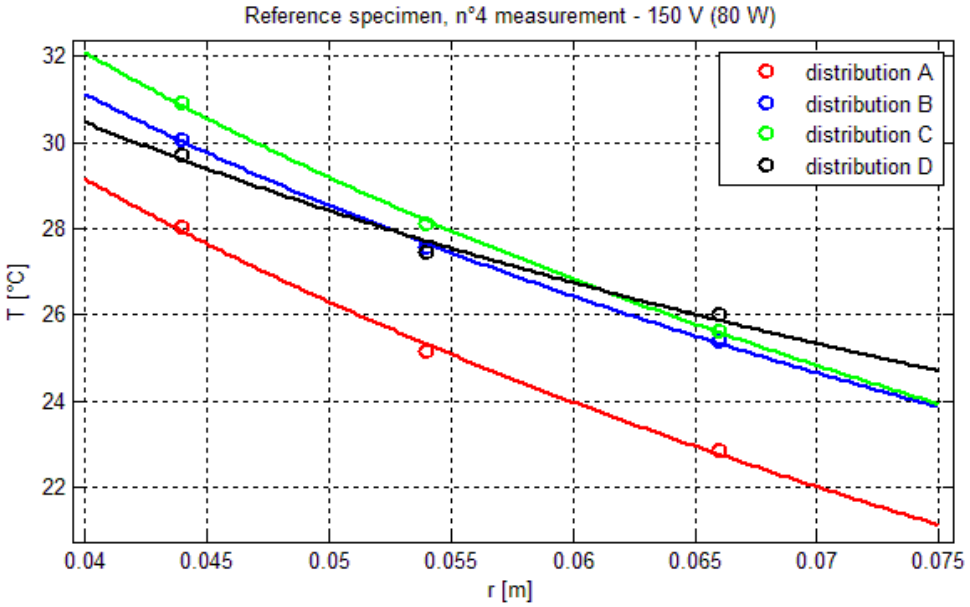
Reference specimen, n°4 measurement - 150 V (80 W)
distribution A
distribution B
distribution C
distribution D
T [°C]
r [m]
32
30
28
26
24
22
0.04
0.045
0.05
0.055
0.06
0.065
0.07
0.075

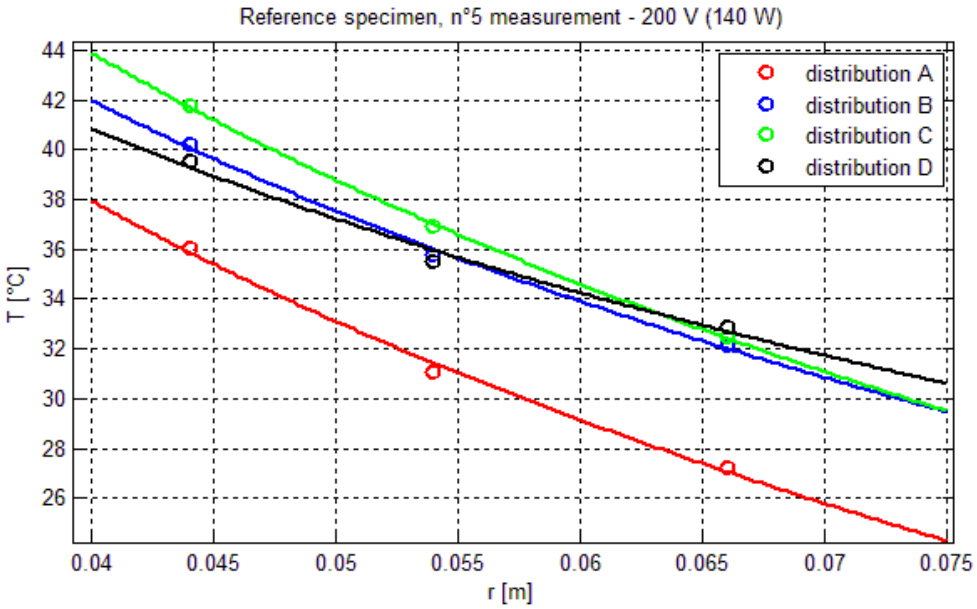
Reference specimen, n°5 measurement - 200 V (140 W)
distribution A
distribution B
distribution C
distribution D
T [°C]
r [m]
44
42
40
38
36
34
32
30
28
26
0.04
0.045
0.05
0.055
0.06
0.065
0.07
0.075

C. Temperature profiles – bearing ring number 1

The temperature profiles obtained by steady state measuring of the bearing ring number 1 are presented below.

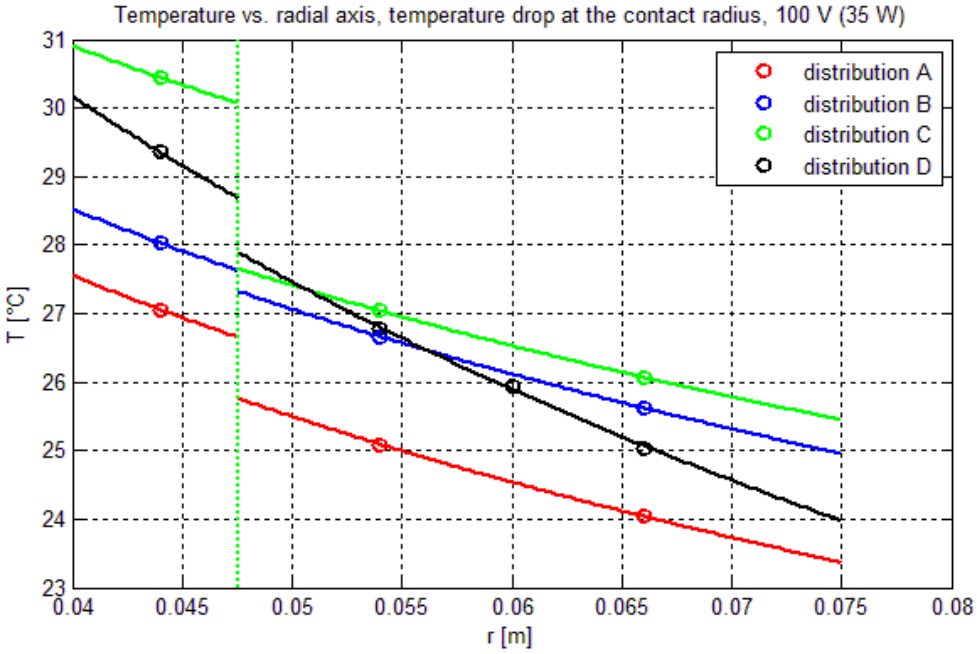

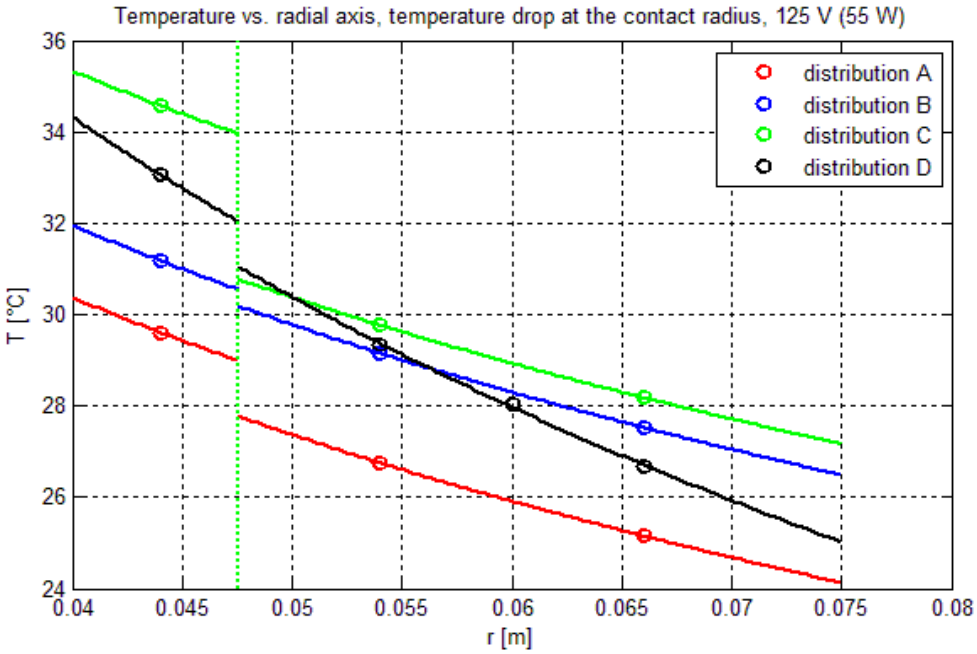

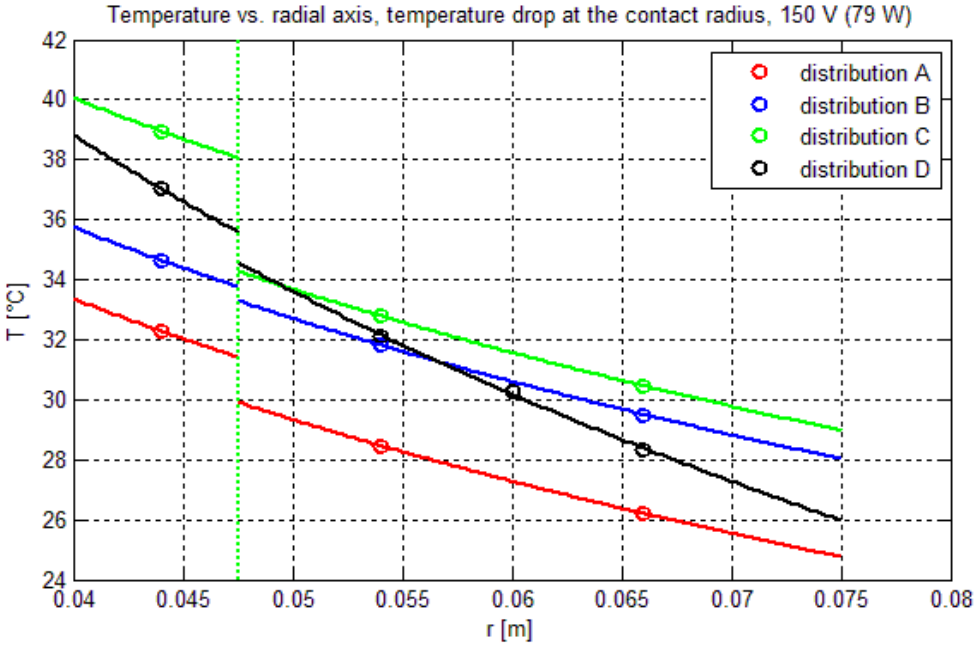
Temperature vs. radial axis, temperature drop at the contact radius, 150 V (79 W)
distribution A
distribution B
distribution C
distribution D
T [°C]
r [m]
42
40
38
36
34
32
30
28
26
24
0.04
0.045
0.05
0.055
0.06
0.065
0.07
0.075
0.08

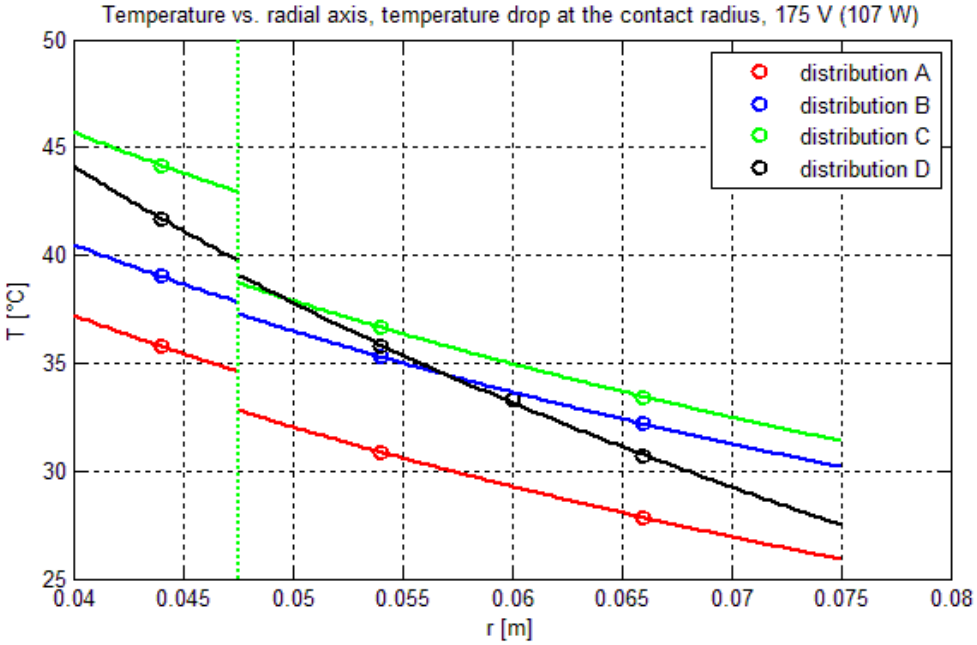
Temperature vs. radial axis, temperature drop at the contact radius, 175 V (107 W)
distribution A
distribution B
distribution C
distribution D
T [°C]
r [m]
50
45
40
35
30
25
0.04
0.045
0.05
0.055
0.06
0.065
0.07
0.075
0.08

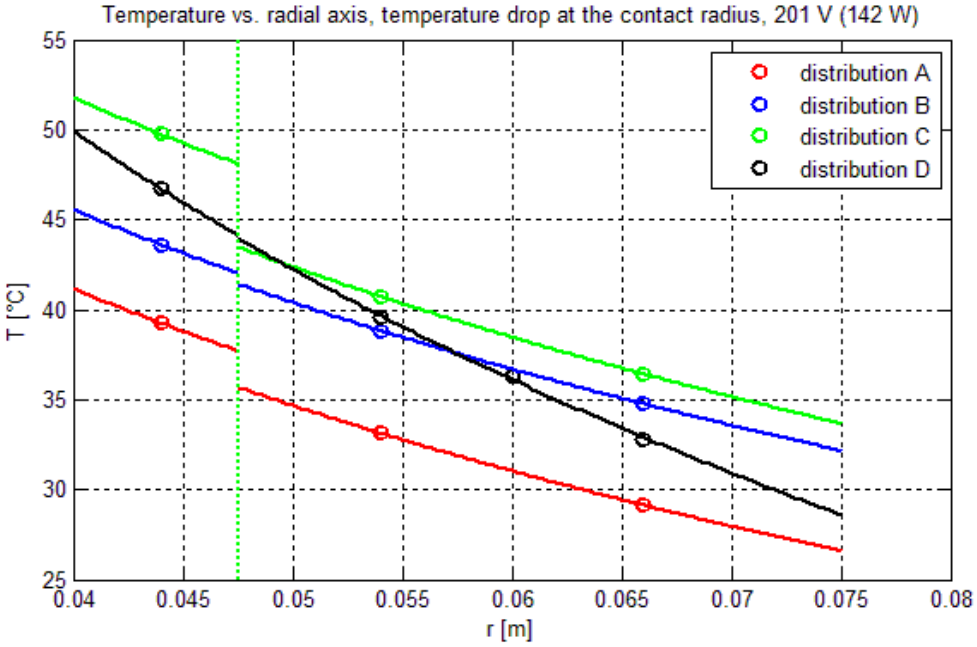
Temperature vs. radial axis, temperature drop at the contact radius, 201 V (142 W)
distribution A
distribution B
distribution C
distribution D
T [°C]
r [m]
55
50
45
40
35
30
25
0.04
0.045
0.05
0.055
0.06
0.065
0.07
0.075
0.08

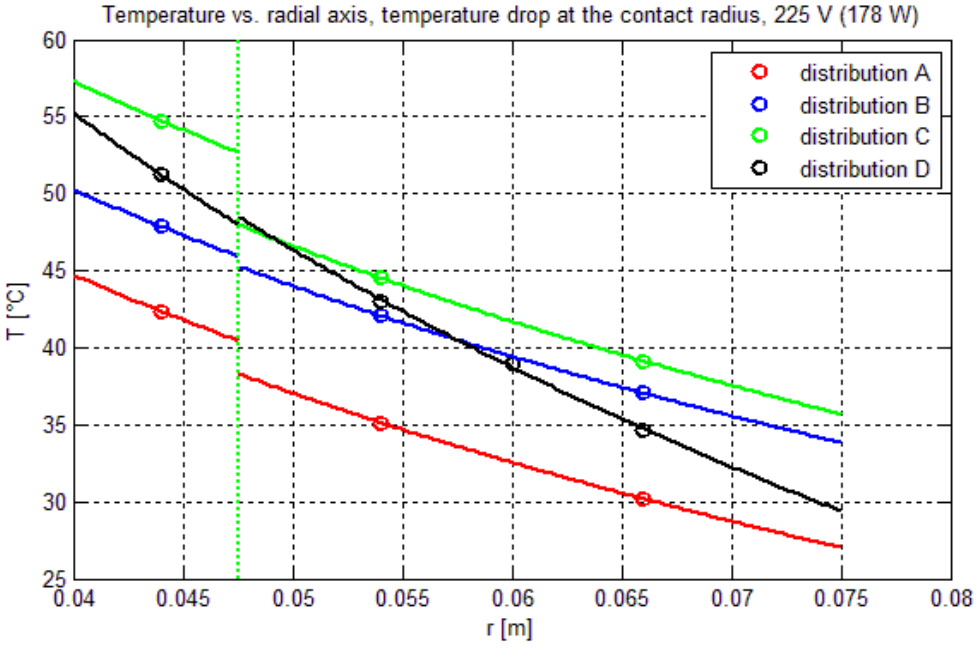
Temperature vs. radial axis, temperature drop at the contact radius, 225 V (178 W)
distribution A
distribution B
distribution C
distribution D
T [°C]
r [m]
60
55
50
45
40
35
30
25
0.04
0.045
0.05
0.055
0.06
0.065
0.07
0.075
0.08

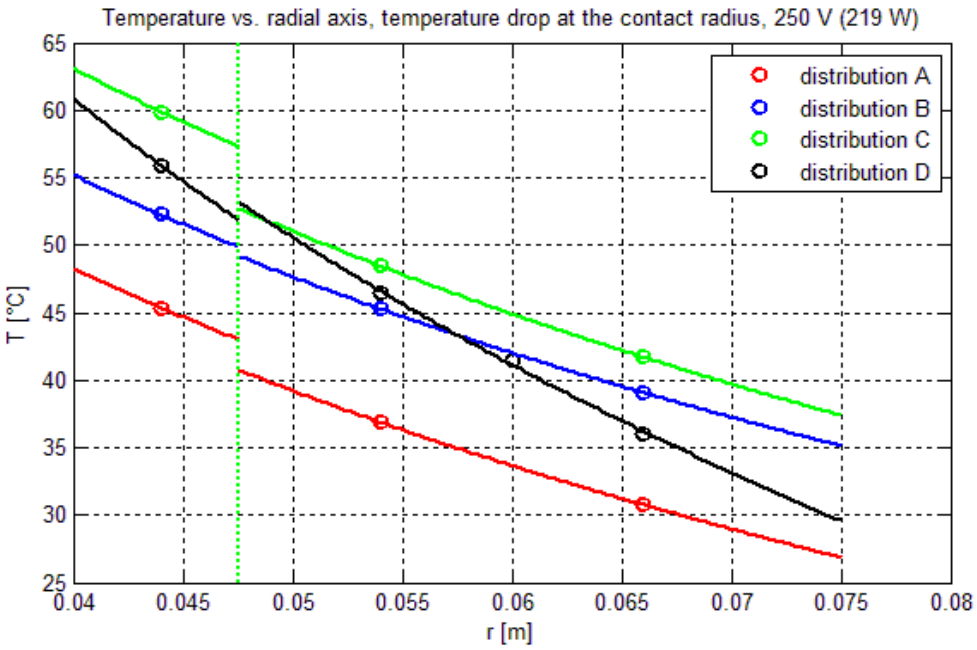

D. Temperature profiles – bearing ring number 2

The temperature profiles obtained by steady state measuring of the bearing ring number 2 are presented below.

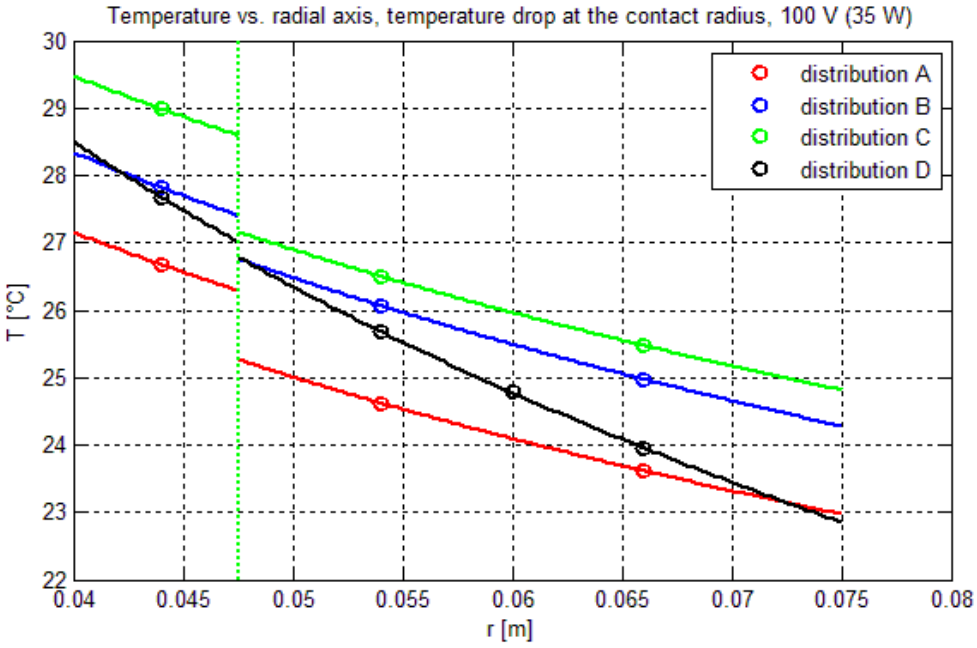

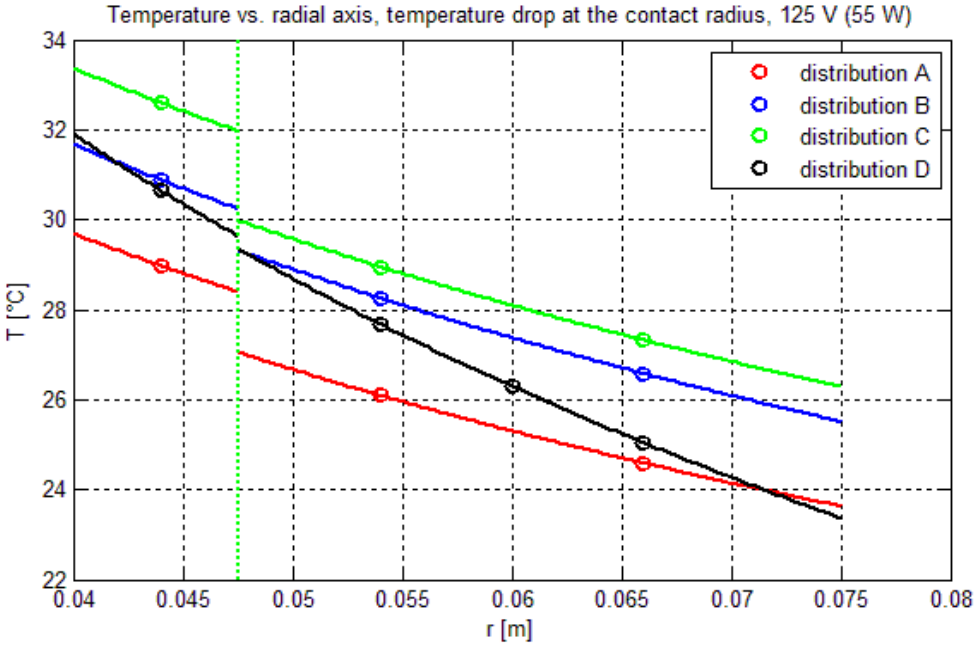
Temperature vs. radial axis, temperature drop at the contact radius, 125 V (55 W)
distribution A
distribution B
distribution C
distribution D
T [°C]
r [m]
34
32
30
28
26
24
22
0.04
0.045
0.05
0.055
0.06
0.065
0.07
0.075
0.08

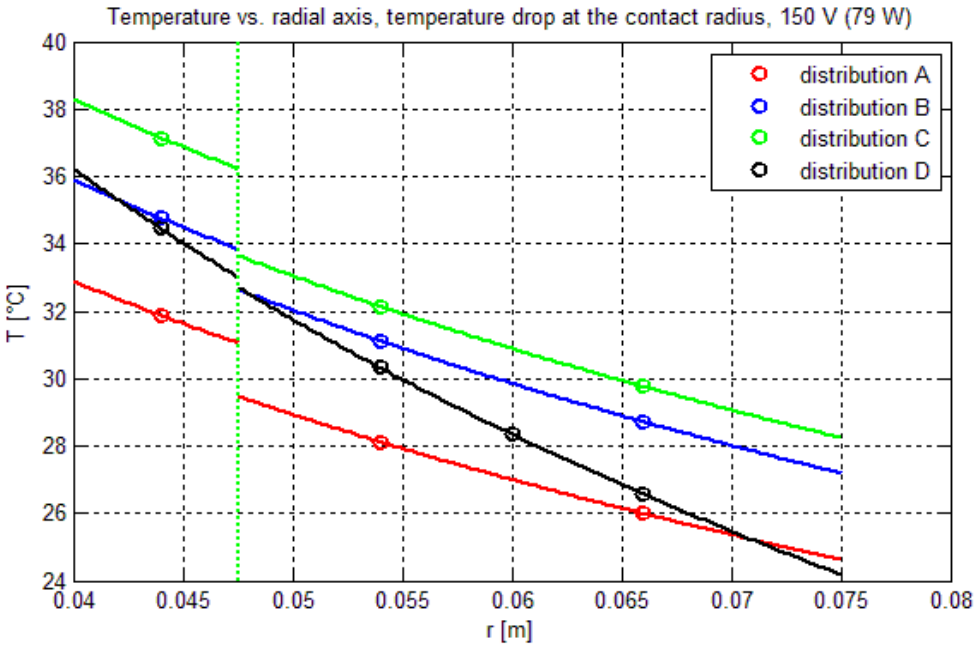
Temperature vs. radial axis, temperature drop at the contact radius, 150 V (79 W)
distribution A
distribution B
distribution C
distribution D
T [°C]
r [m]
40
38
36
34
32
30
28
26
24
0.04
0.045
0.05
0.055
0.06
0.065
0.07
0.075
0.08

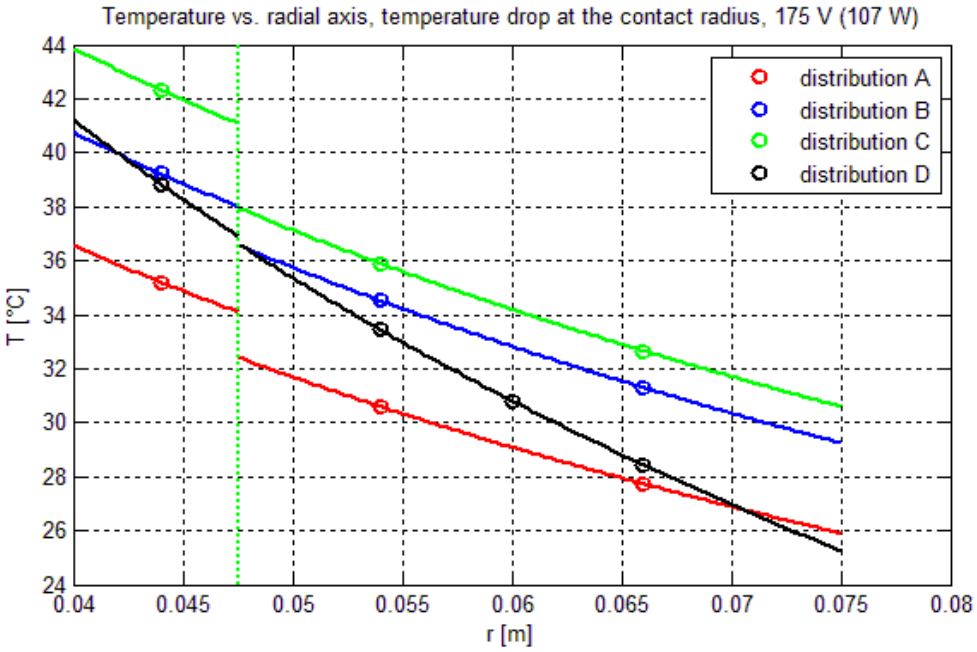
Temperature vs. radial axis, temperature drop at the contact radius, 175 V (107 W)
distribution A
distribution B
distribution C
distribution D
T [°C]
r [m]
44
42
40
38
36
34
32
30
28
26
24
0.04
0.045
0.05
0.055
0.06
0.065
0.07
0.075
0.08

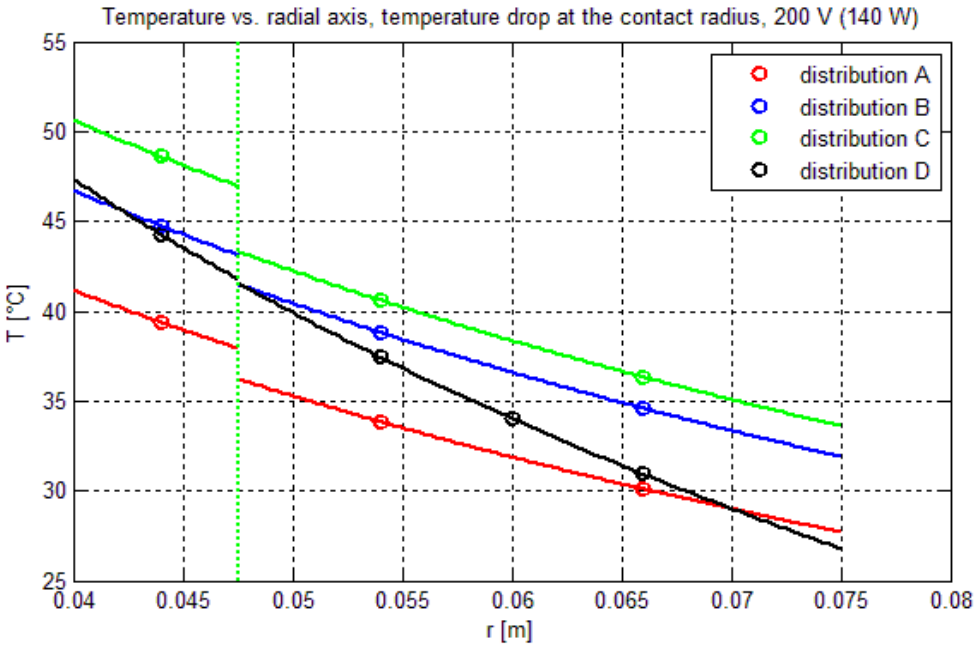
Temperature vs. radial axis, temperature drop at the contact radius, 200 V (140 W)
distribution A
distribution B
distribution C
distribution D
T [°C]
r [m]
55
50
45
40
35
30
25
0.04
0.045
0.05
0.055
0.06
0.065
0.07
0.075
0.08

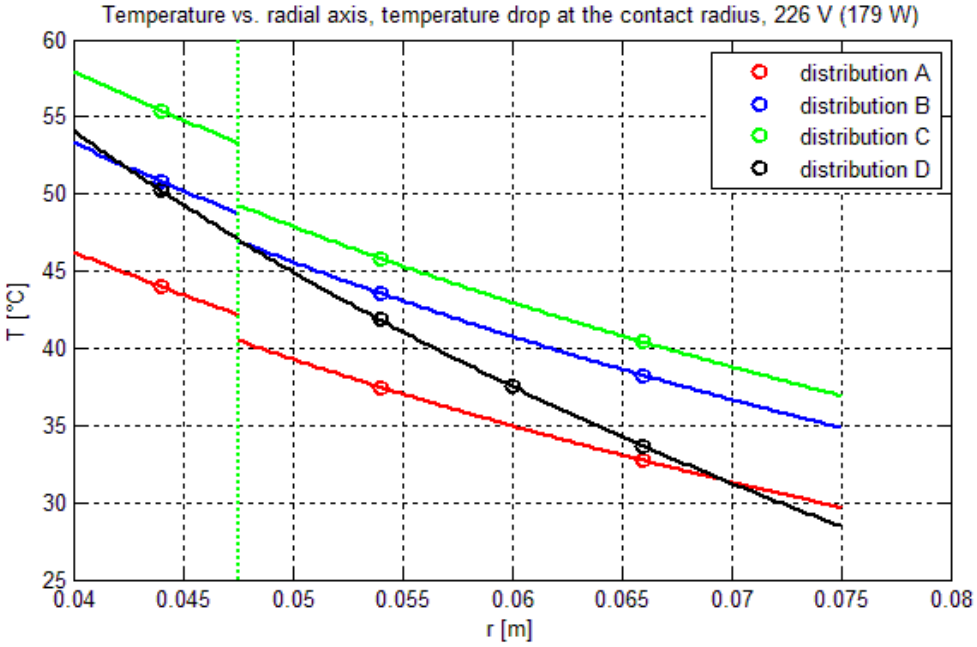
Temperature vs. radial axis, temperature drop at the contact radius, 226 V (179 W)
distribution A
distribution B
distribution C
distribution D
T [°C]
r [m]
60
55
50
45
40
35
30
25
0.04
0.045
0.05
0.055
0.06
0.065
0.07
0.075
0.08

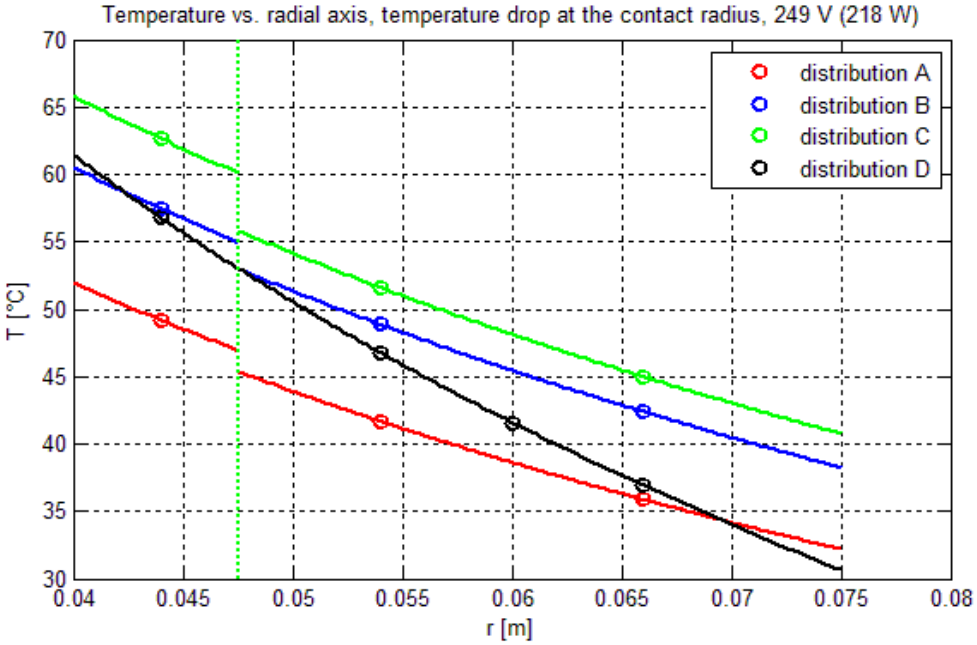
Temperature vs. radial axis, temperature drop at the contact radius, 249 V (218 W)
distribution A
distribution B
distribution C
distribution D
T [°C]
r [m]
70
65
60
55
50
45
40
35
30
0.04
0.045
0.05
0.055
0.06
0.065
0.07
0.075
0.08

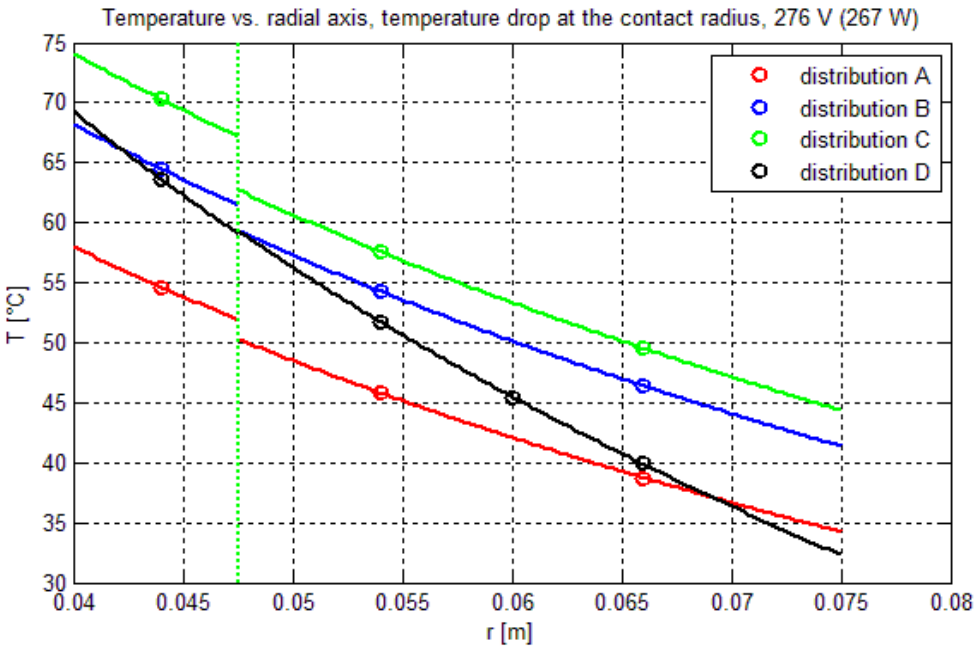

E. Temperature profiles – bearing ring number 3

The temperature profiles obtained by steady state measuring of the bearing ring number 3 are presented below.

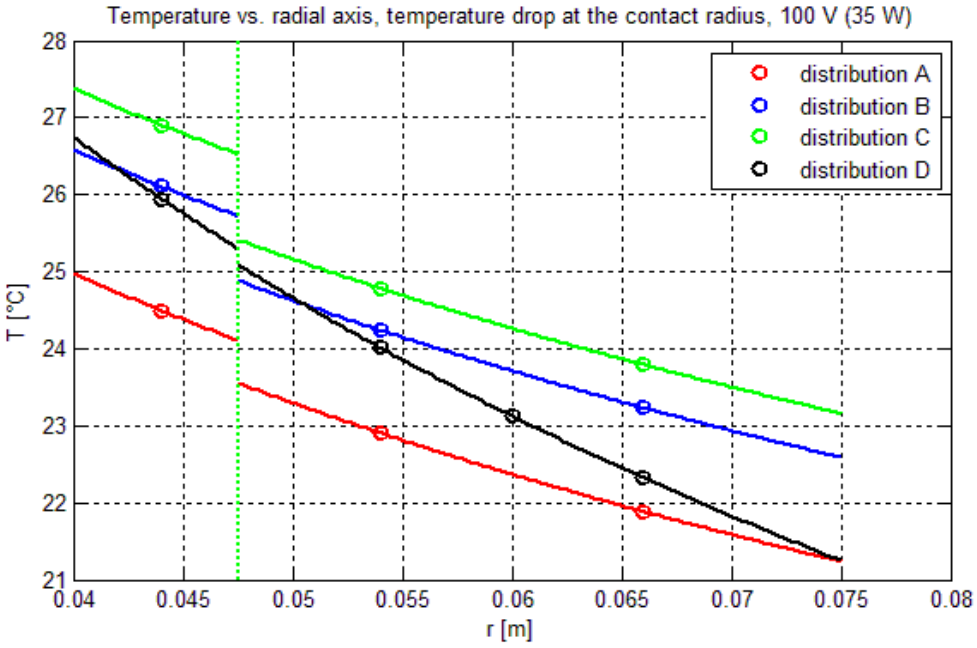

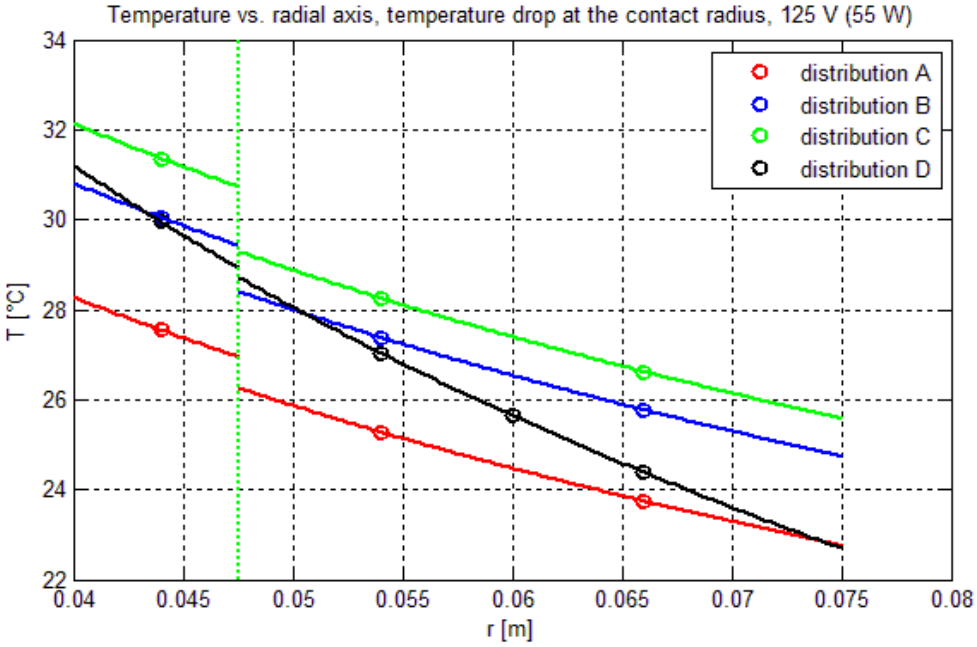
Temperature vs. radial axis, temperature drop at the contact radius, 125 V (55 W)
distribution A
distribution B
distribution C
distribution D
T [°C]
r [m]
34
32
30
28
26
24
22
0.04
0.045
0.05
0.055
0.06
0.065
0.07
0.075
0.08

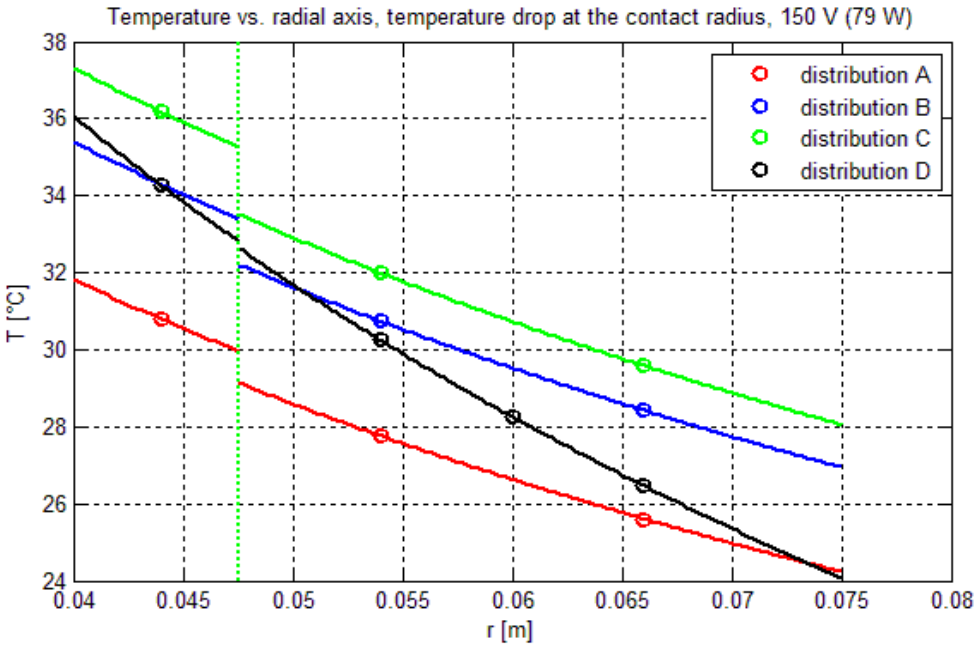
Temperature vs. radial axis, temperature drop at the contact radius, 150 V (79 W)
distribution A
distribution B
distribution C
distribution D
T [°C]
r [m]
38
36
34
32
30
28
26
24
0.04
0.045
0.05
0.055
0.06
0.065
0.07
0.075
0.08

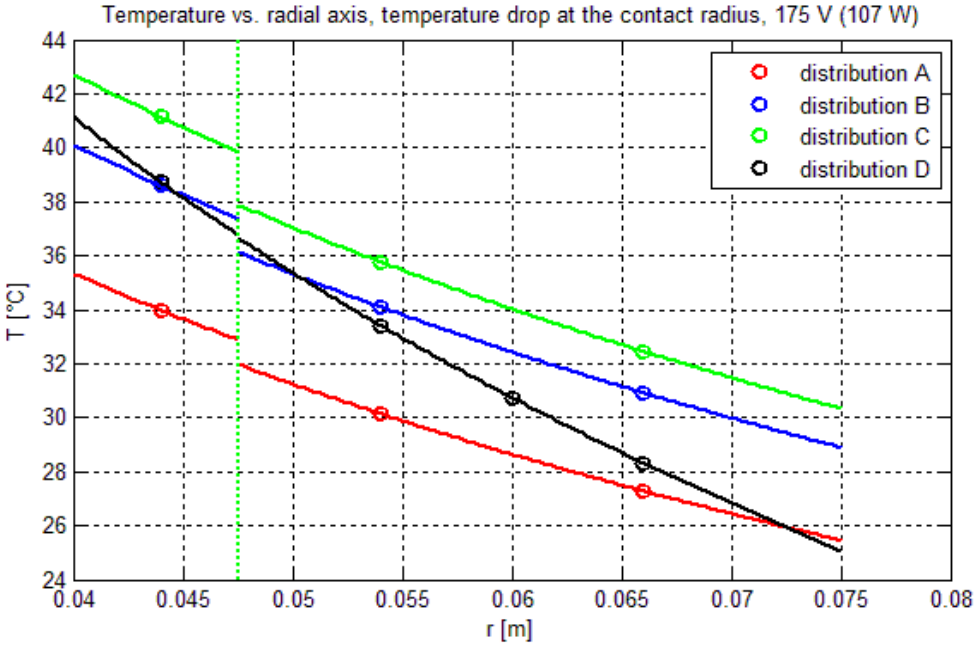
Temperature vs. radial axis, temperature drop at the contact radius, 175 V (107 W)
distribution A
distribution B
distribution C
distribution D
T [°C]
r [m]
44
42
40
38
36
34
32
30
28
26
24
0.04
0.045
0.05
0.055
0.06
0.065
0.07
0.075
0.08

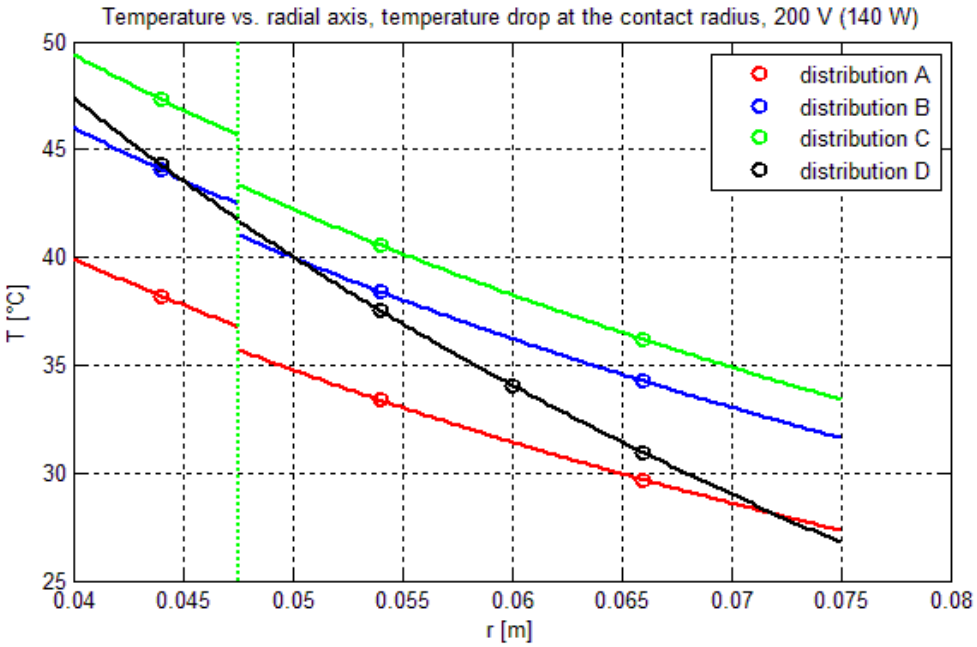
Temperature vs. radial axis, temperature drop at the contact radius, 200 V (140 W)
distribution A
distribution B
distribution C
distribution D
T [°C]
r [m]
50
45
40
35
30
25
0.04
0.045
0.05
0.055
0.06
0.065
0.07
0.075
0.08

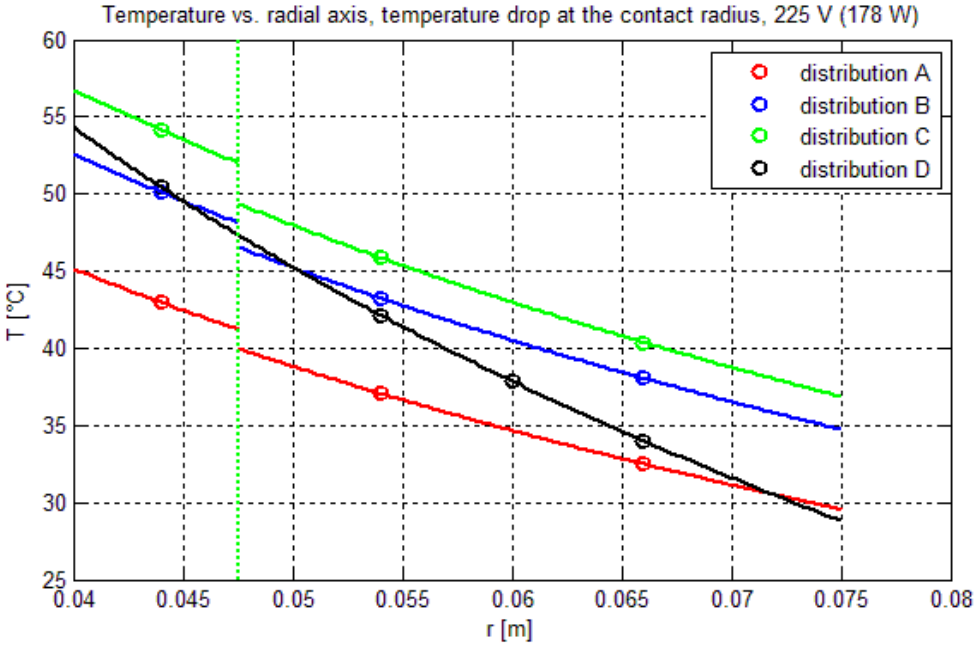
Temperature vs. radial axis, temperature drop at the contact radius, 225 V (178 W)
distribution A
distribution B
distribution C
distribution D
T [°C]
r [m]
60
55
50
45
40
35
30
25
0.04
0.045
0.05
0.055
0.06
0.065
0.07
0.075
0.08

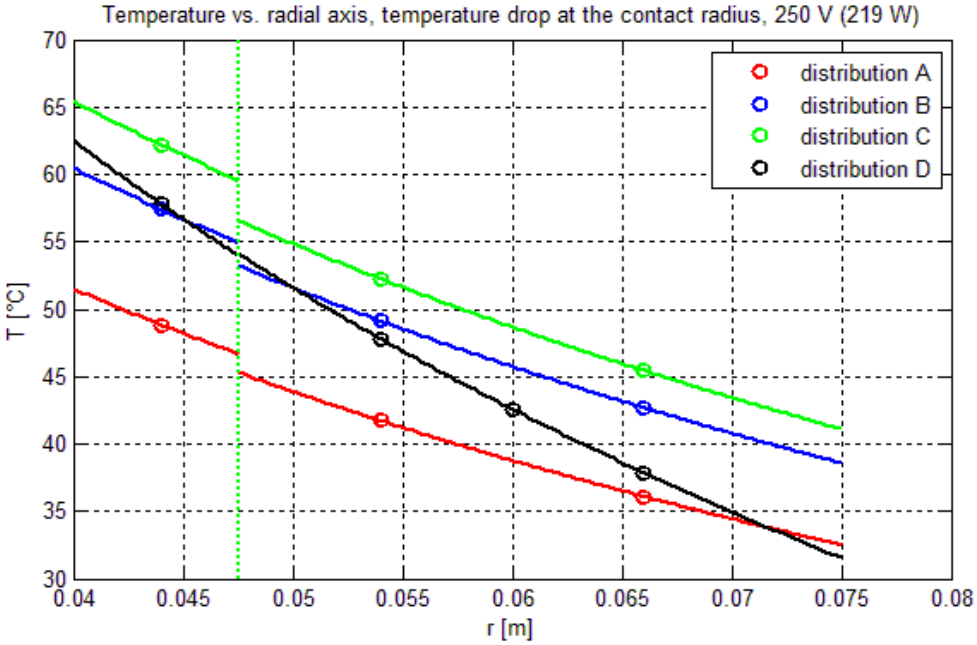
Temperature vs. radial axis, temperature drop at the contact radius, 250 V (219 W)
distribution A
distribution B
distribution C
distribution D
T [°C]
r [m]
70
65
60
55
50
45
40
35
30
0.04
0.045
0.05
0.055
0.06
0.065
0.07
0.075
0.08

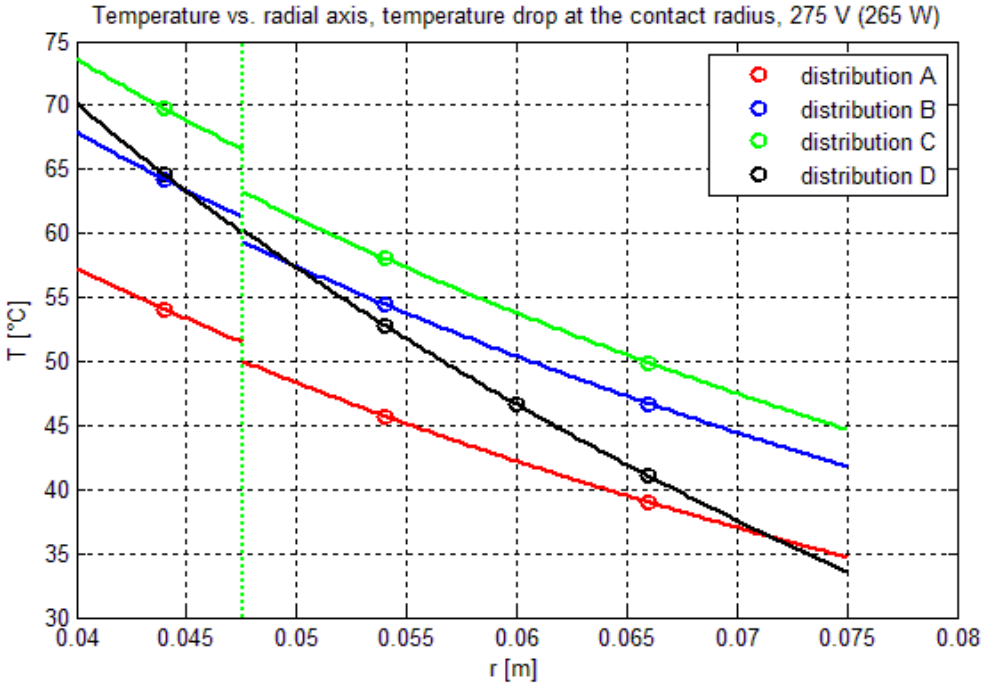
Temperature vs. radial axis, temperature drop at the contact radius, 275 V (265 W)
distribution A
distribution B
distribution C
distribution D
T [°C]
r [m]
75
70
65
60
55
50
45
40
35
30
0.04
0.045
0.05
0.055
0.06
0.065
0.07
0.075
0.08

F. The technical insulation: Puren E 40 HT

The technical list of the insulation material used for construction of the device for cylindrical contact investigation.

puren® PIR Hochtemperatur-Hartschaum E 40 HT Technische Daten*

Duroplastischer Hochleistungsdämmstoff mit spezieller Eignung im Hochtemperaturbereich

Rohdichte	EN 1602	kg/m³	37 - 42
Druckfestigkeit //	EN 826	kPa	282
Druckfestigkeit $\perp_1$	EN 826	kPa	124
Druckfestigkeit $\perp_2$	EN 826	kPa	199
Druckfestigkeit $\perp$	EN 826	kPa	162
Biegefestigkeit	EN 12089	kPa	250 - 300
Querzugfestigkeit	EN 1607	kPa	220 260
E-Modul		MPa	10,0 – 13,0
Schubfestigkeit	EN 12090 (DIN 53294)	kPa	150 – 190
Scherfestigkeit	EN 12090 (DIN 53427)	kPa	120 - 150
Geschlossenzelligkeit	ISO 4590	%	90 – 95
Wasseraufnahme	EN 12087	max %	3
Einsatz-Temperatur	-	°C	- 80 / + 200
Brandverhalten	EN 13501-1 DIN 4102	-	E B 2
Wärmeleitzahl **	EN 12667	W/(mK)	0,023-0,026

* Daten wurden als Durchschnittswerte unter Produktionsbedingungen ermittelt. Für die mechanischen Werte wird sichergestellt, dass die Mindestangaben nicht mehr als 10% unterschritten werden.
** Laborwert